ULTRASONIC ATTENUATION IN BISMUTH SILICON OXIDE AND BISMUTH GERMANIUM OXIDE

by

Parmjit Kaur Sandhu M.Sc.,

Physics Department,

Bedford College,

University of London.

A thesis submitted for
the degree of Doctor of Philosophy
at the University of London

September, 1980

ABSTRACT

The propagation of ultrasonic waves has been studied in single crystals of undoped and doped bismuth germanium oxide ($Bi_{12}GeO_{20}$) and undoped bismuth silicon oxide ($Bi_{12}SiO_{20}$). These crystals are piezoelectric (Cubic Space Group I23) and direct excitation of ultrasound was used wherever possible. Attenuation measurements were made from 10 to 190 MHz over the temperature range 4.2 to 260 K.

A large attenuation peak was observed in the undoped crystals between 35 and 50 K for only those ultrasonic modes whose velocity depends on the elastic modulus C_{44}. This peak is shown to be a single anelastic relaxation peak and is interpreted as due to point defects. Using the selection rules for anelastic relaxation in cubic crystals, it is deduced that these defects must have trigonal symmetry.

The magnitude of the attenuation peak in doped BGO samples is strongly dependent on the presence of dopants. Doping with Al, Ga, Pb, P+Ga, Ga+Cr, all removed the attenuation peak, while Cr increased it and Zn reduced it. A strong correlation was observed between the attenuation peak, the colour of the crystals and the optical absorption just below the band gap measured in these samples by other workers. These results indicate that the same defect centre is responsible for both the optical and the ultrasonic absorption. Possible defects are discussed taking the optical absorption, X-ray diffraction, EPR and other available measurements into consideration.

The ultrasonic attenuation was measured before and after annealing at 450°C in vacuo or in pure oxygen. No change was observed for an undoped sample. However, for the Cr doped sample the attenuation was reduced by vacuum annealing and restored by oxygen annealing. This seems to be closely related to previous observations of photochromic behaviour in BSO doped with Cr. Measurements were also made to study the effects of gamma irradiation on the attenuation in undoped BSO.

CONTENTS

		Page
Acknowledgements		vii
List of figures		viii
List of tables		xiv
CHAPTER 1	BISMUTH GERMANIUM OXIDE AND BISMUTH SILICON OXIDE	1
1.1	History	2
1.2	Structure	7
1.3	Stochiometry	14
1.4	Piezoelectricity	16
1.5	Elastic properties	19
1.6	Optical properties	23
1.7	Photochromism	25
1.8	Semiconducting properties	26
1.9	Technical applications	27
CHAPTER 2	EXPERIMENTAL TECHNIQUES	28
2.1	Electronics	29
2.2	Transducers, delay rods and samples	37
2.3	Sample preparation	39
2.4	Measurements in the temperature range 4.2 to 250 K	45
2.5	Thermometry	51
2.6	Experimental procedure	55

		Page
CHAPTER 3	RELAXATION ATTENUATION AND MEASUREMENTS IN UNDOPED BGO AND BSO	60
3.1	Relaxation	61
3.2	Relaxation strength	69
3.3	Relaxation processes	79
3.4	Experimental results	84
3.5	Analysis of experimental results	93
CHAPTER 4	ATTENUATION MEASUREMENTS IN DOPED, ANNEALED BGO AND γ-IRRADIATED BSO	116
4.1	Doped BGO samples	117
4.2	Ultrasonic attenuation results and analysis	119
4.3	Correlation with optical absorption	138
4.4	Effects of annealing and γ-irradiation on point defects in BGO, BSO	143
4.5	Experimental results in annealed BGO	146
4.6	Experimental results in γ-irradiated BSO	153
CHAPTER 5	PHONON-PHONON ATTENUATION	159
5.1	Introduction	160
5.2	Low temperature region, $\omega\tau > 1$	161
5.3	High temperature region $\omega\tau < 1$	164
5.4	Experimental results	167
CHAPTER 6	DISCUSSION AND CONCLUSION	
6.1	Introduction	173
6.2	Experimental evidence	176

		Page
6.3	Other available measurements.	187
6.4	Possible defect centre	189
6.5	Conclusion	195

APPENDIX 1

Computer program for data analysis 203

APPENDIX 2 Ultrasonic attenuation in doped bismuth germanium oxide 206

(Reprint: Proceedings of the Institute of Acoustics 1980)

paper given by author at the Acoustic 1980 conference.

ACKNOWLEDGEMENTS

It is a pleasure to thank my supervisor, Dr M. J. Lea, for his constant advice, encouragement and availability for discussion. I am also grateful to Professor E. R. Dobbs for his help and guidance from time to time during my stay in this College.

I am indebeted to Dr. Grabmaier and R. Oberschmid of Siemens Research Laboratories (Germany) for supplying us with single crystals of doped BGO.

I would like to thank Mr. A. K. Betts for his help with electronics throughout the work; Mr S. Sen for his assistance in orientation and polishing of the crystals; Mr A.O.T. Le Motte, Mr. F. Greenough, Mr. W. Baldock and other technical staff of the Department for their assistance.

Mr. F.A. Grimes and Mr A.W. King are also gratefully acknowledged for their help in designing the sonic cells. I would like to thank Miss A. LeaKer for her timely help in typing this thesis.

Finally, I would like to thank the British Council for granting me a Fee Award.

P. K. SANDHU

FIGURES

		Page
1.1	Schematic diagram for growing BGO/BSO crystals	5
1.2	Heptacoordinated bismuth in BGO	9
1.3	Arrangement of bismuth atoms and GeO_4 tetrahedra in a unit cell of BGO	11
1.4	Connection of two GeO_4 tetrahedra by means of two Bi-polyhedra	12
1.5	A unit cell of BGO showing the tetrahedra around each Ge atom	18
1.6	Optical absorption for undoped BSO	24
2.1	Block diagram of Matec 9000	30
2.2	Block diagram of complete experimental set up	32
2.3	Calibration curve for Matec detector	34
2.4	Boxcar echo monitoring	35
2.5	Calibration curve for Matec detector using a Marconi pulse generator	36
2.6	A typical pulse-echo train	44
2.7	Block diagram of experimental probe	46
2.8	Sonic cell	48

		Page
2.9	Sonic cell	52
2.10	Calibration curve for the carbon-glass resistor	54
2.11	A raw data plot from X-Y recorder	57
2.12	Attenuation as a function of temperature	58
3.1	Strain ellipsoid	66
3.2	Attenuation of transverse (110,001) mode in BGO as a function of temperature and frequency	85
3.3	Temperature and frequency dependence of T(100,001) and longitudinal (100,100) mode in BGO	87
3.4	Attenuation of longitudinal (111,111) mode	88
3.5	Attenuation as a function of temperature for all modes	89
3.6	Attenuation of transverse (110,001) mode in BSO	90
3.7	Logarithm of the frequency versus reciprocal of peak temperatures for BSO and BGO	95
3.8	Normalized attenuation for the transverse (100,001) mode versus 1/T	97

		Page
3.9	Logarithm of the relaxation time versus reciprocal temperature for the transverse (110,001) mode in BGO	101
3.10	Logarithm of the relaxation time versus reciprocal temperature for the transverse (100,001) mode in BGO	102
3.11	Logarithm of the relaxation time versus reciprocal temperature for the transverse wave (110,001) in BSO	103
3.12	Attenuation of T(100,001) mode, fitted to equation 3.5.4	105
4.1	Ultrasonic attenuation for the transverse (110,001) mode in (BGO + Cr), as a function of temperature and frequency	120
4.2	Ultrasonic attenuation versus temperature for the transverse wave (110,001) in (BGO + Zn) at various frequencies	121
4.3	Logarithm of the relaxation time versus reciprocal temperature for a crystal of BGO doped with Cr. The dashed line corresponds to the undoped BGO crystal	124

		Page
4.4	Logarithm of the relaxation time versus reciprocal temperature for a Zn doped crystal of BGO	125
4.5	Normalized attenuation as a function of reciprocal temperature for the Cr doped BGO sample at two frequencies	127
4.6	Attenuation as a function of temperature and frequency for the transverse (110,001) mode in (BGO + Al).	129
4.7	Attenuation for the transverse (110,001) mode in BGO doped with Ga	131
4.8	Attenuation for the transverse (110,001) mode in a crystal of BGO + (Pb)	132
4.9	Attenuation as a function of temperature in BGO + (P + Ga) for the transverse (110,001) wave	133
4.10	Attenuation in BGO + (Ga + Cr) crystal as a function of temperature and frequency	134
4.11	Attenuation as a function of temperature for all doped BGO crystals	136
4.12	Ultrasonic attenuation of longitudinal waves (111,111) in undoped and doped BSO crystals	137

		Page
4.13	Optical absorption versus photon energy for undoped and doped BGO	140
4.14	Optical absorption coefficient at liquid nitrogen temperature for undoped and doped BSO	141
4.15	Effect of irradiation on optical absorption in BGO	144
4.16	Block diagram of experimental set up for annealing	147
4.17	Raw data plot for attenuation of the longitudinal (111,111) mode in undoped BGO	148
4.18	Raw data plot for attenuation of L(111,111) mode in vacuum annealed BGO	148
4.19	Raw data plot for attenuation of L(111,111) mode in oxygen annealed BGO	148
4.20	Attenuation for the transverse (110,001) mode in an annealed sample of Cr doped BGO	150
4.21	Logarithm of the relaxation time versus reciprocal temperature for the annealed (BGO + Cr) sample	152
4.22	Attenuation for the transverse (110,001) mode in γ-irradiated BSO	154
4.23	Logarithm of the relaxation time versus reciprocal temperature in γ-irradiated BSO	156
4.24	Effect of irradiation on attenuation	157

		Page
5.1	Log-log plot of attenuation versus temperature	170
6.1	Plot of defect concentration versus λ for BGO	181
6.2	Plot of defect concentration versus λ for BSO	182
6.3	Lattice constant as a function of ionic radius for various crystals with structure $Bi_{12}MO_{20}$	184
6.4	A graph showing the relation of bismuth content in the melt and the crystal	188
6.5	Diagram of a trigonal defect	190

TABLES

		Page
1.1	Lattice constants of various compounds of type $Bi_{12}MO_{20}$	3
1.2	Physical constants for BGO/BSO	8
1.3	Ge-O distances in the tetrahedra GeO_4	8
1.4	Site symmetries of various atoms	13
1.5	Elasto-piezo-dielectric matrix	17
1.6	Elastic constants	20
1.7	Acoustic wave velocities	22
3.1	Selection rules for anelastic relaxation	65
3.2	Peak attenuation and peak temperatures for various modes and frequencies	92
3.3	Activation energies and attempt frequencies for different modes	104
3.4	Relaxation strengths for various modes	108
3.5	Effective elastic and compliance constants for various modes	109

		Page
4.1	Doped BGO samples, dopant concentrations and effects of dopants	118
4.2	Peak attenuation and temperature for doped BGO crystals	122
4.3	Activation energies and attempt frequencies, for doped BGO	126
4.4	Attenuation as a function of temperature and frequency. Effect of irradiation on attenuation	155
5.1	Attenuation as afunction of dopant and frequency at 100 K	168
6.1	Activation energy, attempt frequency. and the product $C_0 \lvert\lambda_1-\lambda_2\rvert^2$ for BGO and BSO	178

CHAPTER ONE

BISMUTH GERMANIUM OXIDE AND BISMUTH SILICON OXIDE

Bismuth germanium oxide, $Bi_{12}GeO_{20}$, and bismuth silicon oxide, $Bi_{12}SiO_{20}$ have attracted a great deal of attention because of their potential for use in electrooptic and piezooptic devices. A wide range of work has been carried out to study the elastic and optical properties of these crystals over the past decade.

This thesis presents measurements made on the propagation of ultrasonic waves in undoped $Bi_{12}GeO_{20}$, doped $Bi_{12}GeO_{20}$ and undoped $Bi_{12}SiO_{20}$. Some measurements were also made on annealed $Bi_{12}GeO_{20}$ and γ-irradiated $Bi_{12}SiO_{20}$.

In this chapter a brief review of the history of the material is given. The structure and many other properties related to this work studied by various workers have been discussed. Discussion of other measurements of ultrasonic attenuation is given in Chapter Three.

1.1 History

Bismuth trioxide is known to exist in three modifications as reported by Schumb and Rittner (1943). The commonly occurring α-Bi_2O_3 variety corresponds to the orthorhombic form reported by Gurtler (1903) and the β-Bi_2O_3 or tetragonal phase represents a high temperature modification of the α-phase, first prepared by Sillen (1937). A new form of Bi_2O_3 denoted by γ-Bi_2O_3 was prepared by Schumb and Rittner (1943). They observed that if β-Bi_2O_3 was first placed in a platinum crucible at a temperature of 750-800°C and allowed to cool at a proper rate, a bright yellow product with a body centered cubic lattice, with a_o = 1.025 nm was obtained. But this phase was found to be unstable above 25°C. Later, Sillen and Aurvillius (1945) observed that Bi_2O_3 forms a stable body-centered cubic phase on addition of small amounts of certain metal oxides. A number of isomorphous compounds with formula $Bi_{12}MO_{20}$, where M represents the second metal ion, have been prepared from Bi_2O_3 and Al_2O_3, Fe_2O_3, GeO_2, SiO_2 etc. The lattice constants of these compounds range from 1.010 nm for $Bi_{12}SiO_{20}$(BSO) to 1.023 nm for a compound formed with PbO_2 as given in Table 1.1.

Ballman (1966) while studying bismuth germanate; $Bi_4(GeO_4)_3$, found that small transparent crystals of γ-Bi_2O_3 were formed when bismuth germanate decomposed. The phase diagram of bismuth-trioxide - and germanium

TABLE 1.1 Sillen and Aurivillius's proposed lattice constants of various compounds of type $Bi_{12}MO_{20}$.

Metal	a(nm)	Ionic radius of metal (nm)
Al^{3+}	1.014	0.053
Tl^{3+}	1.015	0.10
Fe^{3+}	1.016	0.067
Bi^{3+}	1.0243	0.10
Si^{4+}	1.010	0.040
Ce^{4+}	1.020	0.102
Zr^{4+}	1.021	0.083
Pb^{4+}	1.023	0.084
Ge^{4+} *	1.0143	0.055

* J.L. Bernstein (1967)

oxide also indicated the formation of a compound at the mole ratio of 6 : 1 (Spranskaya, 1964). Later, large single crystals of $Bi_{12}GeO_{20}$(BGO) were grown by Ballman (1967) from melts prepared at mole ratio of $6Bi_2O_3$: 1 GeO_2. The lattice constant for BGO crystals is also given in Table 1.1.

The Czochralski technique is used for growing large single crystals of BGO, BSO. A detailed description of the method and conditions required for growing good quality crystals is given by Brice (1977). Crystals used in this work were grown by Dr Grabmeier and Oberschmid (1976) using the same method. A brief account of the method is given here. Fig. 1.1 shows the essential parts of the system used by them.

A melt made from weighed amounts of the component oxides (Bi_2O_3 and SiO_2 or GeO_2) are mixed and filled in a rf heated platinum crucible. A seed crystal is placed in contact with the melt and the melt temperature adjusted so that a small amount of the seed melts. To start the growth of the crystal, the melt temperature is slightly lowered and the seed is slowly raised. The seed crystal is continuously rotated during growth to ensure an even temperature distribution and to improve the mixing in the melt. Different diameter crystals can be grown by changing the heat flow into the crystal. Crystals with diameter

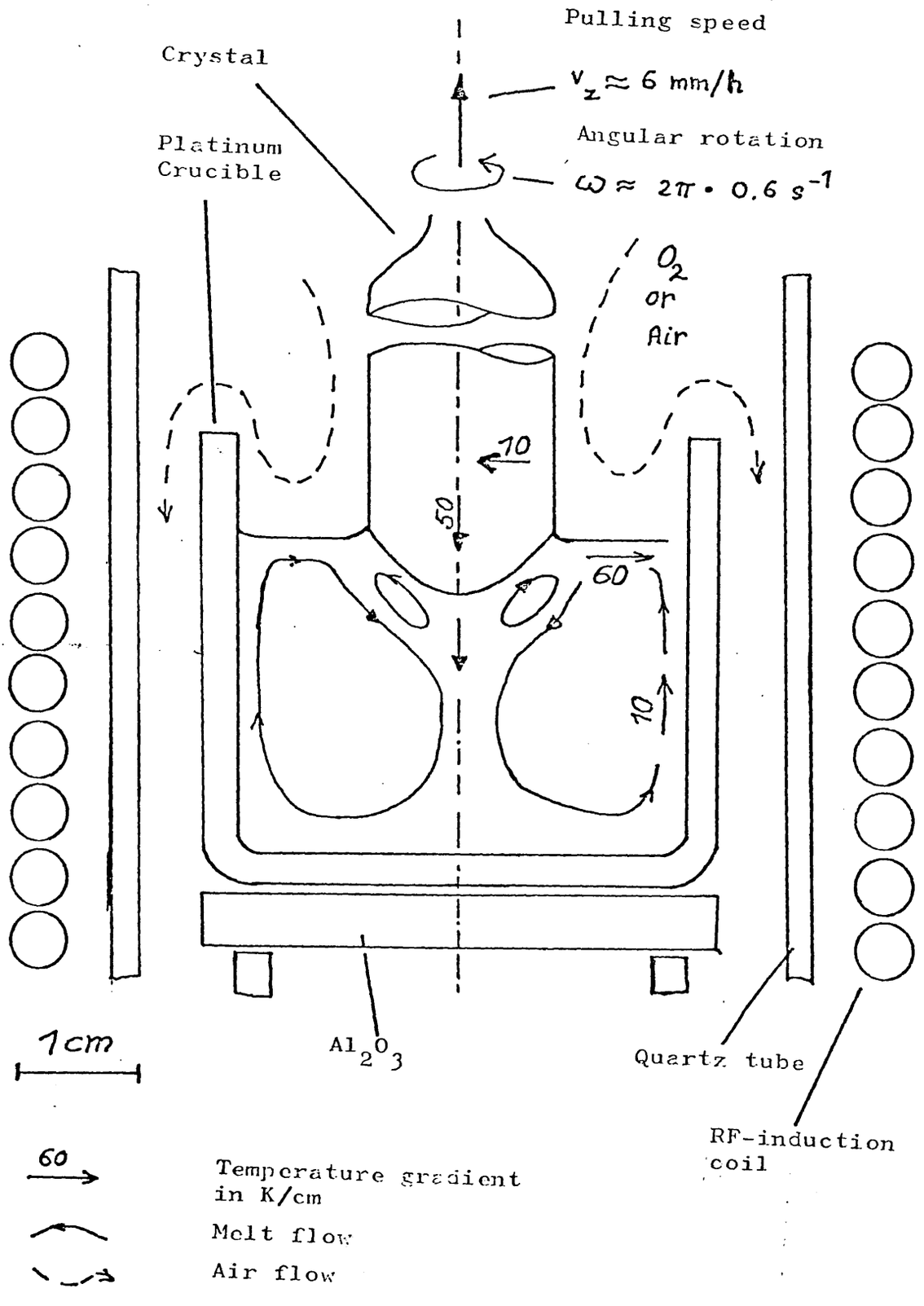

FIG. 1.1 Schematic diagram for growing BGO/BSO Crystals (Oberschmid, 1978)

of about 1 cm can be grown at rates of about 6 mm per hour. Considerable care is needed to avoid cracking of crystals during growth. When the mechanical stress due to the thermal gradient reaches tensile stress, crystals can crack. So, to keep the mechanical tensions as low as possible, crystal diameter is increased slowly in the start and decreased slowly at the end.

Brice and Grabmaier have observed that when the curved face intersects the natural (100) or (110) faces of the crystal, flat regions called facets are formed. The material grown on these facets has been found to be slightly different in colour and a larger lattice constant compared with the rest of the crystal is reported. Clegg and Millet (1974) analysed the crystals grown by Brice and found no difference in the impurity content, on and away from the facets.

Crystals can also be grown with impurities or dopants. A desired amount of the dopant oxide e.g. (Al_2O_3, Ga_2O_3, P_2O_5) is mixed with the component oxides corresponding to the formula $Bi_{12}SiO_{20}$ or $Bi_{12}GeO_{20}$.

Grabmaier (1978) has grown the highly doped crystals at a lower speed of 3 mm per hour and of smaller diameter to avoid cracking.

Pure BGO and BSO crystals are pale and brownish yellow in colour, but even small amounts of dopants have been observed to have considerable effect on the colour. Other effects of dopants are discussed in the following chapters.

1.2 Structure

$Bi_{12}MO_{20}$ (M = Ge, Si) crystals are of body centered cubic symmetry and have space group I23 (Bernstein, 1967). This rare symmetry gives these crystals an unusual mixture of optical and piezoelectric properties. Although several water soluble compounds like $NaClO_3$, $NaBrO_3$ etc. are known, BMO seems to be the first refractory material having this symmetry. A few properties of BGO, BSO are given in Table 1.2.

The overall structure of BGO has been described by Abraham, Jamieson, Bernstein (1967) and of BSO by Abraham, Bernstein, Svensson (1979); in terms of the seven oxygen coordinated bismuth polyhedra which share corners with other identical bismuth polyhedra and with GeO_4 tetrahedra. The four oxygen atoms around each germanium atom form a perfect tetrahedron. The Ge-O or Si-O bond lengths and O-Ge-O or O-Si-O bond

TABLE 1.2 Physical constants for BGO/BSO

	BGO	BSO
Lattice constant a (nm)	1.0143	1.0104
Density (gm cm^{-3})	9.22	9.26
Molecular weight	2901	2857

TABLE 1.3 Ge-O distances in the tetrahedra GeO_4

Crystal	M-O(3) nm	O(3)-M-O(3)
$Bi_{12}GeO_{20}$	1.717 ±0.028	109.47°
$Bi_{12}SiO_{20}$	1.647 ± .005	109.47°

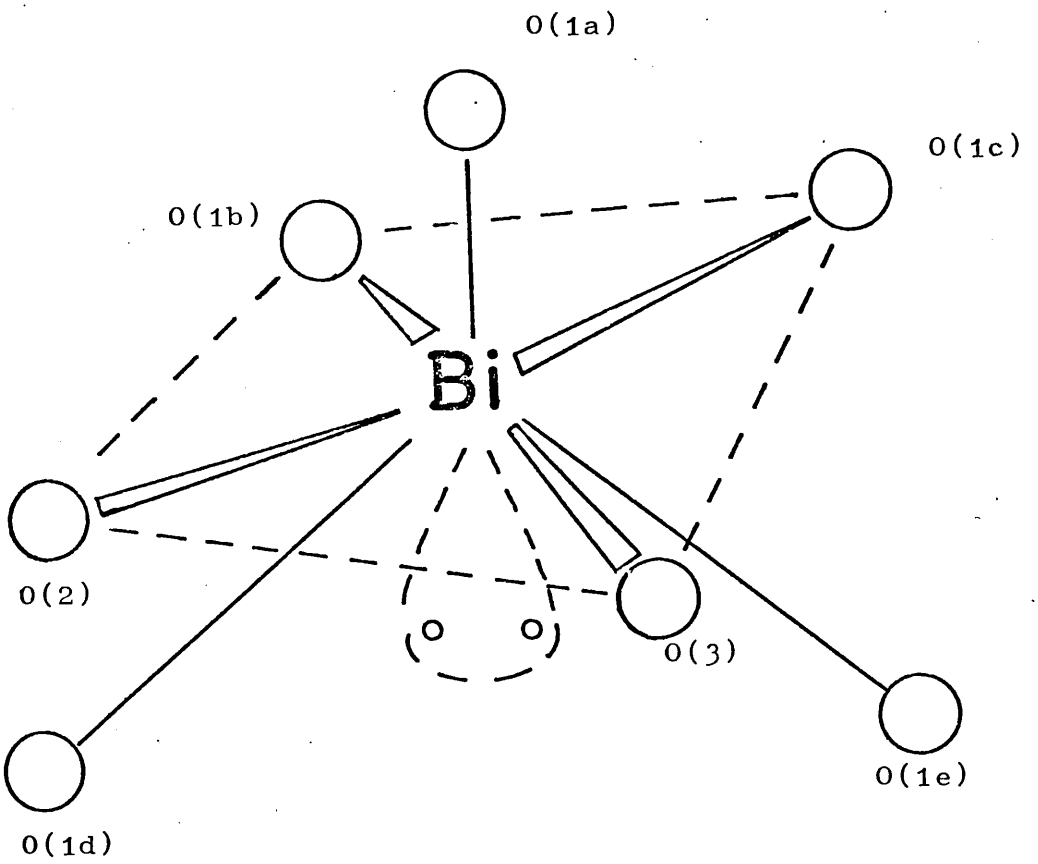

FIG. 1.2 Heptacoordinated bismuth in $Bi_{12}GeO_{20}$ (Abraham et al, 1967)

angles are as given in Table 1.3. The arrangement of the first coordination shell around a bismuth atom is as in Fig. 1.2.

Each bismuth atom is surrounded by four oxygen atoms lying nearly in a plane, and shares two oxygen atoms with a second bismuth atom. Figure 1.3 shows all Bi-atoms and GeO_4 tetrahedron within a unit cell.

Two GeO_4 tetrahedra connected by means of two Bi-polyhedra are shown in Fig. 1.4. The site symmetries of Bi, Si or Ge and the three inequivalent oxygen atoms are as given in Table 1.4.

By studying the temperature dependence of the optical rotatory power from 1.3 to 500 K (melting point $\sim$1223 K) Tanguay (1977) has concluded that there is no crystallographic phase transition over this temperature range.

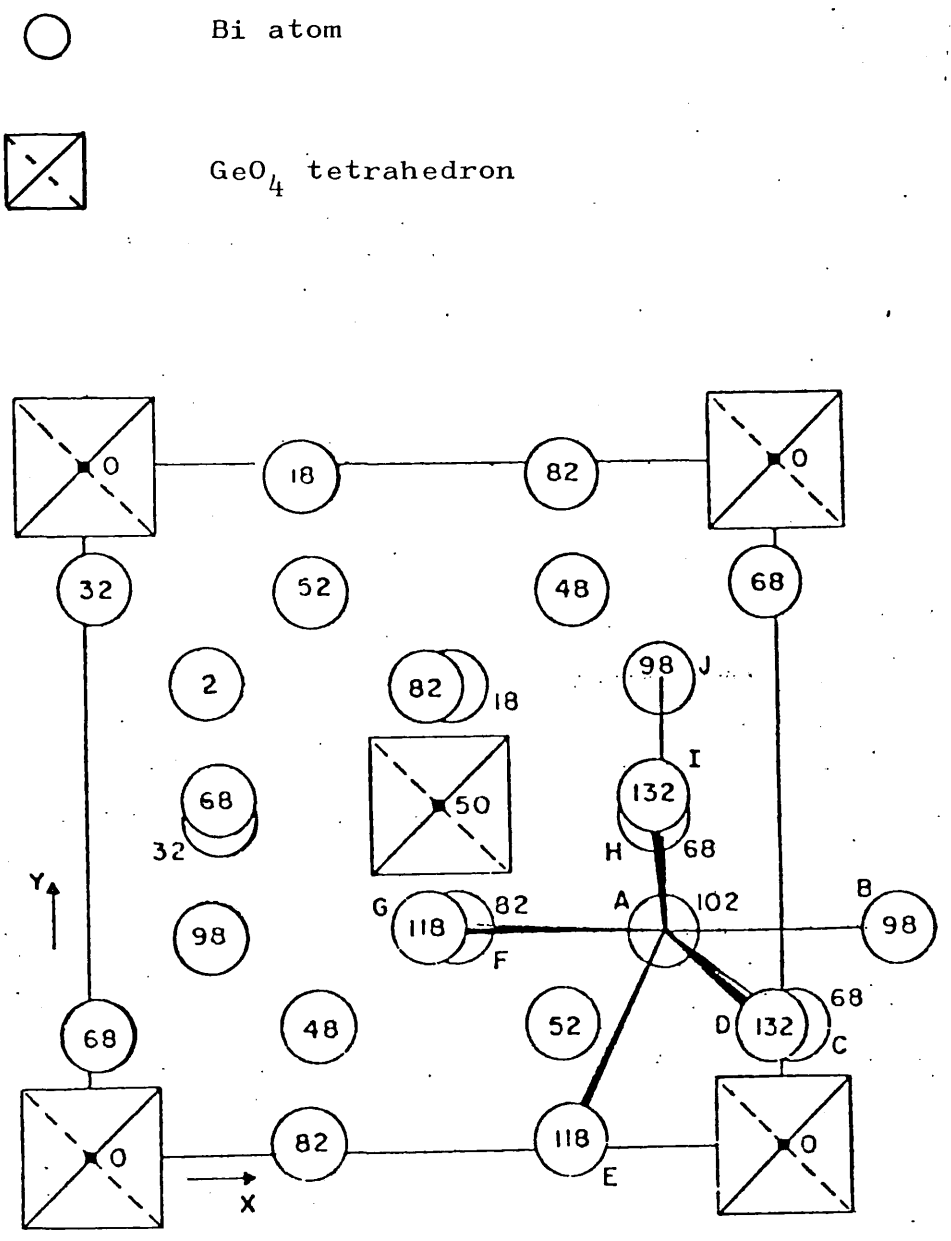

FIG. 1.3 Arrangement of bismuth atoms and GeO_4 tetrahedron in unit cell of BGO

(Nos. correspond to z-coordinates x100)

■ Bi atom

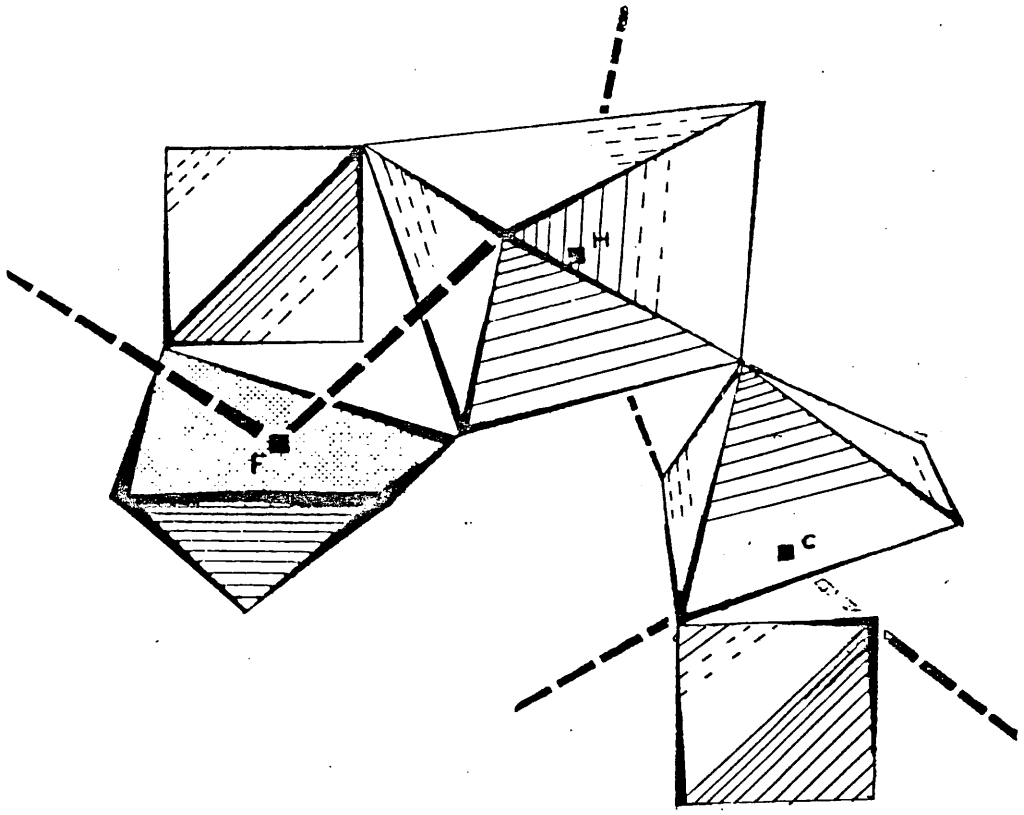

FIG. 1.4 Connection of two GeO_4 tetrahedra by means of two Bi-polyhedra

TABLE 1.4 Site symmetries of various atoms

Atom	site of symmetry *
Si (Ge)	a(23)
Bi	f(1)
O(1)	f(1)
O(2)	c(3)
O(3)	c(3)

* a,f,c are Wycoff notations corresponding to cubic,monoclinic and trigonal site symmetries. Brackets give the International Symbols for these symmetries.

1.3 Stochiometry

The formula $Bi_{12}MO_{20}$ describes the ideal or stochiometric species in which particular cationic and anionic sites in the bcc cell are fully occupied. If Bi : M ratio differs from 12 : 1, or if M is other than a quadrivalent ion, then the bcc structure must contain fractionally occupied ionic sites or else accommodate the change in stochiometry in some other way.

While refining the structure of BGO, Abraham et al (1967) deduced that only Bi atom has anisotropic motion in the crystal and obtained the occupancy factor at the Ge sites to be $0.91 \pm .084$. But in their recent work (Abraham, Bernstein, Svensson, 1979), the occupancy factor is reported to be $0.87 \pm .02$ for Ge and $0.87 \pm .08$ for Si.

The bcc cubic structure with formula $Bi_{12}MO_{20}$ is known to accommodate a variety of different M atoms with radii between 0.025 nm and 0.079 nm. Craig and Stephenson (1975) have studied two mixed oxides, $Bi_{25}FeO_{40}$ and $Bi_{38}ZnO_{60}$, with body centered cubic structure, which involve Bi_2O_3.

By X-ray studies they observed a higher electron population than expected at tetrahedral sites which were supposed to be occupied by Zn and Fe respectively.

After a detailed analysis they suggested that γ-Bi_2O_3 structure can contain some Bi^{5+} ions in addition to Bi^{3+} ions, and these Bi^{5+} ions may occupy some of the tetrahedral sites to provide the higher occupancy observed at these sites.

Brice, Hill (1977) and Grabmaier, Oberschmid (1978) have observed that BSO, BGO crystals can be grown with melt compositions Bi_2O_3 : GeO_2 or SiO_2 varying from 5 : 1 to 7 : 1 without largely affecting its properties. Describing BSO as $Bi_xSiO_{1.5x+2}$, Brice and Hill have reported that if x in the melt was varied from 10 to 14, x in the solid varied from 11.77 to 12.05. They also observed that the maximum and minimum values of x in the solid did not correspond to the maximum and minimum values in the melt.

These observations suggest that BGO, BSO can have Ge, Si or Bi vacancies in the lattice.

1.4 Piezoelectricity

BGO, BSO crystals lack a centre of symmetry and are thus piezoelectric. Since BGO (BSO) is a cubic crystal of class 23, it has only one independent piezoelectric constant, $e_{14} = e_{25} = e_{36}$ (Nye, 1957), as shown in the elasto-piezo-dielectric matrix given by Table 1.5. e_{14} has a value 0.987 $m^{-2}C$.

The origin of piezoelectricity and its resulting polarity in BGO (BSO) has been explained by Abraham, Bernstein and Jamieson (1967); Abraham, Bernstein and Svensson (1979), considering a single GeO_4 or SiO_4 tetrahedron. The four oxygen atoms are required to lie on unit cell body diagonals by symmetry as in Fig. 1.5. The total electric dipole moment associated with a GeO_4 (SiO_4) tetrahedron in the absence of stress is zero. The component along a body diagonal is given by

$$\mu_{\overrightarrow{Ge-O}} + 3\mu_{\overrightarrow{Ge-O}} \text{ Cos } 109.47^{o}$$

$\mu_{\overrightarrow{Ge-O}}$ is the electric dipole of the Ge-O bond. A compressive stress applied along a body diagonal reduces the tetrahedral angle to $109.47-\delta^{o}$. Therefore a net electric dipole moment is generated, with a sense $+\rightarrow-$ from the Ge atom to the face as shown in Fig. 1.5.

TABLE 1.5 Elasto-piezo-dielectric matrix

σ						E		
c_{11}	c_{12}	c_{12}	0	0	0	0	0	0
c_{12}	c_{11}	c_{12}	0	0	0	0	0	0
c_{12}	c_{12}	c_{11}	0	0	0	0	0	0
0	0	0	c_{44}	0	0	e_{14}	0	0
0	0	0	0	c_{44}	0	0	e_{14}	0
0	0	0	0	0	c_{44}	0	0	e_{14}
0	0	0	e_{14}	0	0	ε_{11}	0	0
0	0	0	0	e_{14}	0	0	ε_{11}	0
0	0	0	0	0	e_{14}	0	0	ε_{11}

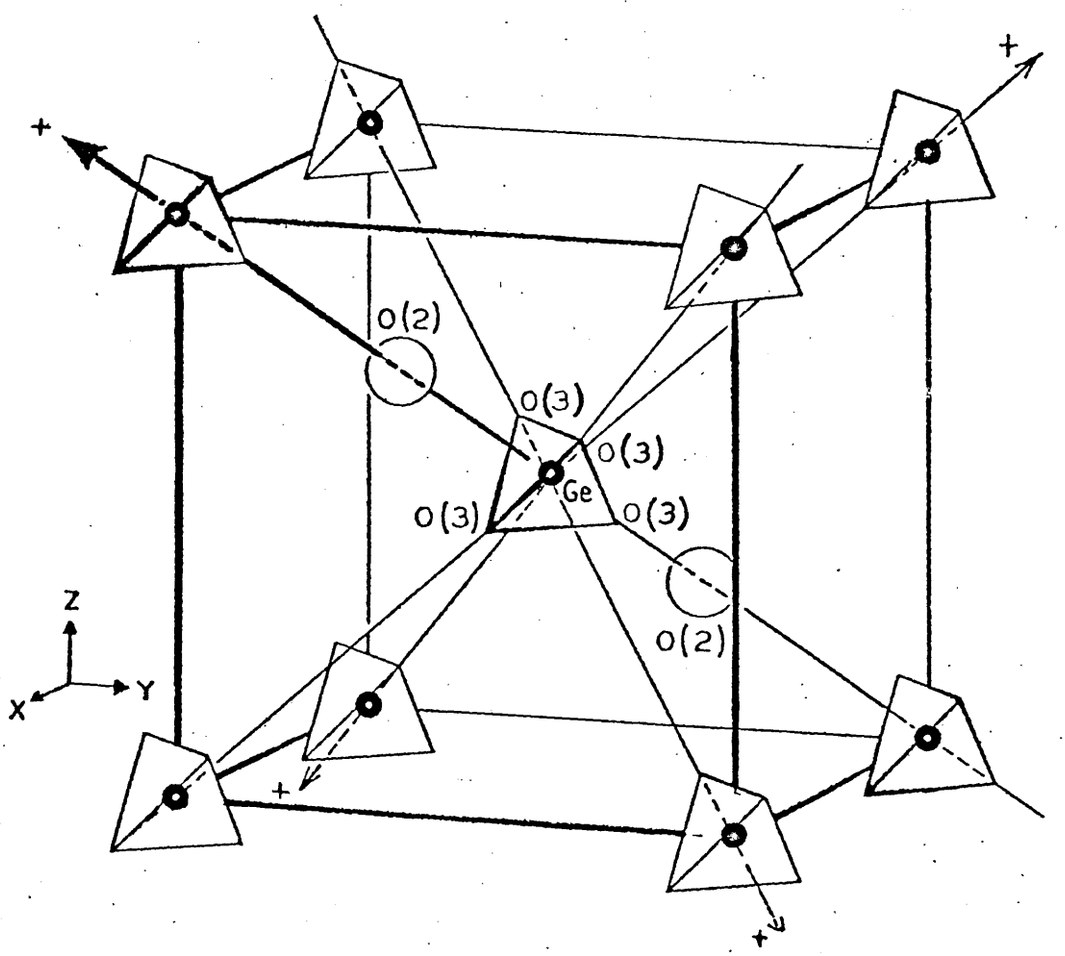

FIG. 1.5 A unit cell of BGO showing the tetrahedra around each Ge atom

1.5 Elastic properties

Since BGO, BSO are cubic crystals belonging to Class 23, it can be seen from the Nye matrix given in Table 1.5 that they have only three independent elastic constants:

$$c_{11} = c_{22} = c_{33}, \quad c_{12} \text{ and } c_{44}$$

and one independent dielectric constant. Various values obtained for elastic moduli at room temperature are given in Table 1.6.

In general, along any direction of propagation, there are three elastic waves each of which is neither a pure shear nor a pure longitudinal. However, in certain directions of symmetry pure longitudinal and pure shear waves can be obtained.

The velocities of transverse and longitudinal waves are determined by the elastic constants and for pure modes they can be expressed in terms of symmetrized elastic moduli given by:

$$c_a = 1/3(c_{11} + 2c_{12})$$

$$c_e = 1/2(c_{11} - c_{12})$$

$$c_t = c_{44}$$

The propagation of high frequency stress waves in a piezoelectric crystal produces electromagnetic waves

TABLE 1.6 Elastic constants

Constant	Slobodnik et al (1971) $10^{11}N/m^2$	Kraut et al (1970) $10^{11}N/m^2$	Onoe et al (1967) $10^{11}N/m^2$	Zelenka (1978) $10^{11}N/m^2$
c^E_{11}	1.28	1.2848	1.20	1.206
c^E_{12}	.305	.2942	.39	.1443
c^E_{44}	.255	.255	.25	.2626

that accompany the stress waves, and vice versa. The presence of electromagnetic waves coupled to the stress waves leads to an increase in the effective values of the relevant elastic constants or piezoelectric stiffening of the crystal. For all these stiffened modes, adding the piezoelectric stress constant and the dielectric constant ε^{s}_{11}, the velocities for various modes studied are given by Table 1.7. The values given in Table 1.7 agree with our measured values to within $\pm$ 0.004 $\times 10^{5}$ m s^{-1}. The relative dielectric constant is 40 for BGO and 56 for BSO.

TABLE 1.7 Acoustic wave velocities for various modes

Orientation	Mode	ρv_s^2	Velocity * 10^5 cm/sec
111	Longitudinal	$c_a + \frac{4}{3} c_t + \frac{4}{3} \frac{e_{14}^2}{\varepsilon_{11}^s}$	3.332
110	Transverse T_1	$c_t + \frac{e_{14}^2}{\varepsilon_{11}^s}$	1.706
100	Transverse	c_t	1.646
100	Longitudinal	$c_a + \frac{4}{3} c_e$	

* Onoe et al (1967)

1.6 Optical properties

Pure BGO, BSO crystals are pale yellow and brownish yellow in colour. Since the band gap is 3.25 eV, which is above the visible range, it shows that there is absorption within the band gap which gives colour to these crystals. The optical absorption in BSO, BGO has been studied by Hou (1972) and Tanguay (1977). The room temperature band gap is assigned at 3.25 eV where the optical absorption coefficient o is 1000 cm^{-1} as shown in Fig. 1.6. A broad absorption shoulder has also been observed in the region 2.3 eV to 3.1 eV with a maximum near 2.7 eV. This shoulder in the optical absorption spectrum has been suggested to be related to the ultrasonic attenuation peaks observed in these crystals. A possible explanation given by Hou and Aldrich (1973) is discussed in the later chapters.

Doping BSO crystals with Al, Ga, B was found, by Hou and Aldrich (1973) and Rehwald, Frick (1976) to strongly effect the optical absorption below the band gap.

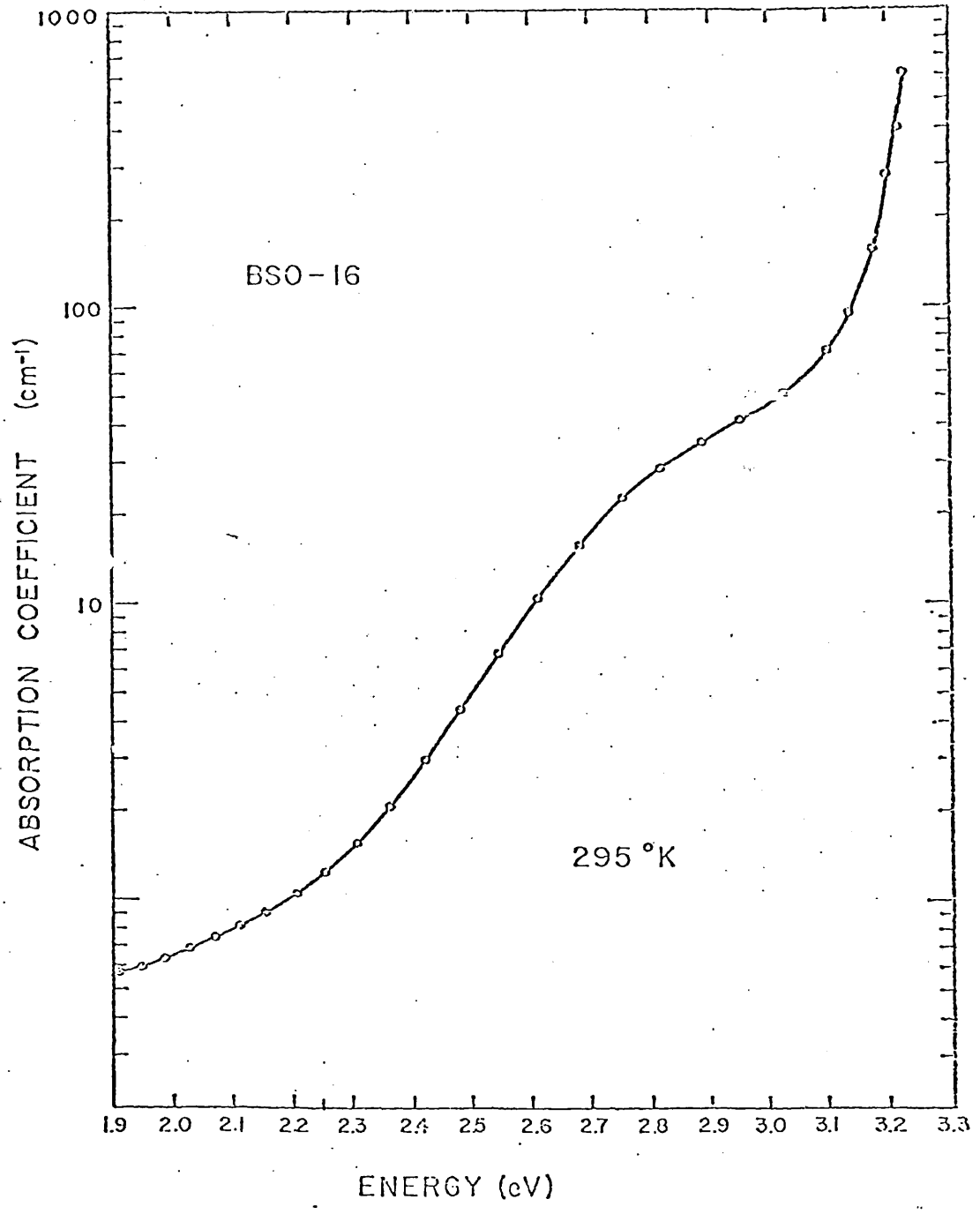

FIG. 1.6 Optical absorption for undoped BSO (Tanguay 197

1.7 Photochromism

Certain boules of $Bi_{12}SiO_{20}$ have been noticed by Tanguay (1977), Brice (1977, Feigelson (1977) to change colour from pale yellow to dark yellow shortly after removal from the growth apparatus. These crystals show some additional optical absorption to that mentioned in Section 1.6. Tanguay (1977) and Brice (1977) have conducted a series of experiments to reveal the cause of this effect and from the observations indicated an extrinsic photochromic mechanism, due to the presence of Cr or Mn at levels of 1 ppm or above. The depth of the colour and the resulting photochromic behaviour were noted to correlate quite well with the optical absorption. Oxygen and vacuum annealing have been observed to effect the additional optical absorption and the photochromism. These are discussed in Chapter 4.

1.8 Semiconducting properties

These are intermediate band gap materials having electrical resistivity value of 8×10^{10} Ω cm for BGO and 5×10^{13} Ω cm for BSO (Aldrich and Hou, 1971). The dark conductivity is p type.

The spectral response of the photocurrent was measured by Aldrich and Albova (1977) for BSO and by Douglas, Zitter (1967) for BGO. The photoconductivity was found to be dominated by photoinduced electrons. Doping the material with Al has been reported to make the material p-type and holes dominate the photocurrent. The effects of different dopants measured by Oberschmid (1978) have been given in Table 4.1.

1.9 Technical applications

The unusual combination of properties in this material make it a technologically attractive material. The low acoustic wave velocity of BGO has made it an attractive delay line material. Its high coupling factor means low insertion loss, high efficiency acoustic delay lines. A rod of BGO (3mm x 12.5mm) was used by Lea, Butcher and Dobbs (1977) as a low loss delay line, for studying the transverse acoustic impedance of normal liquid ^{3}He. About 5000 echoes could be obtained below 4.2K (Butcher 1978).

The pockels readout optical memory relies for its operation on a combination of properties as photo-conductivity with high quantum efficiency, optical transparency in the visible spectrum, a large die-electric constant, high resistivity and a sizeable electrooptic effect. BGO and BSO are the materials at present which satisfy all these requirements, in addition to ease of growth and control of crystal perfection (Feinleib and Oliver 1972). BSO has been reported to have the highest known photorefractive sensitivity for read-write volume holographic storage (Huignard and Micheron, 1976).

CHAPTER TWO

EXPERIMENTAL TECHNIQUES

In order to study the ultrasonic attenuation in BGO and BSO, detailed measurements were made as a function of temperature, at a number of frequencies and for various sound modes. Measurements were made in the frequency range 10 to 190 MHz over the temperature range 4.2 to 260 K. In this chapter the techniques used for measurements and sample preparation are discussed.

The conventional pulse-echo method was used to measure the ultrasonic attenuation. This method has been described in detail by Truell et al (1969) and its use at low temperatures explained by Dobbs et al (1973). Short duration rf pulses are applied to the sample, or to a transducer, which, as a consequence of the piezoelectric effect causes ultrasonic waves to be propagated through the sample. The pulse sent into the sample is reflected at the opposite end face and it returns to the first face where it is reflected again, the process is repeated a number of times. The ultrasonic wave is detected either at the same end (reflection mode) or at the other end (transmission mode) of the sample. As the ultrasonic wave travels through the sample it is attenuated and a series of exponentially decaying echoes are detected.

2.1 Electronics

Matec (model 9000) attenuation comparator, which has a pulsed oscillator and receiver in the common chassis was used. The Matec 9000 used with a 960 rf series plug-in unit covered the frequency range from 10 to 300 MHz. Operation of Matec has been described in detail by Chick, Anderson, Truell (1960). Fig. 2.1 shows a block diagram of its components. Short bursts of rf energy generated in the plug-in unit were applied to the appropriate transducer or sample. The pulsed oscillator of Matec 9000 provides pulses of .5 μ sec to 5 μ sec duration, with pulse amplitude up to about 200 volts at frequencies from 10 MHz to 300 MHz. The natural piezoelectric properties of the BGO samples were used for generation and detection purposes wherever possible. The returning rf signal from the sample was amplified using a preamplifier (Avantek - low noise amplifier). The amplified signal was then mixed with a local oscillator to obtain an IF (60 MHz) signal, which was amplified and detected. The detected video output was displayed on an oscilloscope screen (Tektronix Type 581, with a Type 81 plug-in adaptor). The receiver associated with model 9000 provides a gain of about 80 dB.

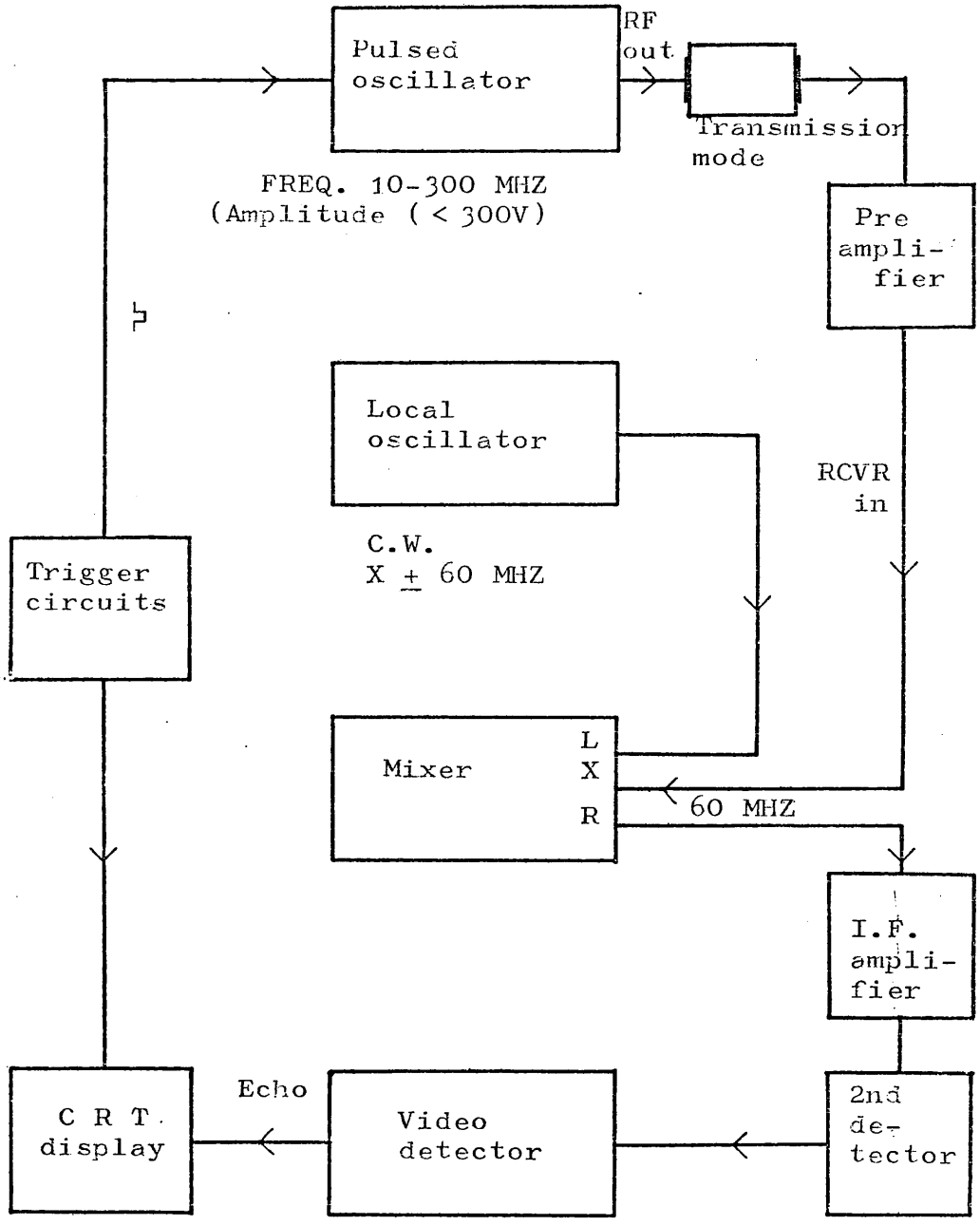

FIG. 2.1 Block diagram of Matec 9000

Absolute measurements are difficult, as the parallelism of the faces is never perfect and so there were some diffraction effects. In all the experiments relative attenuation was measured, by continuous monitoring of echo heights. A 'boxcar' integrator (Brookdeal Linear Gate 9415 and scan delay generator 9425) provided an adjustable gate-width and gave an integrated output of the signal within the selected gate. A particular echo was selected and using a 200 ns wide gate, the integrated output was fed to the y-axis of an x - y plotter to obtain the raw data of attenuation changes with temperature. An integration time of 1 sec was used. Fig. 2.2 shows the complete experimental set-up.

2.1.1 Calibration

The initial pulse has a **stability** of within $\pm$ .05 dB over times comparable to those required to complete a single run. This was checked by recording a single echo under constant conditions.

The amplitude of the recorder was translated into decibels by stopping the recording at least once each run and inserting various attenuators using a calibrated step (Marconi RF attenuator) attenuator. This dropped

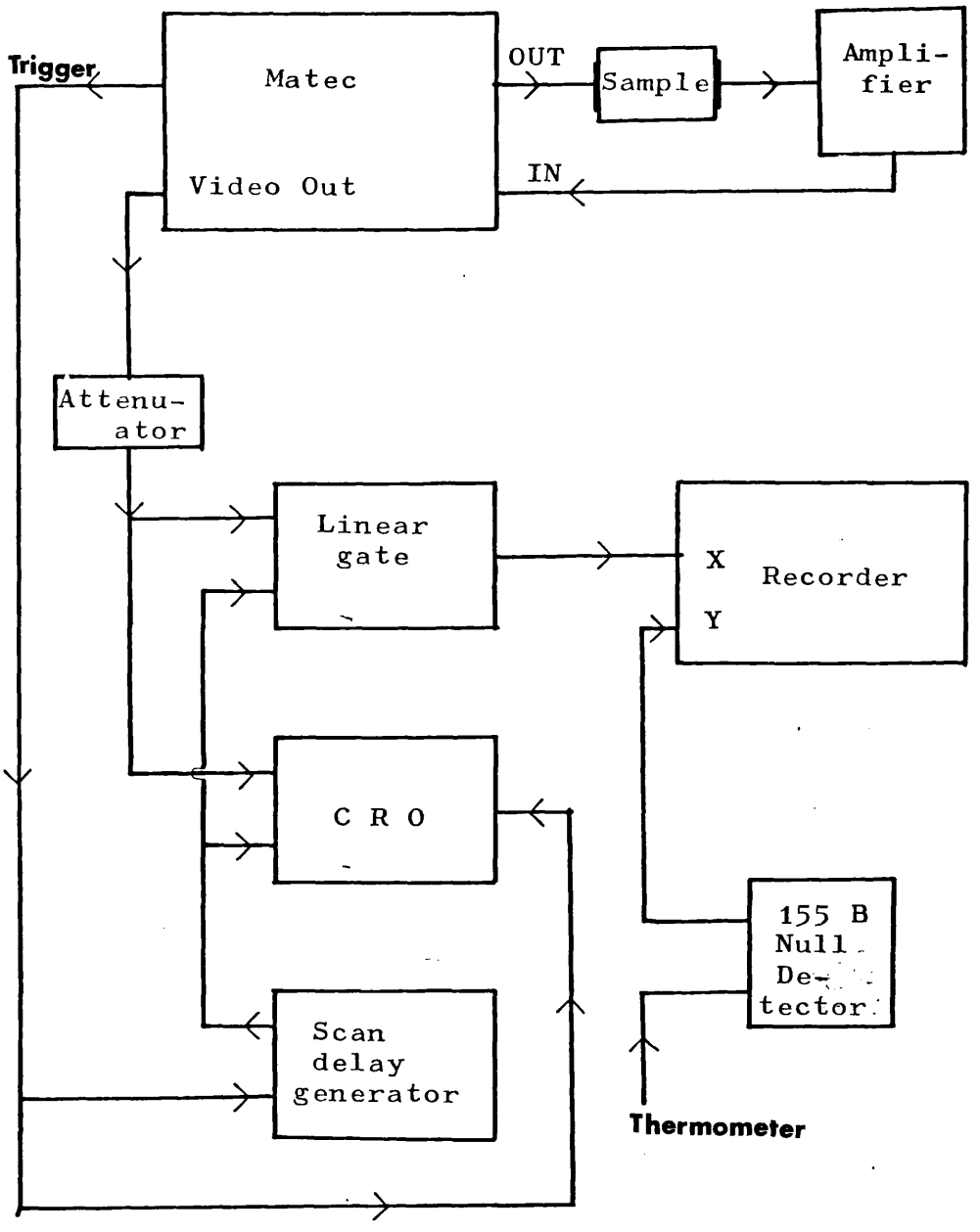

FIG. 2.2 Block diagram of complete experimental set up

the entire echo train by known factors and furnished a scale against which to measure the echo amplitude. The detection system was found to be linear within the dynamic range of 30 dB. Fig. 2.3 shows the echo heights in arbitrary units versus attenuation (dB) inserted.

As a second method for calibration, the output of a Marconi 801D/1 signal generator pulsed by Marconi pulse generator was fed to the Matec receiver system as in Fig. 2.4. The height of the pulse was varied using a precision calibrated attenuator in the Marconi signal generator. The integrated output from Boxcar was read using a 160 B Keithley digital multimeter. The pulse height as a function of dBm is shown in Fig. 2.5. As can be seen from Fig. 2.3 and 2.5, the pulse height V obeys a square law given by $20 \log_{10} V$ down to the noise level. Therefore the attenuation in decibels could be obtained by simply taking $20 \log \frac{V_2}{V_1}$, V_2 and V_1 being the echo heights at two temperatures. The reference for V_1 is the low temperature limit where attenuation is assumed to be zero. The calibration obtained using the two methods were comparable to within $\pm$ .1 dB. The signal to noise ratio was 40 dB.

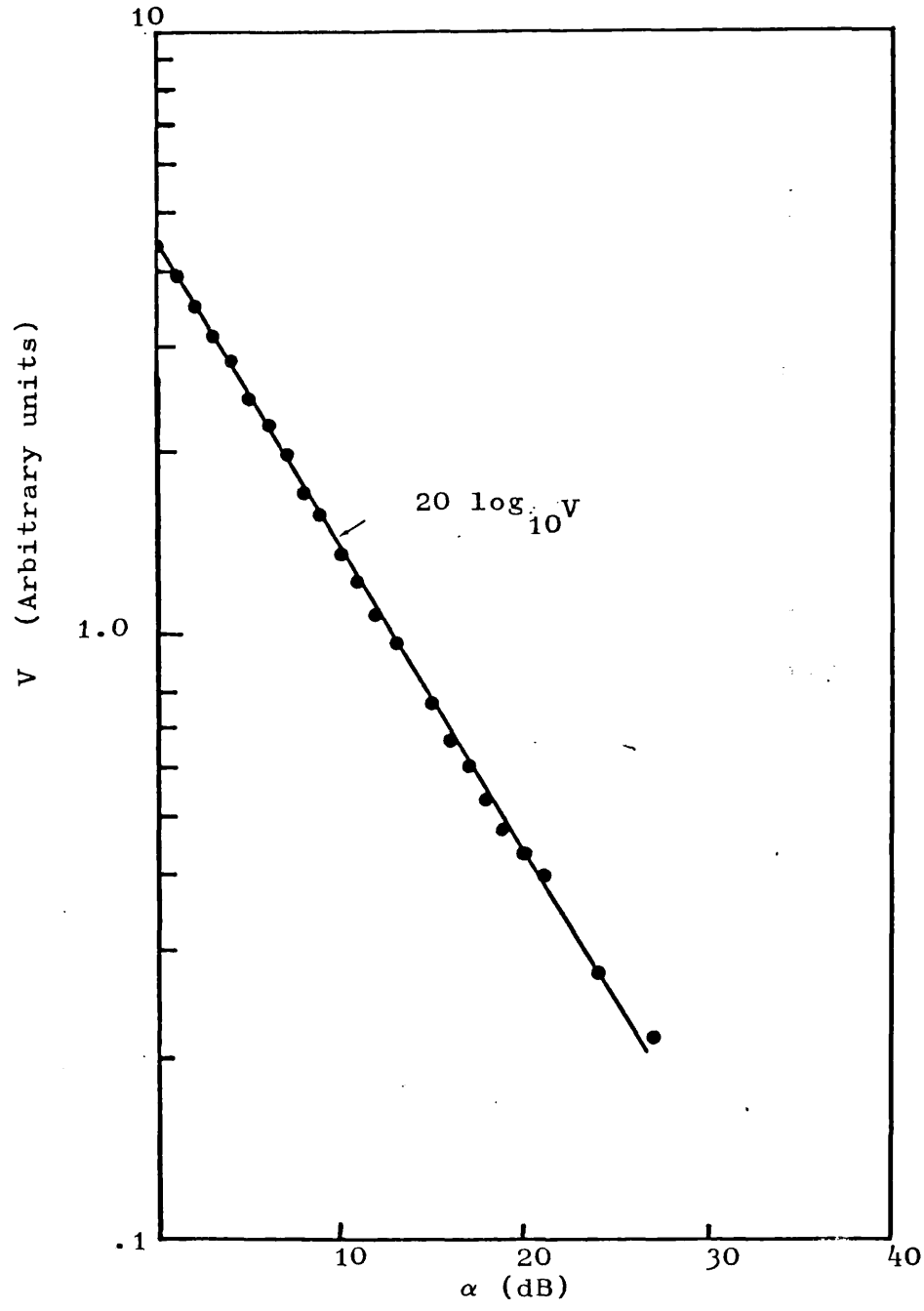

FIG. 2.3 Calibration curve for Matec detector

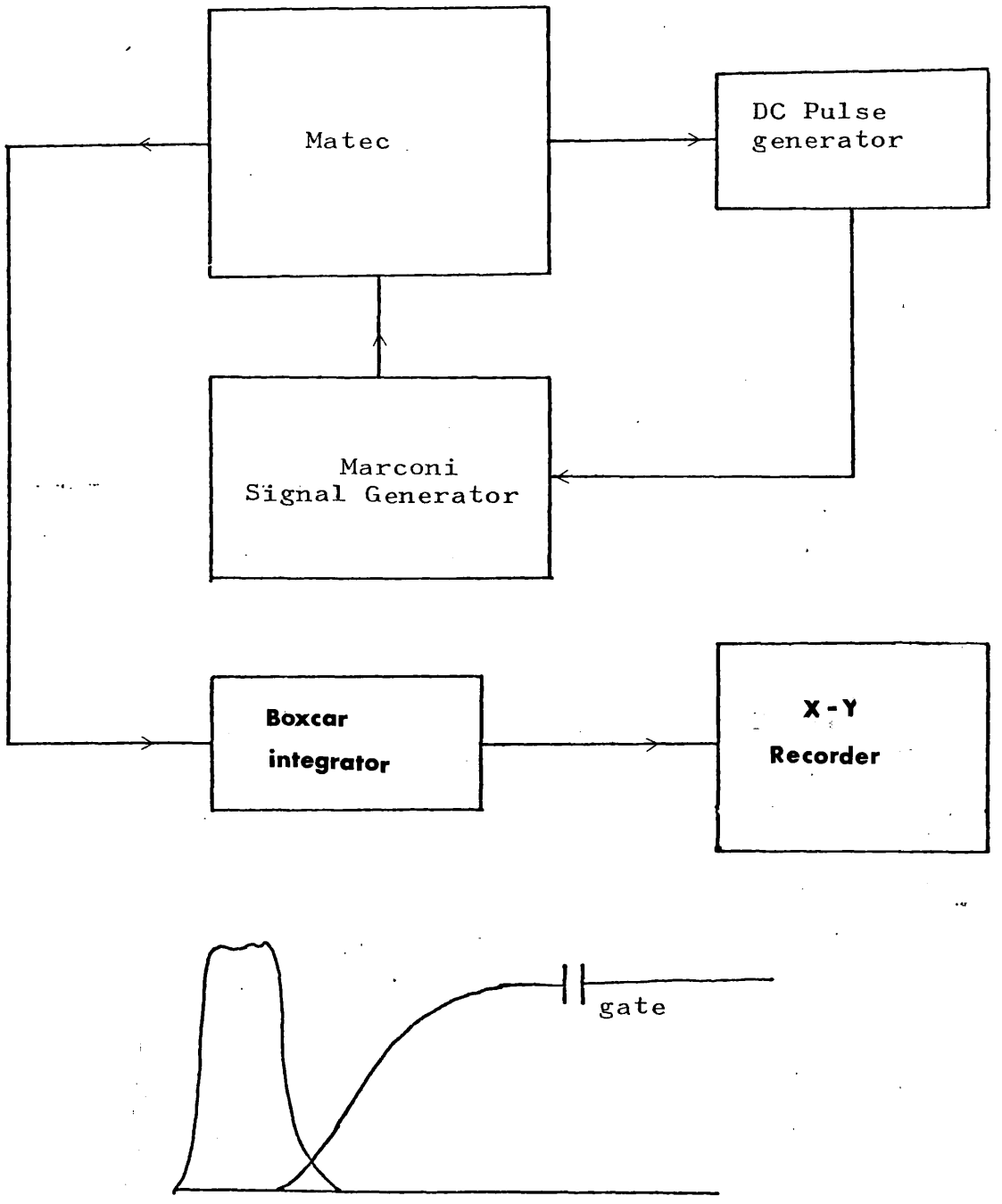

FIG. 2.4 Boxcar echo monitoring

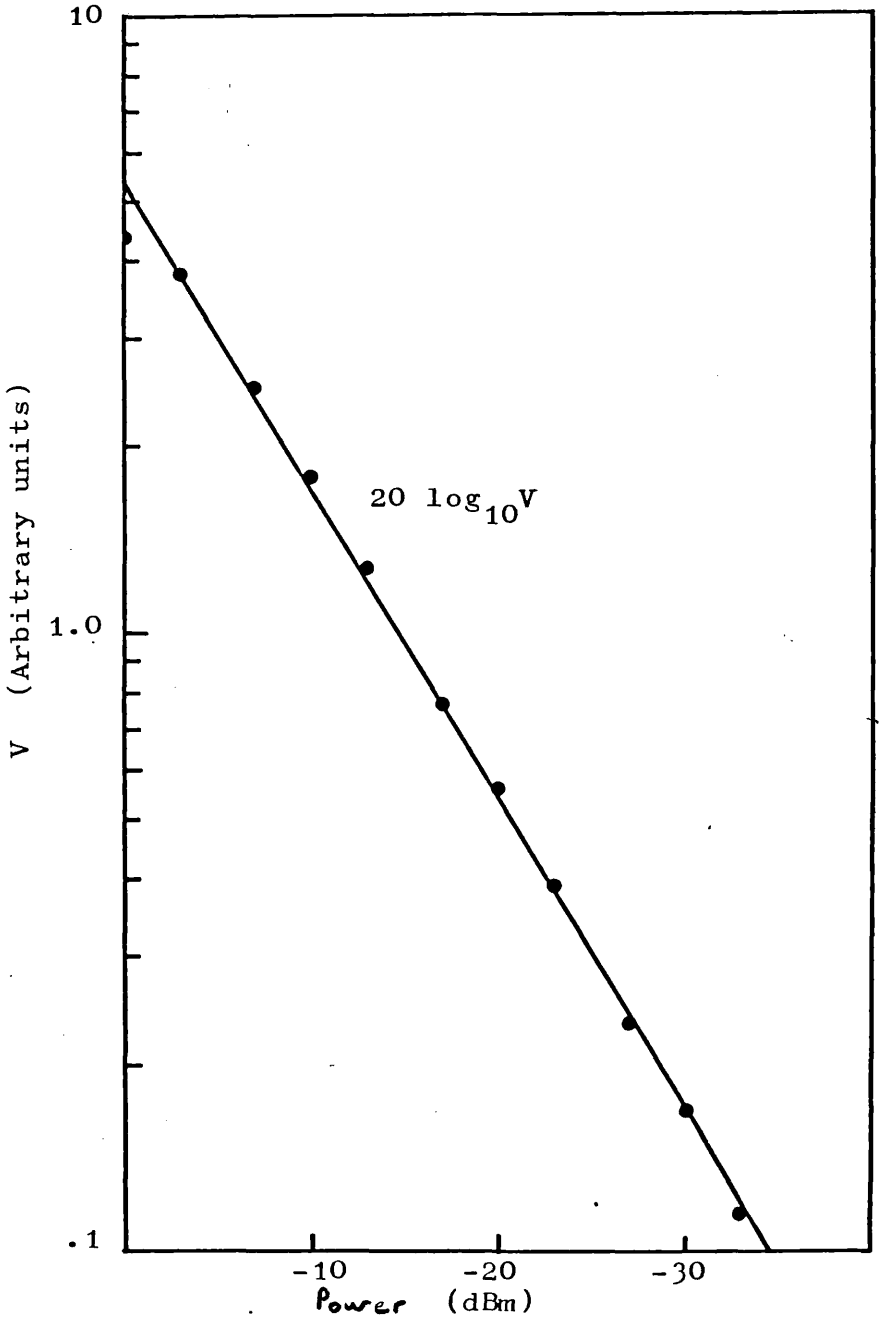

FIG. 2.5 Calibration curve for Matec detector using a Marconi pulse generator

2.2 Transducers, delay rods and samples

2.2.1 Transducers

Sound waves could be directly generated in BGO (BSO) through the piezoelectric effect by surface excitation along certain direction. Using the (111) face, a pure longitudinal mode was obtained and the (1$\bar{1}$0) face provided a shear (110, 00$\bar{1}$) wave. Most of the measurements were carried out on the (110, 00$\bar{1}$) wave. But to study the longitudinal (100, 100) and transverse (100,00$\bar{1}$) modes, quartz transducers were used.

Bonding of the transducers to the sample was a great problem. Initially indium bonding was tried by coating the sample and transducer with indium, using high vacuum coating unit. A jig designed by Dr Hiroshi Tokumoto was used, but no success was obtained with this bonding. Nonaq stopcock grease could not be used, since the experimental space was not evacuated and this grease is extremely hygroscopic. As a last attempt, durofix was tried to make the bond. A small blob of durofix was placed on the cleaned sample surface and the transducer was quickly pressed on to spread the durofix evenly. The whole system was assembled quickly and transferred to the transport dewar for cooling. After obtaining a good bond, it was kept cool as long as measurements were made. The bond lasted thermal cycling 3-4 times and the data for this mode could be obtained.

2.2.2 Delay rods

Measurements were made in both reflection and transmission modes. In the region of very high attenuation only the first echo could be observed. Since the attenuation in this material is extremely large in the temperature region 30-60 K, thinner samples would be useful to obtain the data at higher frequencies. But, using thinner samples decreased the transit time and the first few echoes could not be resolved. Delay rods suitably bonded to the sample could serve the purpose of additional delay. But several delay rods ($LiNbO_3$, quartz, cadium) were tried using different bonding agents, without success. The bonds could not withstand cooling below 77K and resulted in cracking many crystals. This limited the maximum frequency used for measurements to 90 MHZ in the case of large attenuation samples.

2.2.3 Samples

The doped BGO samples used for this work were provided by R Obserschmid and Grabmaier (Siemens, Germany). These crystals were grown by Dr Grabmaier, using the usual Czochralski technique described in Section 1.1.

Table 4.1 gives the list of samples used for measurements. Samples were of various lengths from 2 mm to 6 mm and diameters from 3 to 5 mm.

2.3 Sample preparation

2.3.1 Orientation

Crystals of BGO were received in the form of unoriented boules or discs. Crystals were first oriented using the Philips X-ray set by the Laue back reflection technique. Beam currents of 40 mA at 30 KV incident on a W anode were normally used. Exposure times varied from two to three hours. Crystals could be oriented to within $\pm$ 0.5°. Mounting of the crystals on to the goniometer needed great care. This material being very fragile and thermally sensitive, some cold setting adhesive was required. Dental wax with a low melting point (70° C) was found to be suitable. It provided the bonding strength required with minimum strain on the sample.

An X-ray picture for the <110> direction for BGO is shown on the next page.

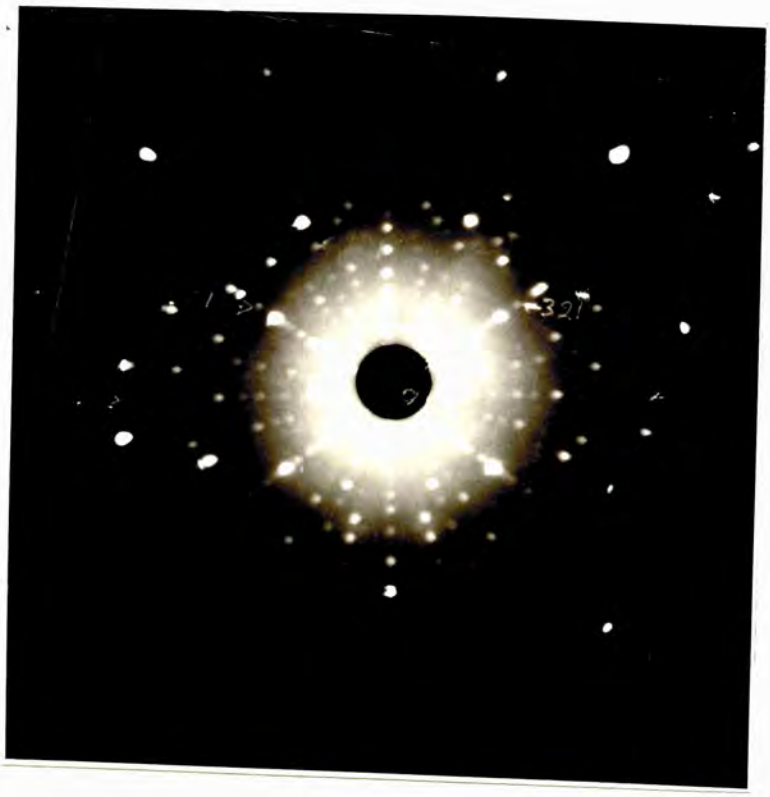

An X-ray picture for <110> direction in BGO

2.3.2 Cutting

A Microslice II annular precision diamond saw was used for cutting the crystals. Samples had to be embedded in dental wax to provide the strength needed to hold the crystal in place while cutting. A speed of 150 - 200 revolutions per minute was used. The diamond blade and sample were continuously cooled with a cutting fluid to avoid cracks due to over heating and friction between the sample and the blade. Normally three to four hours were needed to cut a 5 - 6 mm deep crystal. The samples could be easily removed from the wax. Sample cutting was quite successful using this machine, but a lot of patience was required. After cutting, samples were X-rayed again to check their orientation.

2.3.3 Polishing

Accurately oriented samples, with optically flat faces, parallel to within a few seconds of arc, were needed to obtain a good echo train. The first few samples, which were in the form of small rods, were polished using a Logitech DM2 precision polishing machine. Details of this machine and polishing techniques have been given by Fynn and Powell (1979).

Samples were mounted onto a brass plate which could be screwed on to the precision jig. A very thin layer of dental wax was spread on the brass plate and sample was placed on it and slightly pressed to form a uniform layer. The initial grinding of crystal faces was done using fine grades of silicon carbide grinding paper fixed to a flat glass reference plate. A slurry of silicon carbide powder in Hyprez fluid was used. A 240 and 600 grit silicon carbide papers were used in succession.

The polishing jig is basically a steel cylinder with the base supported by three legs. The legs are waxed into an optically flat steel ring. The brass plate is attached to a spring arrangement on the bottom of the central cylinder. This spring arrangement helps in lowering the sample slowly inside the conditioning ring. The weight of the jig is supported by the ring. The jig stands on the lapping plate and is guided in its motion by a steel arm, which sweeps the jig across the revolving lapping plate.

For finer polishing, diamond paste starting with 10 μm down to 1/4 μm was used, on softer lapping plates. Polishing times of one to two hours were needed to get an estimated surface flatness of $\lambda/10$ of sodium light. After polishing one side, the sample was reversed

and the second face was then polished flat and parallel to the first face. But, since wax was used to hold the samples on the brass plate, perfect parallelism could not be obtained.

Later, small brass jigs were designed, to hold the samples. The two faces of the brass jigs were made flat using the spark erosion machine. Samples were supported in the jig using wax on the sides, so that both faces to be polished were free. Three small pieces of the crystal were fixed with wax on each side of the brass plate. These pieces helped to make polishing quicker, by avoiding polishing of the brass surfaces. Crystals were polished by hand on an optically flat glass plate using successively finer powders. Both faces were polished alternatively and the echoes obtained were checked to see the improvement in parallelism. A parallelism of within 2 sec of arc was obtained. A train of more than 100 echoes could be obtained as can be seen in Fig. 2.6.

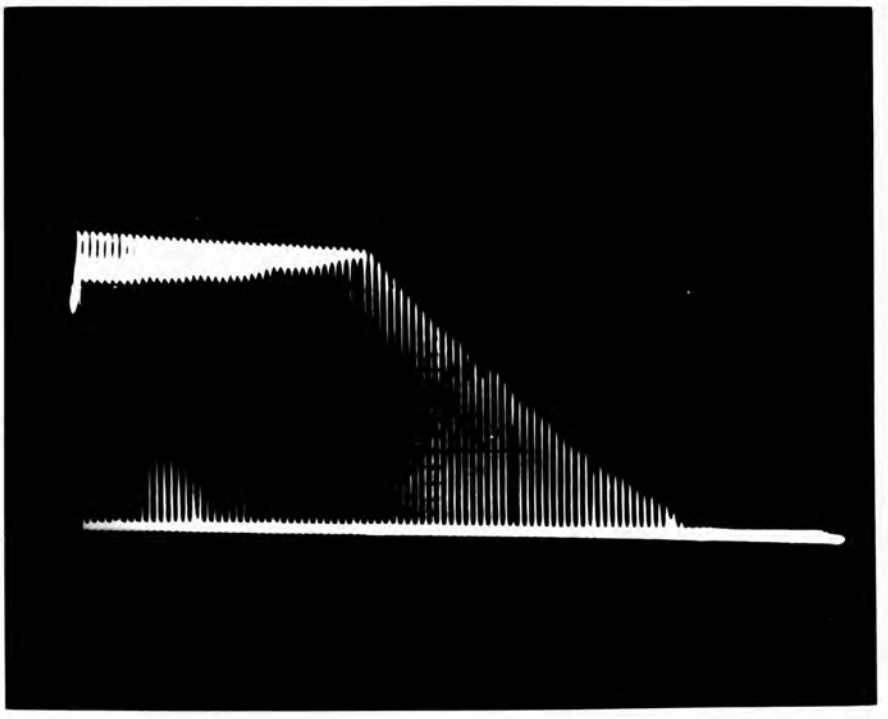

FIG. 2.6 A typical pulse-echo train

2.4 Measurements in the temperature range 4.2 to 300 K

At the start of this work a few experiments were performed by placing the experimental probe in a glass dewar, into which helium could be transferred. But this needed a large amount of helium and the whole system needed precooling with nitrogen. To reduce the cost of running these experiments, a much smaller apparatus was designed, so that the experiment could be carried out in the liquid helium storage vessel. The main problem in this case was the small size of the apparatus required to go through the neck of the storage vessel (diameter 1.95 cm). Fig. 2.7 shows the system used for ultrasonic measurements, which will now be described in detail.

2.4.1 Sonic cell

The sample holders used for ultrasonic measurements at low temperatures are known as sonic cells. Sonic cells used here were constructed from oxygen-free copper. A schematic diagram of the cell is shown in Fig. 2.8. It consists of four parts. The top fixed plate (a) of the shape shown in the figure carried two Cu-Ni coaxial lines for rf in and out to and from

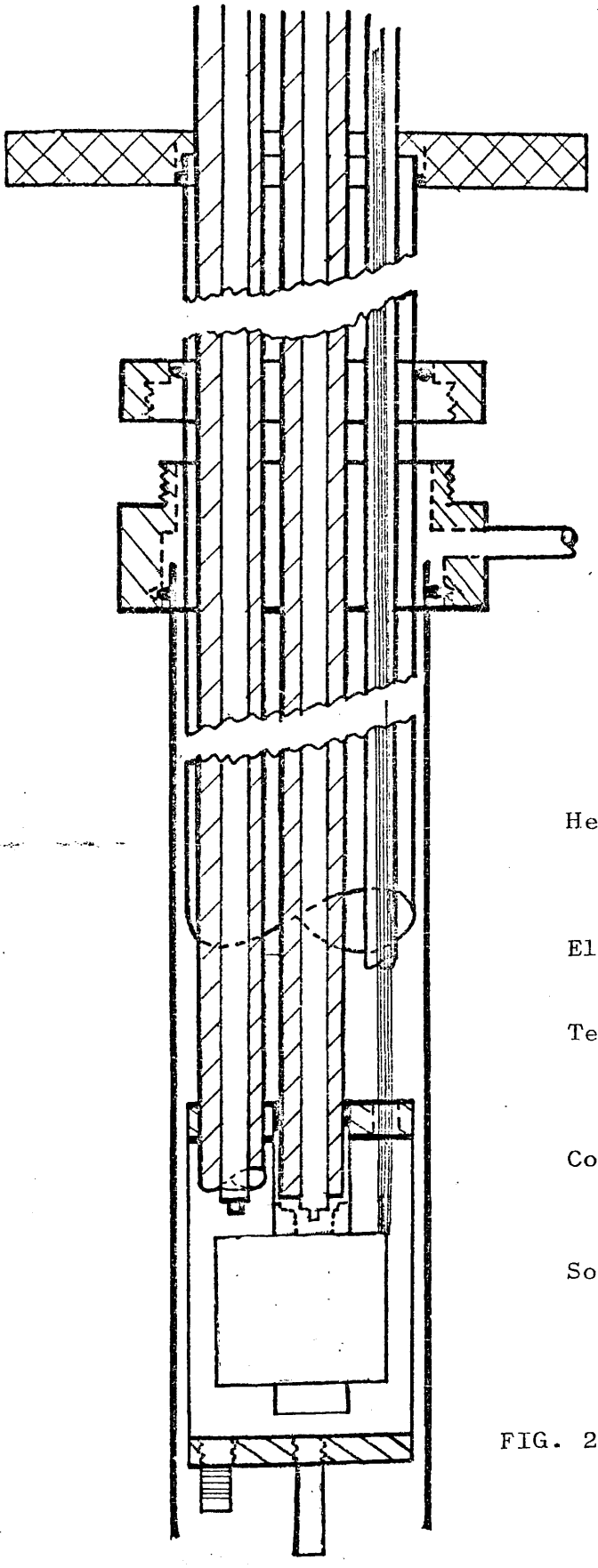

FIG. 2.7 Block diagram of experimental probe

the cell. The thermometer leads were passed through a small hole in this plate. The second plate (b) had a central 5 mm hole to accommodate samples of varying lengths. A 3 mm space alongside the sample space carried the resistor to ensure that the resistor and sample were in good thermal contact. This plate (b) was kept fixed for all the samples to give minimum possible shock to the thermometer. The third plate (c) had a 2 cm diameter stem which carried a mini-coaxial cable for rf out and the thermometer leads were anchored to it using N-grease. For samples smaller in size, special copper plates were machined to locate the samples.

Spring contacts were used to couple rf power to the samples. The contacts were made from small copper discs polished flat and soldered onto the springs made from phosphorbronze. Spring contacts were isolated from the sample holder by teflon spacers. The samples were electrically connected to the cell with silver dag. All these plates had three equally spaced screws (s) to help proper alignment of the cell. The overall diameter of the cell was 1.6 cm.

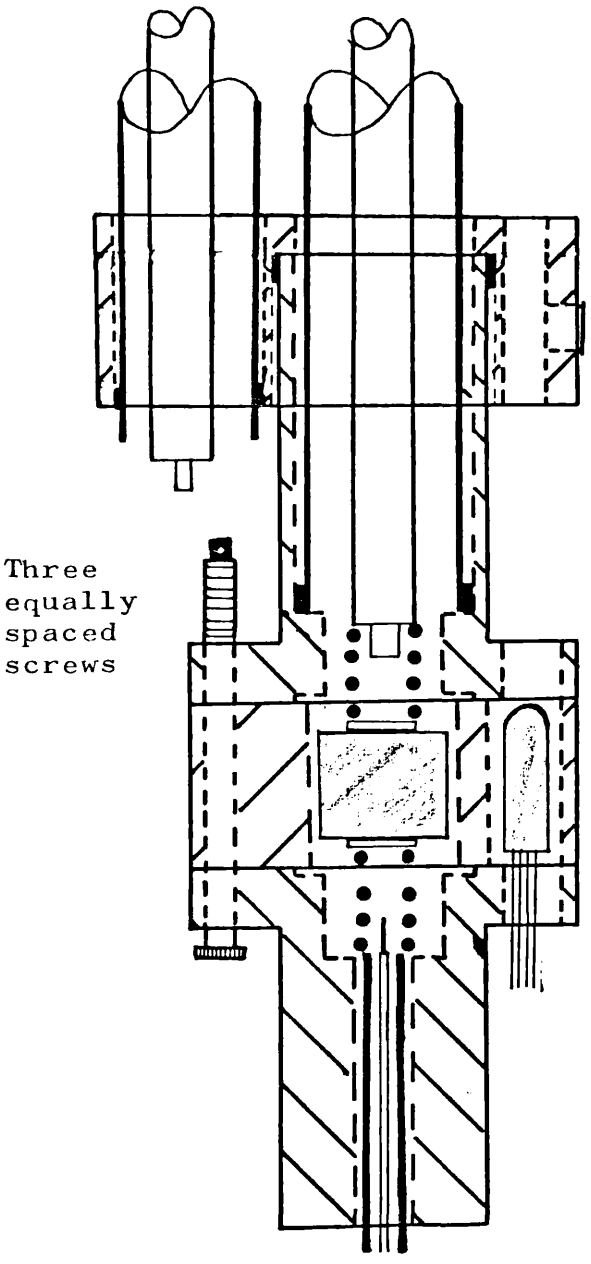

FIG. 2.8 Sonic cell

2.4.2 Coaxial transmission lines

Coaxial transmission lines used for rf into and out from the sample were made from concentric cupronickel tubes. A 2 mm tube (D2) surrounded by a 5 mm tube (D5) and held separated from it using teflon spacers, provided a 50 Ω impedance. Glass to metal seals were used at the top ends to which standard BNC connectors could be fixed. The lower ends of these cables were passed through a copper plate which formed a part of the sonic cell and the outer 5 mm tubes were soldered in place. In this way the coaxial lines also provided a rigid support for the sonic cell. The loss in these lines was less than 1 dB at all frequencies.

2.4.3 Temperature control

The electrical leads were taken down through a thin stainless steel tube. The two coaxial lines and this third tube were passed through a brass plate B and soldered in place. A larger stainless steel tube, T, was slipped over all three tubes and soldered in a small groove in the brass plate as shown in Fig. 2.7. This whole system could slide through a short brass tube D which fits onto the neck of the storage vessel

by means of an O-ring. To make a gas tight seal between D and T, a demountable Edwards coupling E was used, with a neoprene ring. The sonic cell was contained in a very thin walled copper can C (diameter 1.675 cm) which screwed on to the top fixed plate, P. The experimental space is full of helium gas, keeping the temperature throughout the interior of the chamber constant. The apparatus was lowered slowly into the vessel so that it cools gradually. The whole apparatus was balanced using counter weights attached to the plate B through a pulley system.

A copper rod was screwed onto the bottom of the can, C. When the rod dips into the liquid helium, the experimental space is slowly cooled down to the liquid temperature. To raise the temperature above 4.2 K a copper constantan wire (38 swg) wound around the copper rod was used as a heater.

2.5 Thermometry

Due to the limited space available, a carbon-glass thermometer was used for temperature measurements. Extensive literature on low temperature carbon thermometers exists (Clement and Quinnell, 1952). Two types of resistors are mainly used, the carbon radio resistors (Allen-Bradley and Speer resistors) and carbon film resistors. But these are useful mainly below 20 K. In the temperature range from 4.2 to 300 K, carbon-glass resistors are suitable. These first developed by Lawless (1971) at Corning Glass works are quite similar to carbon resistors. It consists of high purity carbon filaments deposited in the voids of a leached borosilicate glass.

2.5.1 Calibration

R(T) for carbon glass resistor is qualitatively similar to that of Allen-Bradley resistor, but sensitivity is higher - $R_{77}/R_{300} \simeq 2$ and $R_{4.2}/R_{300} \simeq 130$. Tests performed by Lawless indicate that reproducibility of the encapsulated models is better and cycling does not give changes significantly greater than $\pm$ 1 mK at 4.2 K. The resistor (CG 638) used in this work

FIG.2.9 Sonic cell

was calibrated against another carbon glass resistor (CG 628) calibrated by Cryotech. The R(T) curve for this sensor is given in Fig. 2.10. It is more sensitive below nitrogen temperature, with resistance going from 41 Ω at room temperature to only 77 Ω at nitrogen temperature, but rises rapidly to 6900 Ω at 4.2 K.

2.5.2 Thermal contact

Thermal heat sinking is very important for all resistor thermometers. Since the carbon glass resistors are constructed so that the sensing element is thermally and electrically isolated from its case, the main thermal input is through the electrical leads, and considerable care was needed to heat sink these leads. The resistor was mounted in a 3 mm diameter space in the sample holder as shown in Fig. 2.9. The thermometer leads made of phosphor bronze and insulated with polyamide were thermally anchored to the copper post of the sample holder using Apiezon-N grease. Electrical leads (44 swg copper) from room temperature were also thermally anchored to the sonic cell before going to the resistor as in Fig. 2.9.

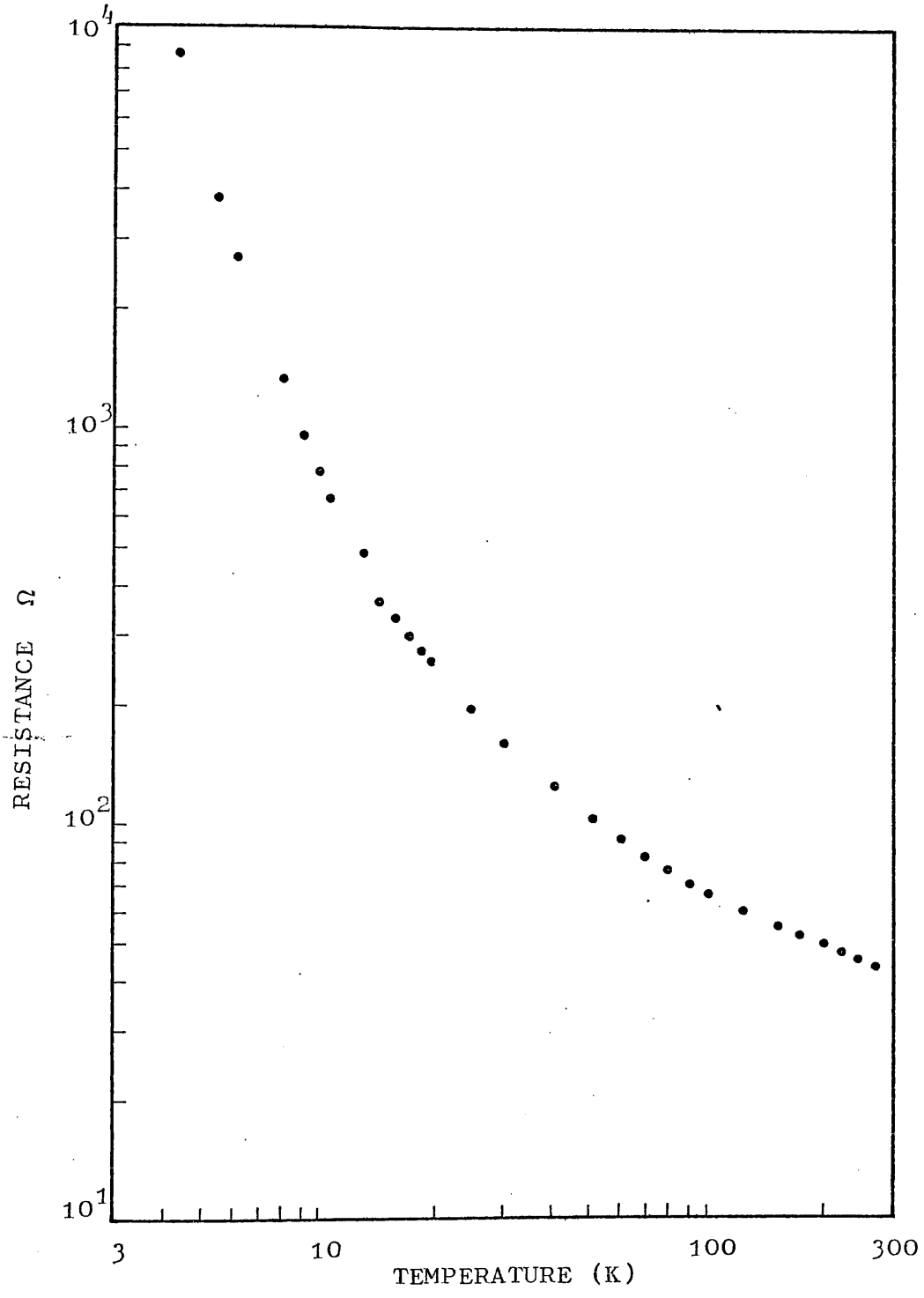

FIG. 2.10 Calibration curve for a carbon glass (CG 638) resistor

A constant current of 1μA was used throughout the temperature range to keep the ohmic heating as low as possible. No heating effects due to stray rf fields were detected.

2.6 Experimental procedure

For a typical run, sample and sonic cell were cleaned and assembled as in Fig. 2.9. To set the rf transmitter at a certain frequency, a Marconi signal generator and a Mixer (Hewlett Packard) were used. The signal generator was set at the desired frequency. The rf output was mixed with the output from the Matec transmitter and the resultant output displayed on a CRO. Frequency of the Matec transmitter was adjusted till there were no beats in the output signal. Using this procedure the frequency could be set to within $\pm$ .1 MHz. After setting the frequency, a pulse from the Matec was applied to the transducer or the sample and the reflected or transmitted signal was received by carefully tuned receiver system. The experimental probe was slowly lowered into the helium vessel.

The integrated output for a particular echo from the boxcar was fed to the Y-axis of the XY recorder. The temperature was measured in terms of resistance. The output from the resistor was amplified using a 155 B Keithley null detector before feeding to the horizontal axis of the plotter. Each run was completed in at least four hours. Less than half a litre of helium liquid was consumed for a single run. No precooling of the system was required and the system proved to be very economical. The thermal reproducibility was found to be very good, as checked by repeating measurements a number of times. Fig. 2.11 shows a typical temperature sweep repeated three times. The amplitude of the echo was converted to dB as described in Section 2.1.1. The value of attenuation at 4.2 K was taken as reference zero. Knowing the length of the crystal and the number of transits through the crystal, attenuation (dB/cm) at various temperatures could be calculated using

$$\frac{\alpha_T - \alpha_{4.2}}{n\ell}$$

where ℓ is the length and n the number of transits.

Resultant data for Fig. 2.11 is shown in Fig. 2.12. To check if there was any temperature dependence of the coupling, the amplitude of at least ten echoes was recorded at a number of temperatures. The

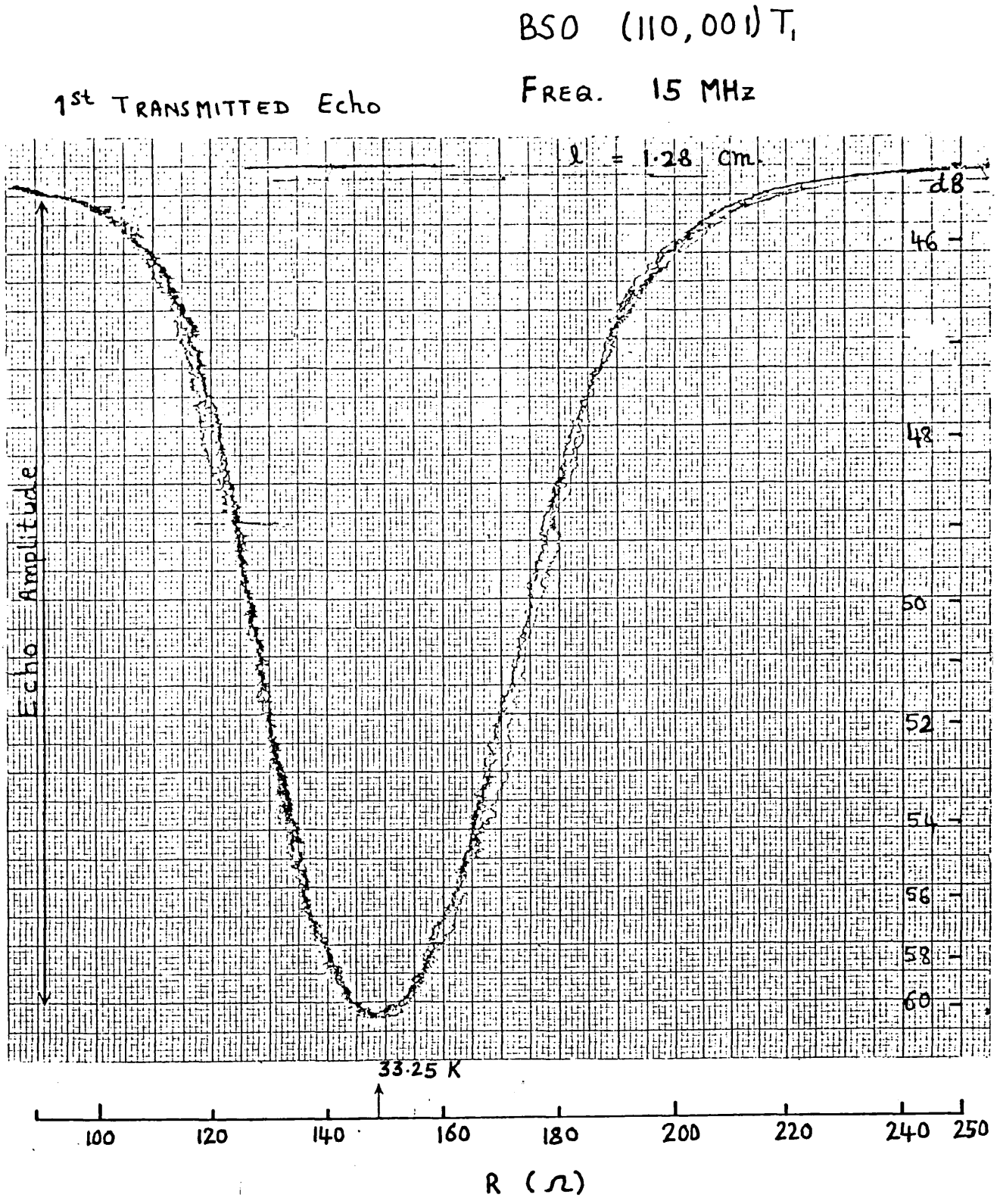

FIG. 2.11 A raw data plot from X-Y recorder

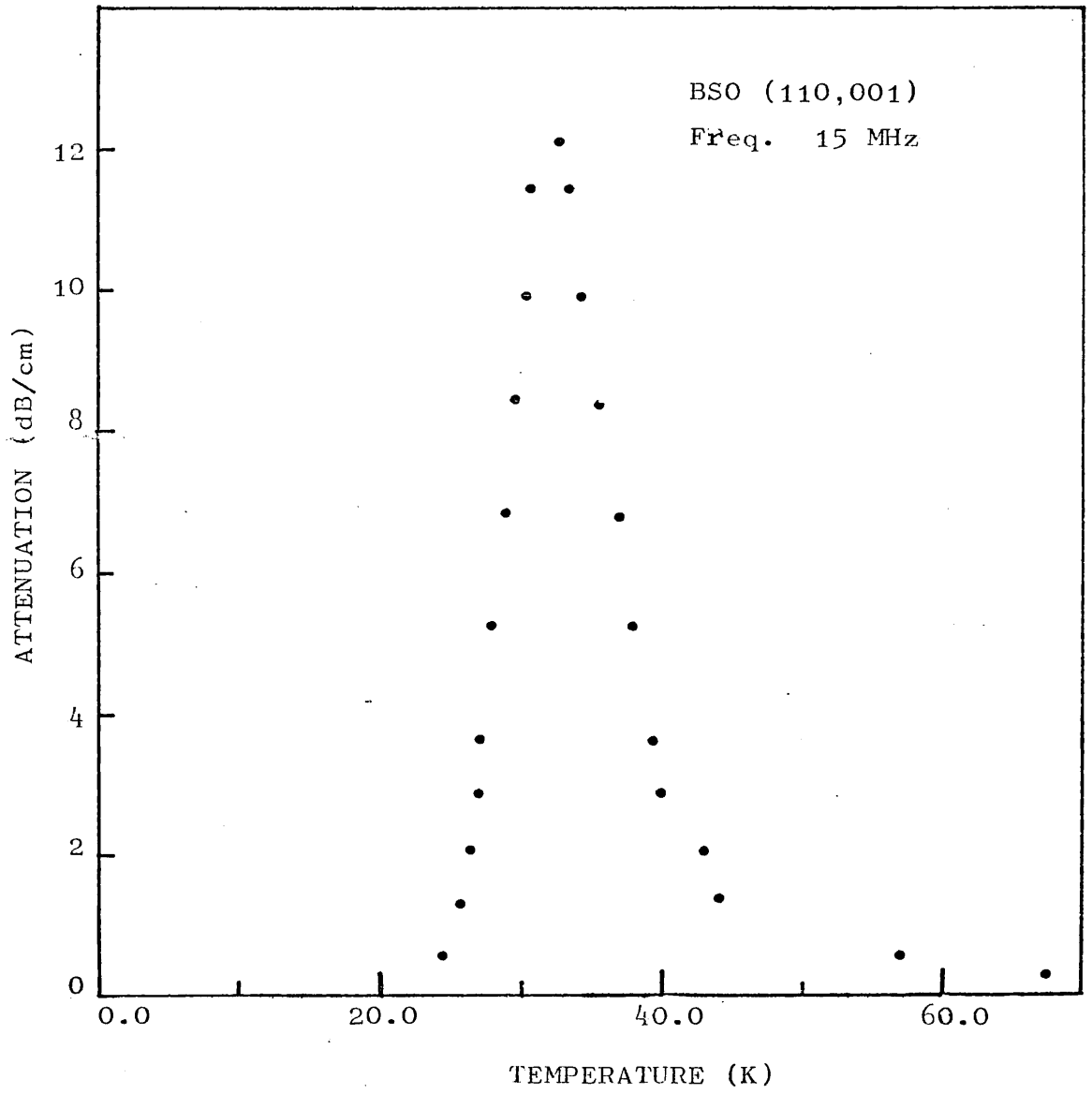

FIG. 2.12 Attenuation as a function of temperature obtained from the raw data given in fig. 2.11

attenuation (dB/cm) was calculated from successive echoes, but no temperature dependence of the coupling was observed. Measurements repeated over a period of more than a year show the reproducibility of the initial calibration. The same procedure was used for all attenuation measurements, throughout this work.
The data plots given in the following Chapters have been plotted by computer using the attenuation values calculated as explained above. The program used for data analysis, to calculate the activation energies and relaxation times has been given in Appendix I.

CHAPTER THREE

RELAXATION ATTENUATION AND MEASUREMENTS IN UNDOPED BGO, BSO

The first part of this chapter deals with the basic theory for anelastic relaxation in crystals, discussed in detail by Nowick, Berry and Heller in their various publications. Various possible relaxation processes are discussed.

In the second section, experimental results of ultrasonic attenuation in undoped BGO and BSO are presented and discussed.

3.1 Relaxation

The term relaxation is used to denote the time-dependent self-adjustment of a system to a new equilibrium condition when an external variable is changed. When the external variable is stress on a crystal it induces an appropriate strain. In a perfectly elastic crystal an alternating stress produces a strain which is in phase and no energy is dissipated. However, when defects are present, the strain will lag behind the applied stress (Zener, 1948), and such a response is called anelastic relaxation. Considering a stress of the form:

$$\sigma = \sigma_o \exp(iwt)$$

the strain can be written as

$$\varepsilon = (\varepsilon_1 - i\varepsilon_2) \exp(iwt)$$

The value of ε/σ immediately upon application of the stress is the elastic compliance s, and the magnitude of the time-dependent change in strain per unit stress $\varepsilon(t)/\sigma$ is known as the relaxation of the compliance δs.

In the case of a suddenly applied static field, the time-dependent behaviour obeys an exponential relaxation, whereas under an a.c. field the components

depend on the frequency, ω, through the Debye equations.

$$\varepsilon_1(\omega)/\sigma_0 = s + \delta s/(1 + \omega^2\tau^2) \qquad (3.1.1)$$

and

$$\varepsilon_2(\omega)/\sigma_0 = \delta s \left[\omega\tau/(1 + \omega^2\tau^2)\right] \qquad (3.1.2)$$

The out-of-phase component of strain, ε_2, gives rise to damping or internal friction in the sample. The two parameters δs and τ are known as the magnitude of relaxation and relaxation time. These equations are analogous to those obtained for the case of dielectric relaxation.

3.1.1 Origin of Anelasticity

The state of a standard anelastic solid can be completely described by some internal variable, which may describe the distribution of a collection of defects or the electronic distribution in the solid. This indicates that anelasticity occurs as a result of the relaxation of internal variables that are coupled to the elastic properties of the crystal. Point defect relaxation or electronic relaxations mainly occur in the case of semiconductors or insulators.

3.1.2 Electronic relaxation

Stress may induce a change in the electronic configuration of a crystal provided that a redistribution of electrons can produce a corresponding strain. For piezoelectric semiconductors, an ultrasonic wave propagating through the crystal is accompanied by a piezoelectric field which acts on the mobile charge carriers. These carriers move toward regions of potential minima in the piezoelectrically induced electric field.

In insulating crystals, electronic relaxation can occur due to the redistribution of bound electrons among two or more equivalent sites.

3.1.3 Point defect relaxation

The presence of defects in a crystal destroys its translational symmetry. The simplest point defects are, a vacancy, an interstitial atom or a single substitutional atom. The defect symmetry is the point group symmetry of the crystal and defect at the site at which the defect is present. The defect symmetry may be lower than or equal to that of the equivalent point in the perfect crystal. If the defect has a

lower symmetry than the perfect crystal, there must exist more than one distinguishable orientation of the defect. In such cases relaxation occurs because of the redistribution of defects among sites which are initially equivalent but become inequivalent in the presence of an external field. The various possible defects in cubic crystals are given in Table 3.1. A defect present in the crystal will interact with a homogeneous stress applied to the crystal, as an electric dipole interacts with an applied electric field. Due to this analogy, Kröner (1958) called such a defect an elastic dipole. The change in strain of a crystal in the presence of defects is given by

$$\varepsilon_{ij}^{(d)} - \varepsilon_{ij}^{0} = \sum_{p=1}^{n_d} \lambda_{ij}^{p} C_p \qquad (3.1.3)$$

ε_{ij}^{d} and ε_{ij}^{0} are the strains with and without defects and p is the index giving one of the possible orientations of the defects. C_p is the mole fraction of defects in orientation p given by

$$C_p = V_0 N_p$$

N_p represents the density of defects in orientation p and V_0 (= $1/N_\mu$, where N_μ is the number of molecules/unit volume) is the molecular volume. Equation 3.1.3 defines a tensor λ_{ij}^{p} which characterizes the elastic

TABLE 3.1 Selection rules for anelastic relaxation

Crystal	Defect	Compliance: Number of distinct relaxation times		Expressions for λ_{ij} in terms of principal values					
		$S_{11}-S_{12}$	S_{44}	λ_{11}	λ_{22}	λ_{33}	λ_{23}	λ_{31}	λ_{12}
Cubic	Tetragonal	1	0	λ_1	λ_2	λ_2	0	0	0
	Trigonal	0	1	λ_a	λ_a	λ_a	$\frac{\lambda_c}{3}$	$\frac{\lambda_c}{3}$	$\frac{\lambda_c}{3}$ *
	Orthorhombic <100>	2	0	λ_1	λ_2	λ_3	0	0	0
	Triclinic	2	3						

* $\lambda_a = (\lambda_1 + 2\lambda_2)/3$

$\lambda_c = (\lambda_1 - \lambda_2)$

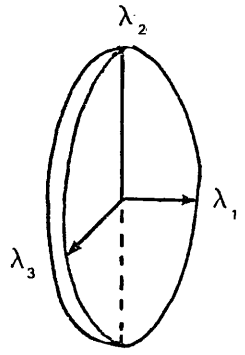

FIG. 3.1 Strain ellipsoid

dipole with components given by

$$\lambda_{ij}^{p} = \frac{\partial \varepsilon_{ij}}{\partial C_{p}}.$$

Therefore λ_{ij}^{p} is the strain per unit mole fraction of defects having the orientation p. Since λ_{ij}^{p} represents a strain tensor, it must by symmetric and therefore can be characterized by a strain ellipsoid with three mutually perpendicular principal axes.

In the coordinate system of the principal axes, the λ tensor becomes

$$\begin{pmatrix} \lambda_1 & 0 & 0 \\ 0 & \lambda_2 & 0 \\ 0 & 0 & \lambda_3 \end{pmatrix}$$

The principal values λ_1, λ_2, λ_3 are independent of the orientation p. The λ_{ij} components can be related to the principal values (Nye 1957) by the equation

$$\lambda_{ij}^{p} = \sum_{m=1}^{3} \alpha_{im}^{p} \alpha_{jm}^{p} \lambda_m \qquad (3.1.4)$$

The index m ranges over the three principal values, α_{im}^{p} is the direction cosine between the fixed axis and the m^{th} principal axis of the dipole, of orientation p. The symmetry of the λ tensor must reflect the symmetry

of the defect it represents. So, the principal axes are limited to lie along the symmetry axes of the defect, and the number of principal values is also sometimes limited. It means that more than one physically distinguishable defect orientation may give the same λ tensor. If all defect orientations have identical response tensors, then relaxation cannot take place. If the number of independent tensors, n_t is greater than one, an arbitrary stress interacts differently with defects having different λ tensors. This gives rise to redistribution of defects and to anelasticity. From this argument Nowick and Berry have derived a general rule called the n_t criterion.

A crystal containing defects will undergo relaxation if n_t is greater than one. The n_t values for various defects in a cubic crystal are given in Table 3.1 In this table, presence of a zero implies the relaxation of that particular compliance does not occur. A number 1, 2 or 3 tells how many distinct relaxation times the designated compliance will manifest.

3.2 Relaxation strength

Nowick and Berry (1972) have derived an expression for the relaxation strength making the following assumptions. All defects may be represented as elastic dipoles with n_t crystallographically equivalent orientation of the λ tensor and the total concentration of defects per formula unit, C_0, cannot change; but dipoles of one ~~interaction~~ orientation can go into another orientation. Since all orientations are crystallographically equivalent, at zero stress C_p the mole fraction of defects having a λ tensor in the orientation p is given by C_0/n_t for all p. Considering a uniaxial homogeneous stress the change in strain is given by

$$\varepsilon_{11} = s_u\sigma + \sum_{p=1}^{n_t} \lambda_{11}^{p}\left[C_p - (C_0/n_t)\right] \qquad (3.2.1)$$

s_u is the unrelaxed compliance for the crystal orientation parallel to the applied stress. The summation term represents the anelastic strain.

Using the differential form of Gibbs function, they have calculated the change produced by a stress σ, in the free energy level, γ_p, for dipole p, to be

$$\frac{\partial \gamma_p}{\partial \sigma} = -V_0 \lambda^{(p)} \qquad (3.2.2)$$

Integrating for small values of the stress

$$\gamma_p = -V_0 \lambda^p \sigma$$

i.e. free energy levels depend only on stress and not on defect concentration, if the concentration is small enough defect interactions do not take place. Once the levels are split, they will be re-populated in accordance with the Boltzmann distribution law. Thus the equilibrium values $\bar{C}_p$ for the concentrations at any given stress and temperature is

$$\frac{\bar{C}_p}{C_0} = \frac{e^{-(\gamma_p/kT)}}{\sum_q e^{-(\gamma_q/kT)}}$$

Expanding the exponentials under the assumption that $\gamma_q/kT \ll 1$ and substituting for γ_p and γ_q gives

$$\bar{C}_p - \frac{C_0}{n_t} \simeq \frac{C_0 V_0 \sigma}{n_t kT} \left[\lambda^p - \frac{1}{n_t} \sum_q \lambda^q \right] \qquad (3.2.3)$$

so deviation of $\bar{C}_p$ from C_0/n_t is proportional to σ and C_0. This redistribution of dipoles is known as stress induced ordering. Substituting Eq. (3.2.3) in to Eq. (3.2.1)

$$\delta s = \frac{\bar{\varepsilon}^{an}}{\sigma} = \frac{C_0 V_0}{n_t kT}\left[\sum_p (\lambda^p)^2 - \frac{1}{n_t}\left(\sum_p \lambda^p\right)^2\right]$$

This relation applies for relaxation under any simple stress. Since there exist several compliances which can undergo relaxation, it is needed to know which of the various compliances undergo relaxation.

Nowick and Heller (1965) have generalised the above expression to calculate the magnitude of relaxation for symmetrized compliances. The relaxation of the symmetrized compliance $\delta s'_\gamma$ has been expressed in the form

$$\delta s_\gamma' = \left(\frac{C_0 V_0}{n_t kT}\right)\lambda_\gamma'^2 \qquad (3.2.4)$$

where λ_γ' is the symmetrized component of the λ tensor for the symmetry designation γ. Expressing the quantity λ_γ' in terms of the components λ_{ij} of the λ tensor, they have obtained the magnitude of relaxation for shear compliances.

For a cubic crystal the magnitudes of relaxation are given by

$$\delta(s_{11} - s_{12}) = \frac{C_0 V_0}{6kT}\left[(\lambda_{11}-\lambda_{22})^2 + (\lambda_{11}-\lambda_{33})^2 + (\lambda_{22}-\lambda_{33})^2\right] \qquad (3.2.5)$$

and

$$\delta s_{44} = \frac{4C_0 V_0}{3kT}\left[\lambda_{23}^2 + \lambda_{31}^2 + \lambda_{12}^2\right] \qquad (3.2.6)$$

These equations are applicable for defects of any allowed symmetry in the cubic crystals. The number of independent values of the λ_{ij} coefficients for various defects, depends on the symmetry of the defect. The λ_{ij} components can be expressed in terms of the principal values as given in Table 3.1. Using Eq. (3.1.4) and substituting in Eq. (3.2.5 and 3.2.6), the magnitude of relaxation for various defect symmetries can be obtained. This helps in finding which compliances relax, when defects of a certain symmetry are present.

Considering a trigonal defect and expressing λ_{ij} in terms of principal values, it can be seen that

$$\frac{2}{3}\delta(s_{11} - s_{12}) = 0 \qquad (3.2.7)$$

and

$$\delta(s_{44}) = \frac{4}{9} \frac{C_0 V_0}{kT} \left|\lambda_1 - \lambda_2\right|^2 \qquad (3.2.8)$$

Similar expressions have been obtained for defects of other symmetries. Table 3.1 gives the possible defect symmetries and the corresponding compliances that undergo relaxation in cubic crystals. It can be seen from Eq. (3.2.8) and other equations obtained by Nowick et al for various defect symmetries, that the magnitude of relaxation due to point defects is proportional to the total defect concentration C_0 and varies inversely as kT. It also varies as the square of some difference in principal values of the λ tensor.

Therefore, if the total defect concentration is known, an anelasticity experiment can provide $|\lambda_1 - \lambda_2|$.

The presence of a collection of randomly oriented defects changes the lattice parameters of a crystal and from this change some parameters of the λ tensor can be obtained. From the definition of the $\lambda_{ij}^{(p)}$ coefficients,

$$\lambda_{ij}^{(p)} = \frac{\partial \varepsilon_{ij}}{\partial C_p}$$

and for a hydrostatic strain per unit concentration of defects

$$\lambda_{11}^{(p)} + \lambda_{22}^{(p)} + \lambda_{33}^{(p)} = 3a^{-1}\left(\frac{da}{dC_0}\right)$$

Since the strain is invariant to the rotation of the axes, therefore

$$3a^{-1}\left(\frac{da}{dC_0}\right) = \lambda_1 + \lambda_2 + \lambda_3$$

This shows that the fractional change in lattice parameter, a, per unit concentration of defects is equal to $\frac{1}{3}(\lambda_1 + \lambda_2 + \lambda_3)$.

This equation provides another relation involving the principal values of λ.

For a trigonal defect, if $\lambda_2 = \lambda_3$, then

$$3a^{-1}\left(\frac{da}{dC_0}\right) = (\lambda_1 + 2\lambda_2) \qquad (3.2.9)$$

For a substitutional atom on a site of cubic symmetry,

$$\lambda_1 = \lambda_2 = \lambda_3 = \lambda$$

and there is no relaxation. From Eq. 3.2.9,

$$\frac{da^*}{dC_0} = \lambda$$

3.2.1 Relation between attenuation, velocity and elastic modulus

For cubic crystals the elastic constants and elastic moduli are related as

$$c_{44} = 1/s_{44}$$

and

$$c_{11} + 2c_{12} = (s_{11} + 2s_{12})^{-1}$$

To obtain an expression for attenuation in terms of s_{ij} and we will consider the (100,001) transverse wave and the (111,111) longitudinal wave.

For the (100,001) transverse wave, the velocity is given by

$$\rho v_s^2 = c_{44}$$

or in terms of elastic modulus s_{44}

$$v_s \ (100,001) = \sqrt{\frac{1}{s_{44}^{o}\rho}}$$

If s_{44} is the modulus that relaxes, let us assume

$$s_{44} = s_{44}^{0} + \delta s_{44}^{*}$$
$$= s_{44}^{0} + \delta s_{44}^{'} - j\delta s_{44}^{''}$$

$$\therefore \quad v = \left[\rho(s^{0}_{44} + \delta s'_{44} - j\delta s''_{44}) \right]^{-\frac{1}{2}}$$

$$= v_s \left[1 - \frac{\delta s^{*}_{44}}{2 s^{0}_{44}} \right]$$

$$= v_s \left[1 - \rho v_s^2 \frac{\delta s^{*}_{44}}{2} \right]$$

$$\frac{1}{v} = \frac{1}{v_s} \left[1 + \frac{\rho v_s^2 \, \delta s^{*}_{44}}{2} \right]$$

Therefore

$$\alpha = \frac{\rho v_s \omega}{2} \delta s''_{44} \qquad \text{(nepers/m)}$$

Using Debye equations as discussed in Section 3.1,

$$\alpha = \frac{\rho v_s}{2} \frac{\omega^2 \tau}{1 + \omega^2 \tau^2} \delta s_{44} \qquad (3.2.10)$$

For the longitudinal (111, 111) mode, the velocity is given by

$$\rho v_L^2 = \frac{1}{3} \left(c_{11} + 2c_{12} \right) + 4/3(c_{44}) + 4/3 \frac{e_{14}^2}{\varepsilon_{11}^s}$$

So, expressing this in terms of compliance constants, the attenuation is given by

$$\alpha_{(111,\ 111)} = \frac{2}{3\rho v_L^3}\ \frac{1}{s_{44}^2}\ \frac{\omega^2\tau}{1+\omega^2\tau^2}\cdot\delta s_{44}$$

$$= \frac{2}{3}\ \rho v_s \left(\frac{v_s}{v_L}\right)^3 \frac{\omega^2\tau}{1+\omega^2\tau^2}\ \delta s_{44} \qquad (3.2.10a)$$

As discussed in Section 3.2, δs_{44} or δs in general is proportional to the total defect concentration C_0 and varies inversely as kT. Therefore the attenuation, α, is given by,

$$\alpha = \beta\frac{\rho v_s}{2}\ \frac{C_0 V_0}{kT}\ (\delta\lambda)^2\ \frac{\omega^2\tau}{1+\omega^2\tau^2} \qquad (3.2.11)$$

Here β is a numerical factor, $\delta\lambda$ the appropriate difference in principal values of the λ tensor and V_0 is the molecular volume. So the attenuation is proportional to the number of defects and inversely to the termperature. We can write

$$\alpha = \frac{A}{T}\ \frac{\omega^2\tau}{1+\omega^2\tau^2} \qquad (3.2.11a)$$

The corresponding change in velocity would be

$$v - v_s = \frac{\rho v_s^3 \, \delta s_{44}^r}{2}$$

$$= \frac{\rho v_s^3}{2} \, \frac{1}{1+\omega^2\tau^2} \, \delta s_{44}$$

3.3 Relaxation processes

A number of relaxation processes have been considered by various workers to explain the change of position of an atom or ion in crystals.

3.3.1 Thermal activation

At a temperature, T, such that kT approaches Q, the height of the potential barrier, the relaxation mechanism is considered to be thermal activation across the barrier (Zener 1952). In this case, the relaxation rate is given by the Arrhenius equation

$$\tau = \tau_{\infty} \exp\left(\frac{Q}{kT}\right) \qquad (3.3.1)$$

where k is the Boltzmann's constant and $1/\tau_{\infty}$, the attempt frequency. $1/\tau_{\infty}$ is a product of a vibration frequency and an entropy factor (Zener 1952). From Eq. (3.3.1) it can be seen that in such a case τ may be varied over a wide range by simply changing the temperature.

From Eq. (3.3.1)

$$\ln \omega\tau = \ln \omega\tau_{\infty} + (Q/k)(1/T) \qquad (3.3.2)$$

Since for the case of a Debye peak, $\ln \omega\tau = 0$ at the peak, therefore

$$\ln \omega\tau_{\infty} + (Q/k)(1/T_M) = 0 \qquad (3.3.3)$$

Here T_M is the temperature at the peak. From a series of peaks obtained at different frequencies, $\ln \omega$ plotted versus $1/T_M$ would give a straight line whose slope is Q/k. This provides the activation energy of the process involved.

But when $kT \ll Q$, the process of thermal activation does not contribute, and to explain the observation of a finite τ a number of other mechanisms have been considered by Sussman (1964, 1967), Pirc, Zeks (1966) and Orbach et al (1961).

3.3.2 Tunnelling process

Sussman has treated the passage of a particle from one potential well to an adjacent one by quantum mechanical tunnelling. Considering a particle moving in a potential well consisting of two adjacent parabolic wells, whenever the two wells are equivalent the particle can be described by symmetric and antisymmetric wave functions. A particle in such a case has equal probability to be in either of the two wells and cannot be considered localized in any of the two wells.

If the potential wells are made inequivalent by random internal strain or external applied fields, the wave functions are in general assymetric and localize the particle. Phonons can induce transitions from the localized state in one well to the localized state in the other well. Three types of transition processes have been discussed.

(a) One Phonon Process

This process also known as the direct process, involves the emission or absorption of a single phonon. Sussman (1964) considers this relaxation mechanism to be tunneling accompanied by simultaneous emission or absorption of a phonon, but Pirc et al (1966) considered the successive processes of tunnelling and the phonon

emission or absorption. Using first order perturbation theory, the relaxation time is given by

$$\tau \sim T^{-1}$$

(b) Raman Process

The single phonon process dominates only at the lowest temperatures (below 20 K). At slightly higher temperatures, the second order processes, involving virtual intermediate states may occur. In this case, the relaxation time for temperatures below the Debye temperature has been calculated to be

$$\tau \sim T^{-7}; \qquad T \ll \theta_D$$

For temperatures above the Debye temperature,

$$\tau \sim T^{-2}; \qquad T > \theta_D$$

(c) Indirect Process

The third type of transition is considered to be multiphonon or an indirect process involving intermediate states. The relaxation time is given by

$$\frac{1}{\tau} \sim \sum_i [1 \; / \; \exp(\Delta_i/kT) - 1]$$

Δ_i is the energy difference between the initial and intermediate states. When $\Delta_i \gg kT$, the expression 3.2.2 reduces to rate equation. Similar processes are discussed by Van Vleck (1967) and Scott and Jeffries (1962) for the case of spin lattice relaxations. When all three processes are present the relaxation time τ is given by

$$\frac{1}{\tau} = AT + CT^7 + \sum_i \frac{B_i}{\exp(\Delta_i/kT) - 1}$$

Experimental measurements can yield τ as a function of temperature which provides evidence for the relaxation process involved. From the measured relaxation times and a model of defects in the crystal, the jump rates of an atom or ion that change position in the process of reorientation of the defect may be determined.

3.4 Experimental results

The attenuation measurements were made on the undoped, doped, irradiated and annealed samples of BGO and BSO. Results for undoped crystals only are discussed in this chapter. The attenuation was measured for various modes as a function of temperature, T, and frequency, ω.

3.4.1 Data for BGO

Three samples were prepared as described in Section 2.4 with <100>, <111> and <110> orientation from the same boule of BGO. Two transverse (110, 001), (100, 001) and two longitudinal (100, 100) and (111, 111) modes were studied. The data was obtained at three frequencies over the temperature range from 4.2 to 260 K using the method described in Chapter Two. Each set of results was obtained by carrying out a number of warming and cooling runs. From the raw data (plots from the XY recorder), as shown in Section 3.7, the relative attenuation was calculated taking the attenuation value at 4.2 K as a reference zero value.

FIG. 3.2 shows the attenuation as a function of temperature for the transverse (110, 001) mode at 15, 25 and

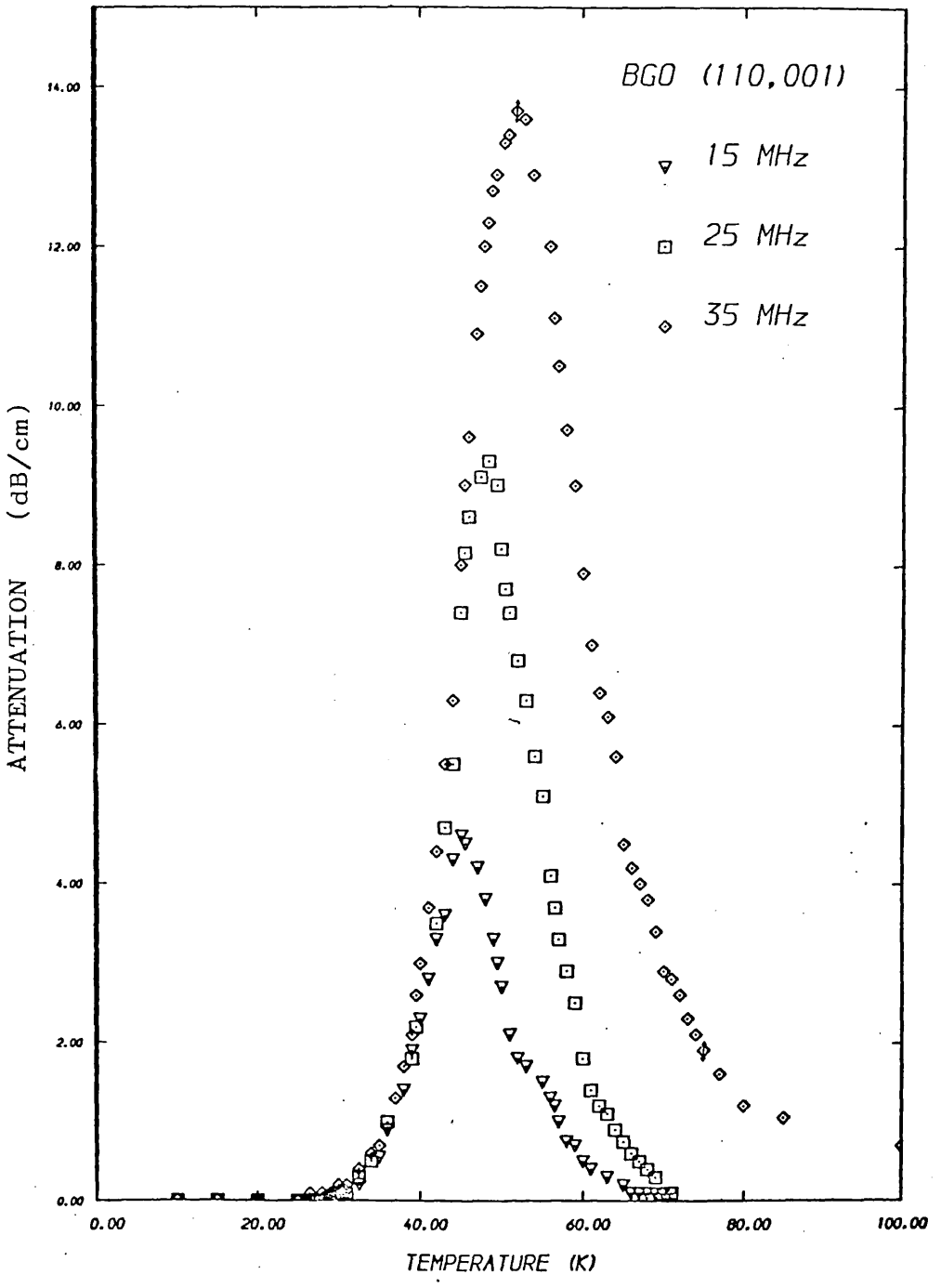

FIG. 3.2 Attenuation of T(110, 001) mode as a function of temperature and frequency

35 MHz. A large attenuation peak was observed between 35 and 60 K. As can be seen from Fig. 3.2, the peaks shifted to higher temperatures as frequency was increased.

FIG. 3.3 shows the results for transverse (100, 001) and longitudinal (100, 100) modes. Transverse (100, 001) mode showed a similar attenuation peak, with larger amplitude, but no peak was seen for the (100, 100) longitudinal mode. A similar, but much smaller peak was seen for the longitudinal (111, 111) mode as in Fig. 3.4. These results show that ultrasonic waves are attenuated selectively in this temperature range.

3.4.2 Data for BSO

For $Bi_{12}SiO_{20}$, only the transverse (100, 001) mode was studied, using a cylind rical rod sample. The attenuation peaks were found to be at slightly lower temperatures (30 - 50 K) and larger in amplitude compared with those for transverse (110, 001) mode in BGO.

For BSO, a smaller peak at 150 K was also observed. The height of this second peak also increased with increasing frequency, but the shift in position was

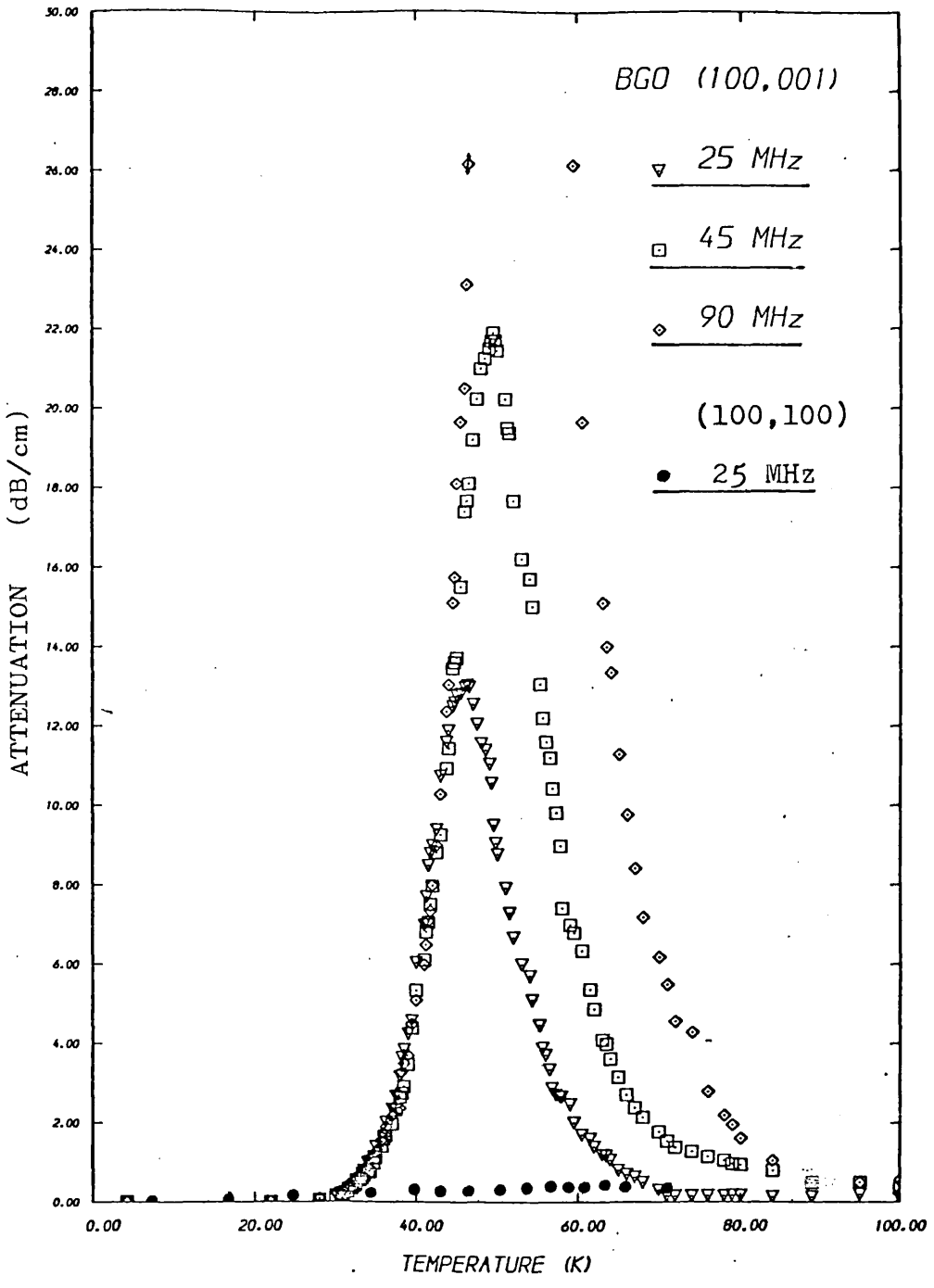

FIG. 3.3 Temperature and frequency dependence of attenuation for the transverse (100, 001) and longitudinal (100, 100) mode

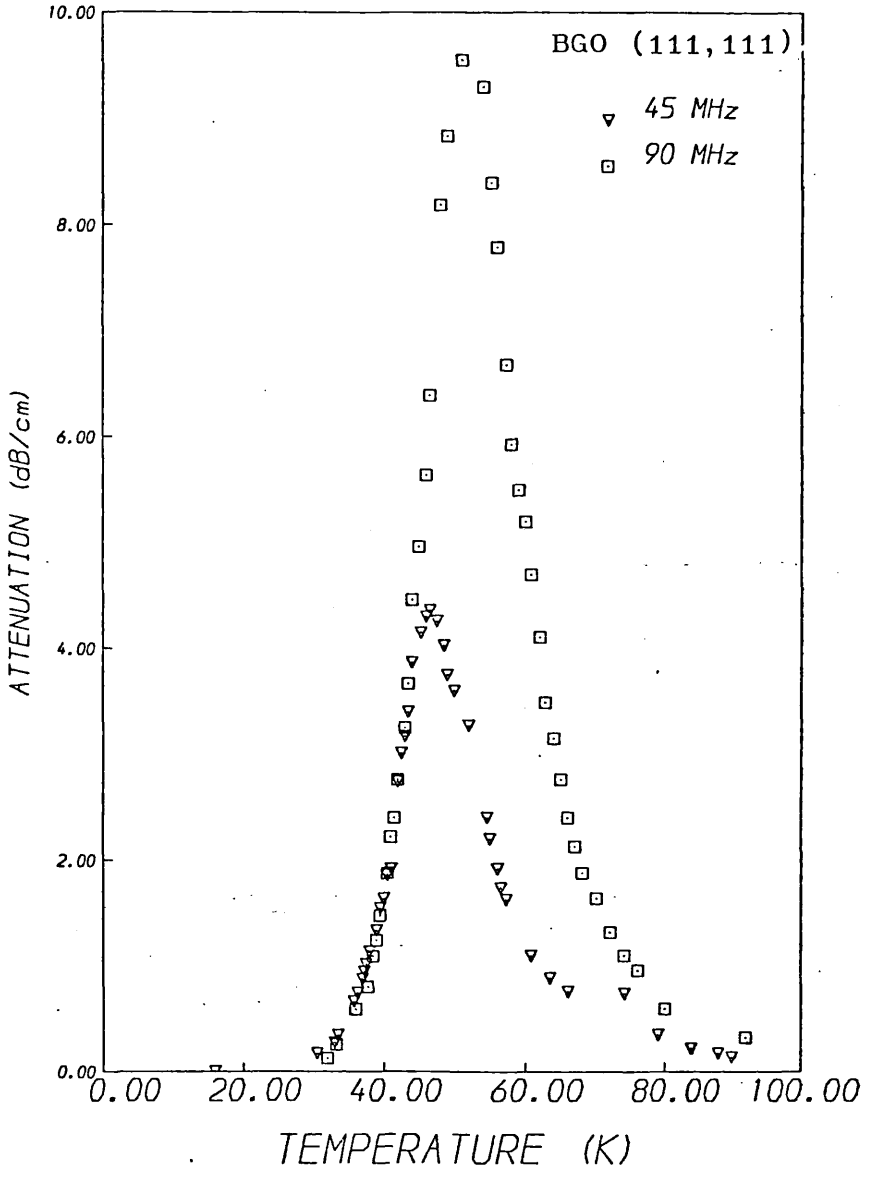

FIG. 3.4 Attenuation of L(111,111) mode

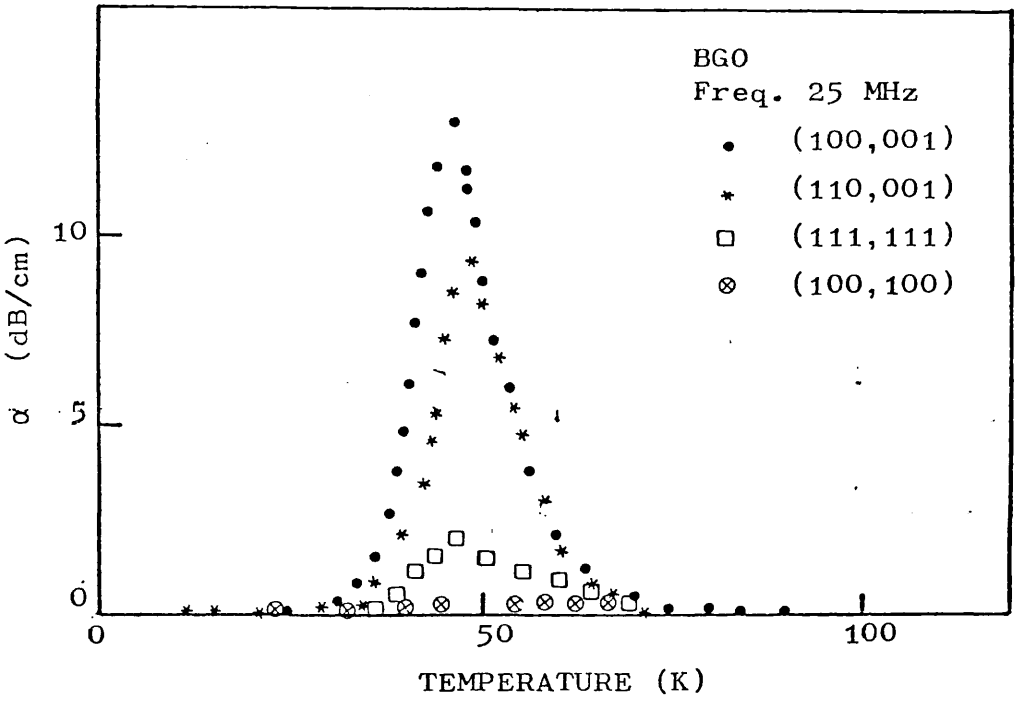

FIG. 3.5 Attenuation as a function of temperature for all modes studied for BGO

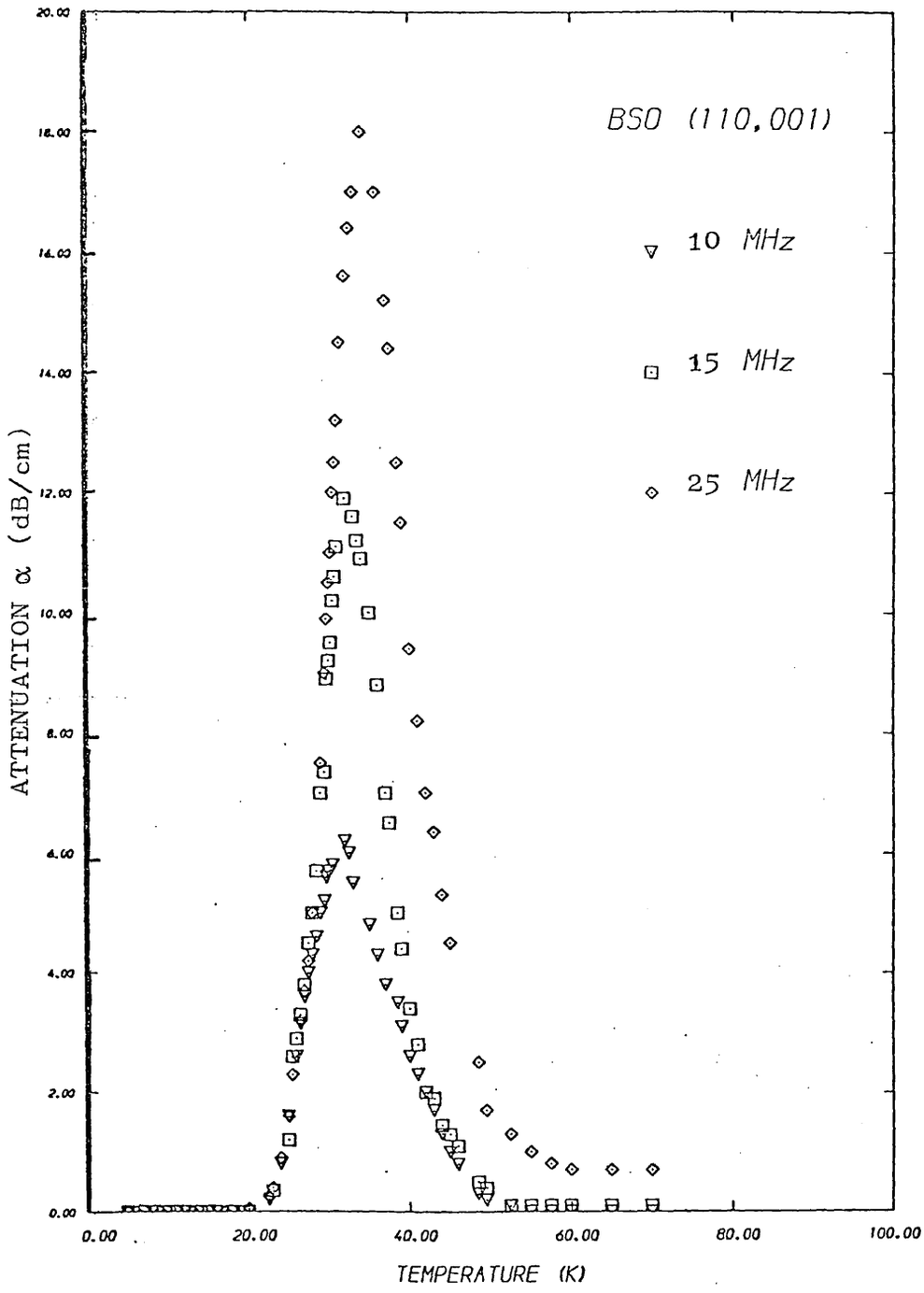

FIG. 3.6 Attenuation of T(110, 001) mode in BSO as a function of temperature and frequency

negligible. But for BGO no corresponding peaks were observed up to 250 K. Fig. 3.5 shows the attenuation as a function of temperature for all modes for the complete temperature range from 4.2 to 120 K.

The peak attenuation was unchanged by changing the input acoustic power by 20 dB. Attenuation could be measured to within $\pm$ .1 dB. Table 3.2 gives the peak attenuation values α_M and the corresponding peak temperatures, T_M, for various frequencies.

TABLE 3.2 Peak attenuation and peak temperatures for various modes and frequencies

Sample	Orientation	Mode	Frequency MHz	α_M (dB/cm) $\pm.1$	T_M (K)
BGO	110	T_1	15	4.6	44.6
			25	9.3	47.8
			35	13.7	51.5
"	100	T	25	13.04	46.25
			45	21.9	49.5
			90		52.5
"	100	L	25	-	-
			45	-	-
"	111	L	45	4.36	46.5
			90	9.55	51.0
BSO	110	T	10	6.2	31.5
			15	11.9	32.25
			25	17.0	34

3.5 Analysis of the experimental results

3.5.1 Shape of the attenuation peaks

The attenuation peaks show the usual features of a relaxation phenomenon.

(i) The peaks shift to higher temperatures with increasing frequency as shown in Fig. 3.7.

(ii) The peak amplitude increases with frequency ω.

(iii) On the higher temperature side of the peak, the attenuation varies with frequency as $\sim \omega^2$.

(iv) Curves for all frequencies overlap on the low temperature side of the peak.

3.5.2 Relaxation time

The next problem was to characterize the unknown relaxation time spectrum from the experimental attenuation curves. Various relaxation processes are possible as discussed in the previous sections, and the relaxation time spectrum may be composed of a set of relaxation times or it may be a continuous spectrum characterized by a particular distribution function.

From the attenuation curves obtained at different frequencies, ω, log ω was plotted versus $1/T_M$ as in Fig.3.7. A straight line plot was obtained for both BGO and BSO. Since for a relaxation peak, $\omega\tau = 1$ at the peak temperature, so the straight line plot suggests that the relaxation time, τ, obeys an Arhenius relation given by

$$\tau = \tau_\infty \, e^{Q/kT}$$

From Eq. (3.3.2),

$$\ln \omega\tau = \ln \omega\tau_\infty + \theta\left(\frac{1}{T}\right) \qquad \text{where } \theta = Q/k \qquad (3.5.1)$$

Since at the peak temperature T_M $\omega\tau$ equals unity and $\ln \omega\tau = 0$, therefore

$$\ln \omega\tau + \theta(1/T_M) = 0$$

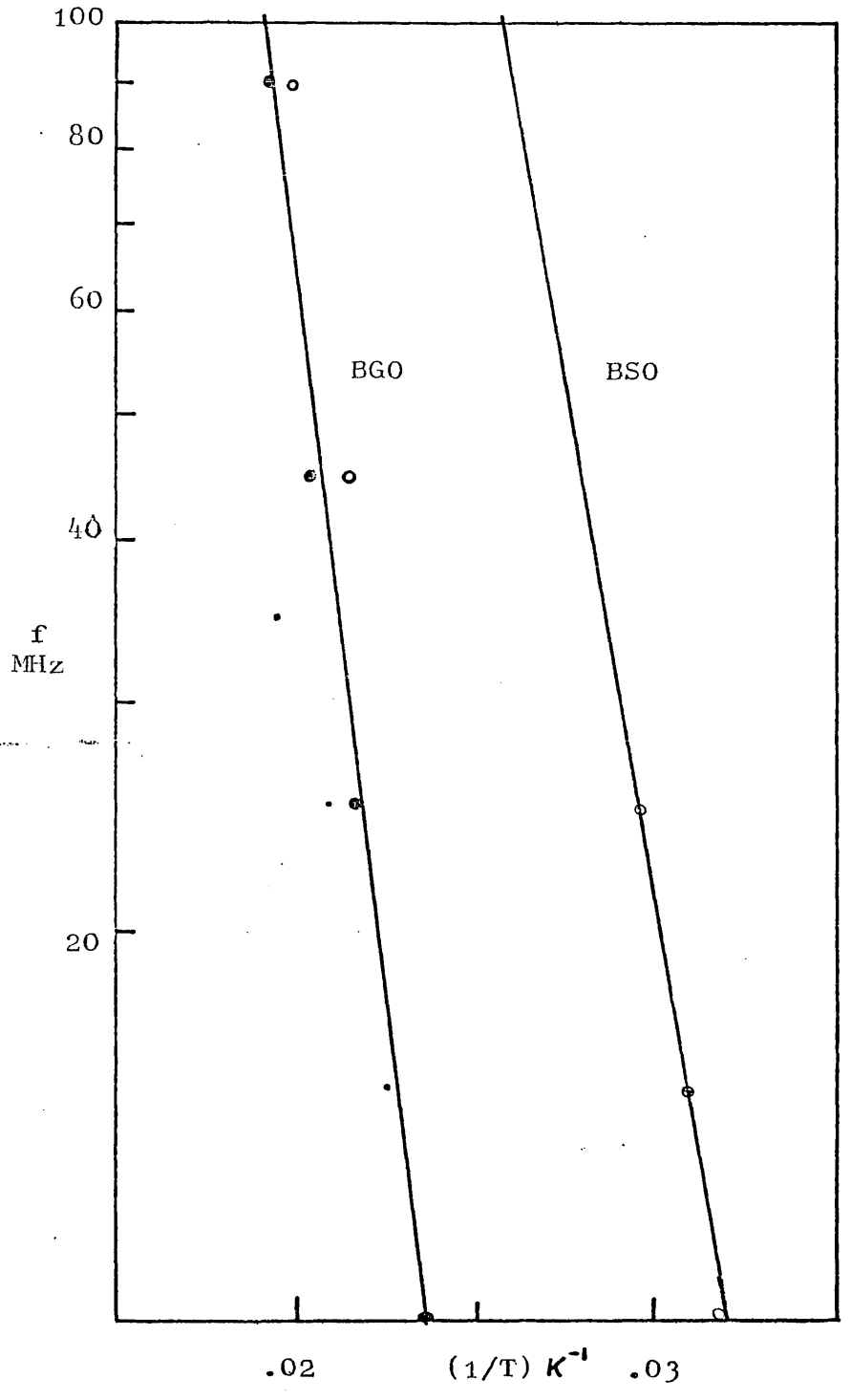

FIG. 3.7 Logarithm of the frequency versus reciprocal of peak temperature for BSO and BGO

and the slope of the straight line plot obtained above (Fig. 3.7) gives θ and hence the activation energy of the process involved.

The slopes of the two straight lines give

Crystal	θ K	Q eV
BGO	511	0.044
BSO	367	0.031

since a small range of frequencies was covered, this method gives approximate value of the activation energy.

A precise way of calculating the activation energy described by Nowick and Heller was used. If the normalized dynamic response function of a standard anelastic solid is plotted versus 1/T, equivalent values of the response function taken at different frequencies correspond to the same value of $\omega\tau$. If $1/T_1$ and $1/T_2$ are the values corresponding to a certain value of the response functions at frequencies ω_1 and ω_2, then from Eq. (3.5.1)

$$\ln\left(\frac{\omega_2}{\omega_1}\right) = \theta\left(T_1^{-1} - T_2^{-1}\right) \qquad (3.5.2)$$

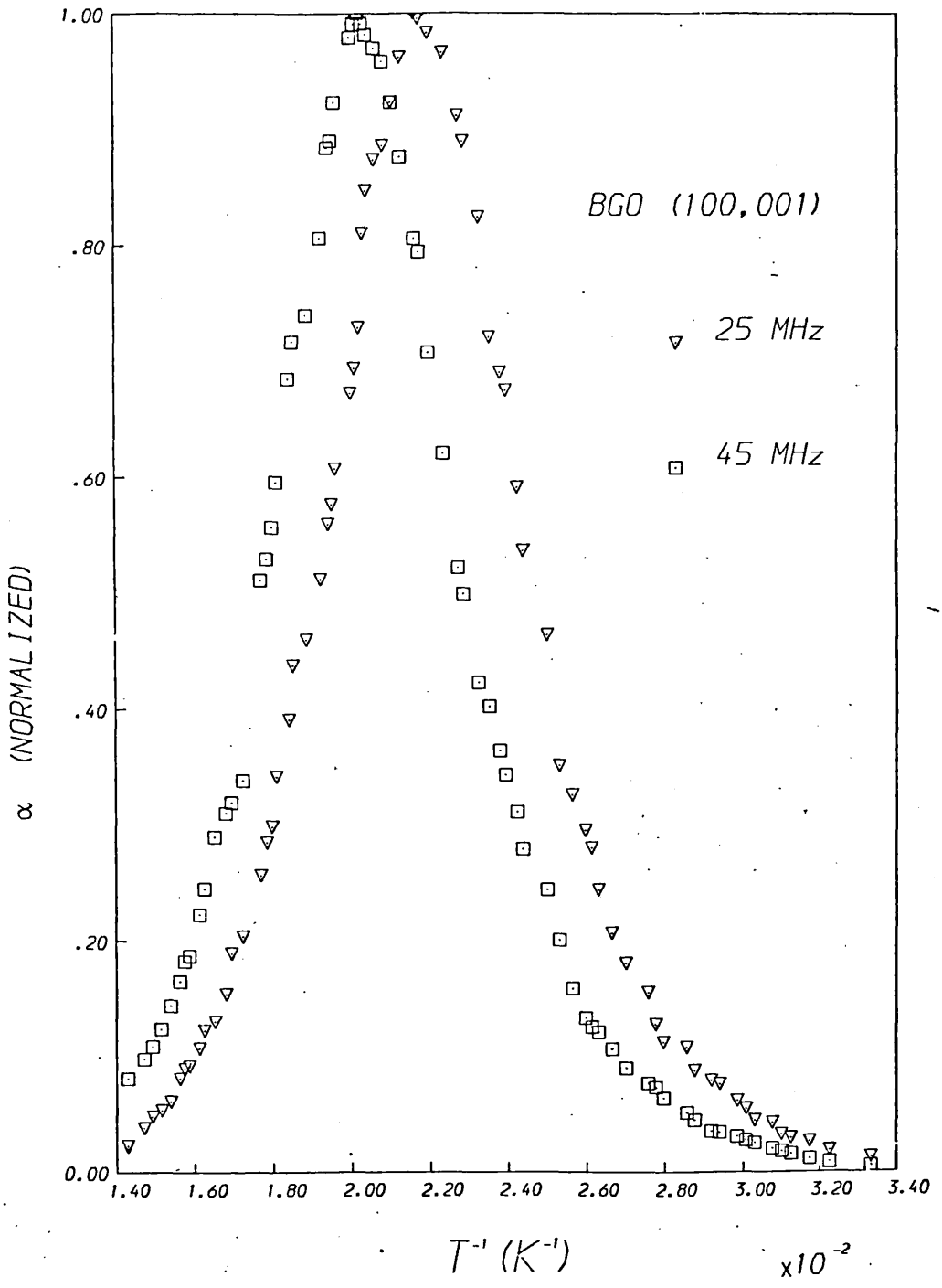

FIG. 3.8 Normalized attenuation for the transverse (100, 001) mode versus 1/T

This equation should be satisfied at all points on the curve.

If θ, i.e. the activation energy is constant, curves for two frequencies should be displaced by a constant shift δT^{-1} along the 1/T axis, which is equal to $1/\theta(\ln \omega_2/\omega_1)$. From the shift δT^{-1}, θ can be calculated.

Fig. 3.8 shows a plot of normalized attenuation versus 1/T for the transverse (100, 010) mode at 25 and 45 MHz. From the shift δT^{-1} at a number of points; the value of activation energy, calculated by using Eq. (3.5.2) is tabulated below.

S. No.	θ K	Q eV
1	485.7	0.042
2	413.9	0.036
3	477.8	0.041
4	416.8	0.036
5	425.9	0.037
6	445.0	0.038
7	413.9	0.036

This gives the average activation energy to be 0.038 $\pm$ .002 eV.

Using Eq. (3.5.1), the width of the Debye peak versus 1/T is given by

$$\Delta(T^{-1}) = (1.144)(2.303/\theta)$$

Therefore the peak width is inversely proportional to the activation energy, if the peak is truly a Debye peak.

From Fig. 3.8, using the peak width at half maximum,

Frequency MHz	Width at half maximum $\Delta(T^{-1})$	θ K	C eV
25	5.2×10^{-3}	504.8	.043
45	5.4×10^{-3}	480.8	.041

This gives average activation energy to be 0.042 $\pm$ .001 eV, which agrees quite well with the values obtained above. This shows that attenuation peaks are single Debye peaks.

3.5.3 Least square fittings

The relaxation time as a function of temperature was calculated by computer fittings.

As derived in Section 3.2.1, the relaxation attenuation is given by

$$\alpha = \frac{A}{T} \frac{\omega^2 \tau}{1+\omega^2 \tau^2} \qquad (3.5.4)$$

where A is a constant depending on the number of defects and the relaxation strength. The relaxation time τ obeys the Arhenius relation.

From the experimental value of attenuation α, at peak temperature for a certain mode and frequency A was calculated. Using least square fitting methods, by varying τ_∞ and 0, the relaxation time $\tau(T)$ was obtained for temperatures, T, from 20 K to 80 K. Plots for ln (τ) versus 1/T are shown in Fig. 3.9, 3.10, 3.11. The computed values of activation energy attempt frequency $1/\tau_\infty$ and A's are given in Table 3.3.

An example of a fit produced using A = 34.8 dBK/cm/MHz and $1/\tau_\infty = 4.6 \times 10^{12}$Hz for the transverse (100, 001) mode is shown in Fig. 3.12.

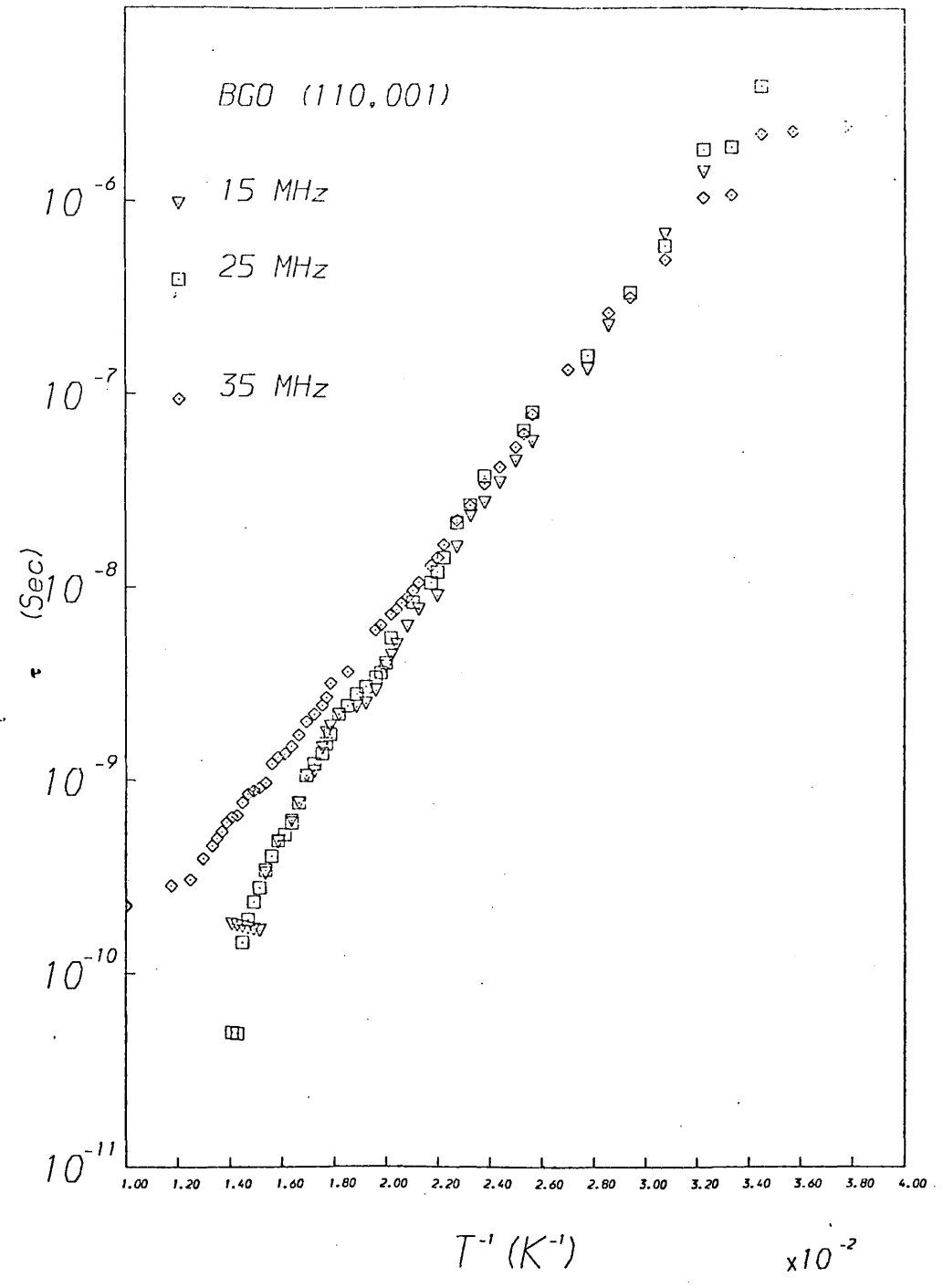

FIG. 3.9 Logarithm of the relaxation time versus reciprocal temperature at different frequencies for the transverse wave (110, 001) in BGO

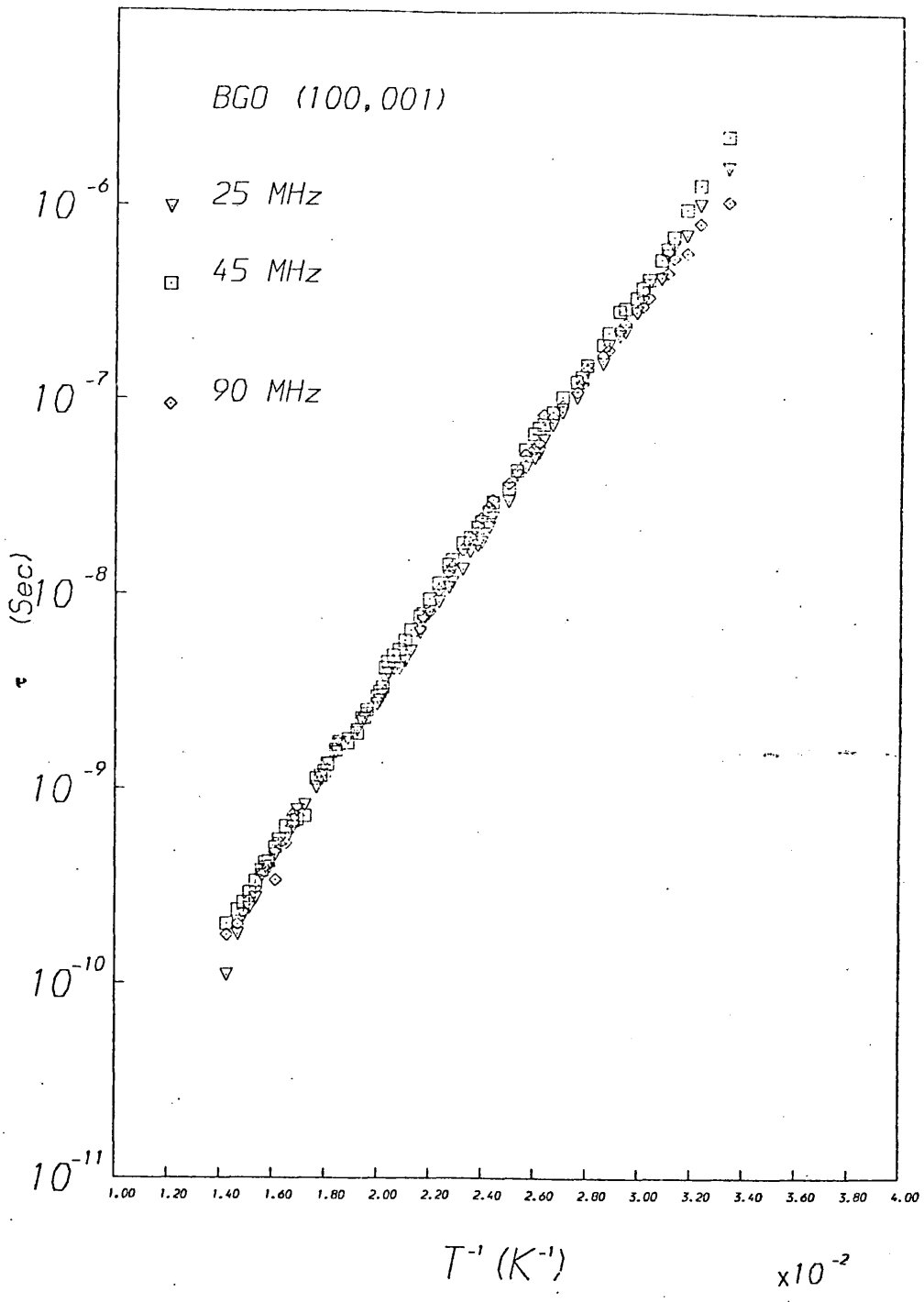

FIG. 3.10 Logarithm of the relaxation time versus reciprocal temperature for the transverse (100, 001) mode in BGO

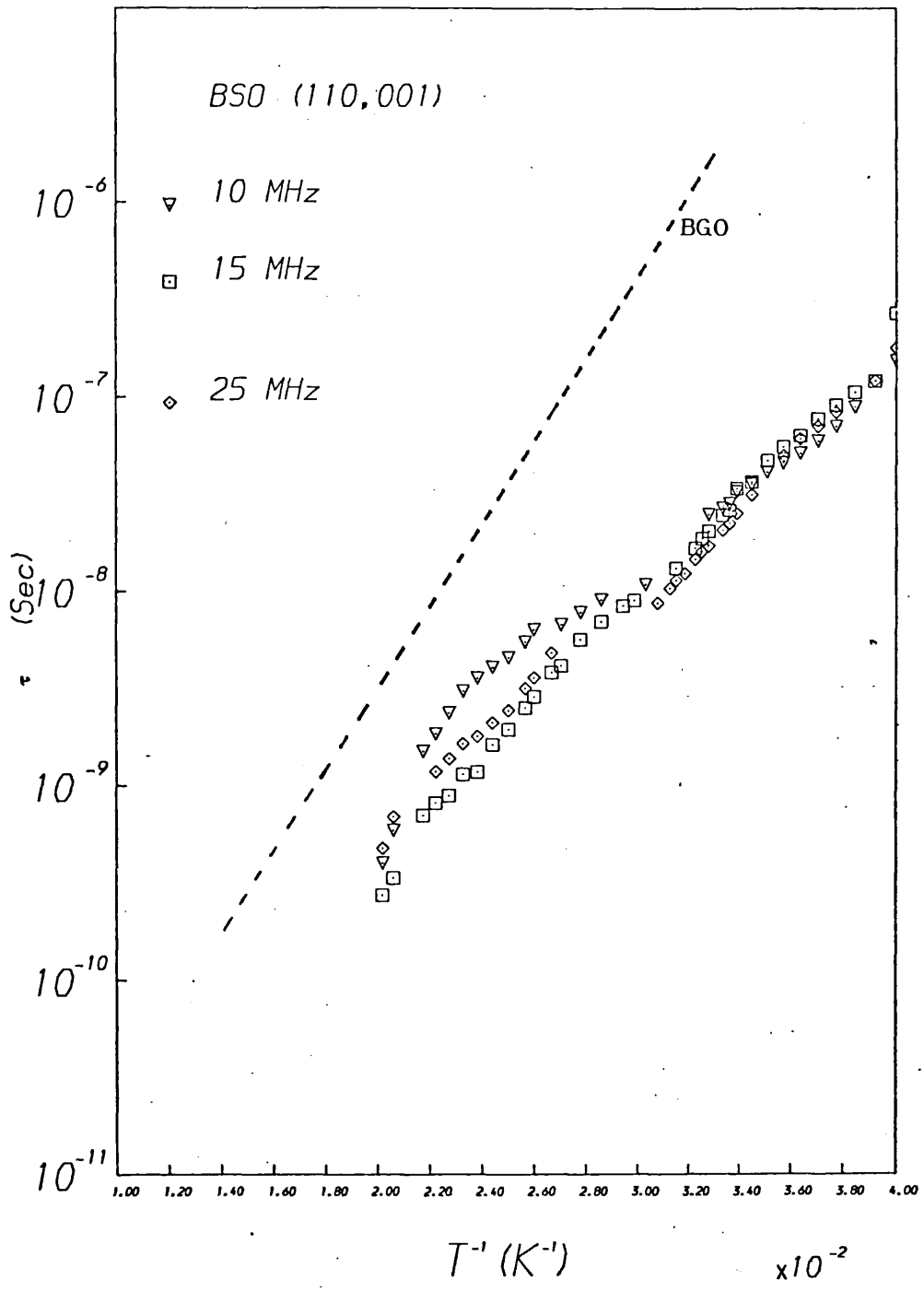

FIG. 3.11 Logarithm of the relaxation time versus reciprocal temperature for the transverse (110, 001) mode in BSO

TABLE 3.3 Values of activation energy, attempt frequency and A for different modes

Crystal	Mode	Frequency	$A = \frac{\alpha_M T_M}{f}$ dB K/cm MHZ	θ K	Q eV	$1/\tau_\infty$ 10^{12} Hz
BGO	(110,001)	15	27.6	499±9	.043±.001	5±1
		25	36.0	508±12	.044±.001	6±1
	(100,001)	25	48.25	481±5	.042±.001	5±.5
		45	46.19	474±3	.041±.0004	3±.2
		90	48.0	484±4	.042±.004	6±.5
BSO	(110,001)	10	39.0	271±10	.024±.001	.3±.1
		15	50.7	330±7	.028±.0005	2±.5
		25	44.8	278±6	.025±.0005	.5±.1

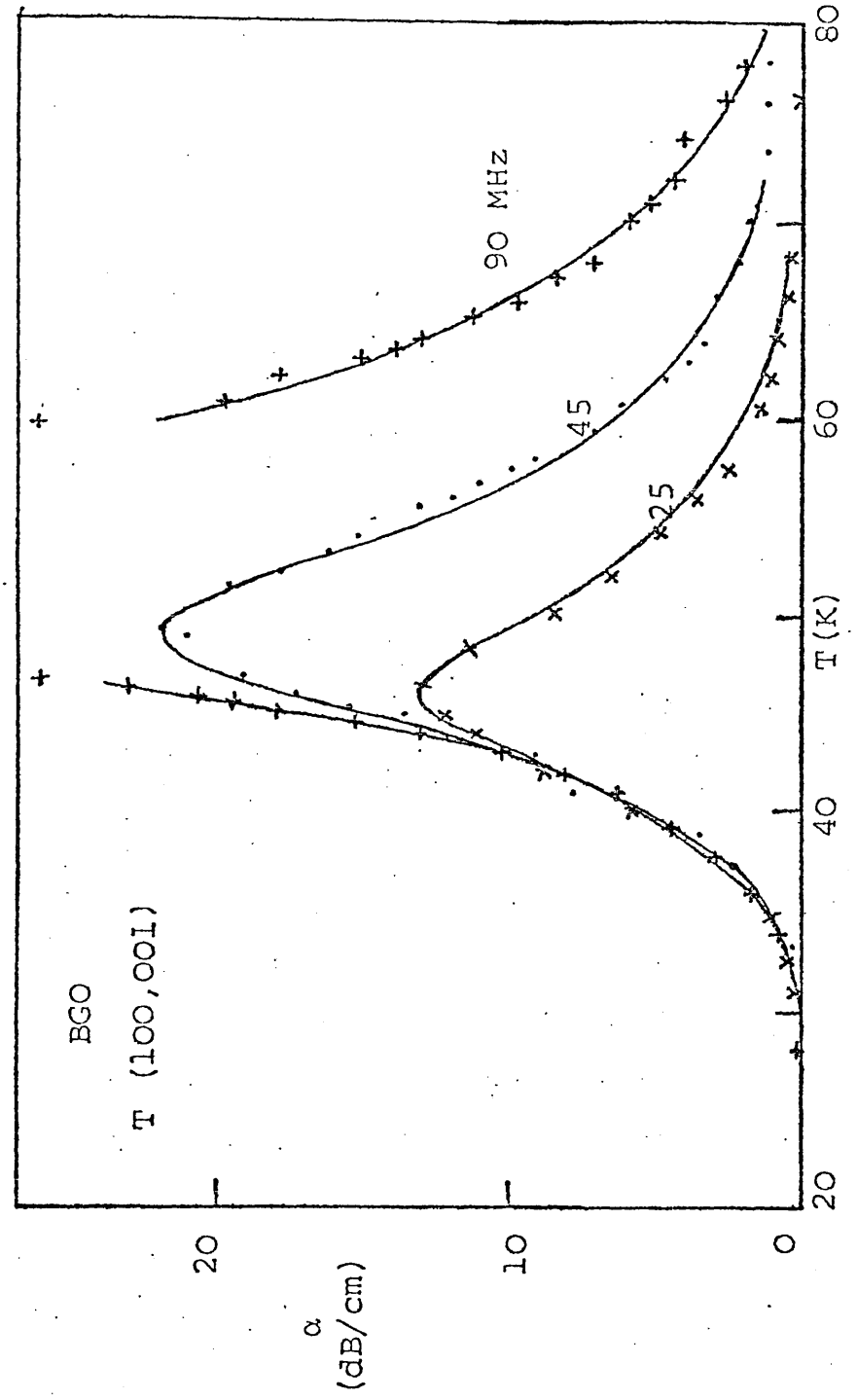

FIG. 3.12 Attenuation of T(100, 001) mode in undoped BGO fitted to Eq. (3.5.4) with A = 34.8 dBK/cm MHz

3.5.4 Relaxation strength

The strength of relaxation for various modes is calculated as follows:

In general the strain is not in phase with the stress as discussed in Section 3.1, if relaxation effects are present, but lags behind the stress by an angle ϕ.

When a sinusoidal stress is applied to standard anelastic solids, the phase angle ϕ is given by:-

$$\tan \phi = \frac{\Delta}{(1+\Delta)^{\frac{1}{2}}} \frac{\omega\tau}{1+\omega^2\tau^2} \qquad (3.5.5)$$

Δ is called the relaxation strength and given by

$$\Delta = \frac{\delta s}{s_u}$$

s_u is the unrelaxed compliance for the particular mode

The attenuation of an ultrasonic wave of frequency ω travelling through a crystal with velocity v, is related to the phase angle ϕ by

$$\tan \phi = \frac{2v\alpha}{\omega} \qquad (3.5.6)$$

From Eq. (3.5.5) and (3.5.6) and the experimental value of attenuation, the relaxation strengths for various modes were calculated and are given by Table 3.4. This shows that the strength of relaxation depends on the mode.

The relaxation strength Δ is much less than one, for all modes. Nowick and Heller have derived that if $\Delta < 0.01$ there is no interaction between the defects.

3.5.5 Discussion

(a) As can be seen from the experimental results the transverse (100, 001), (110, 001) and the longitudinal (111, 111) modes show similar attenuation peaks. But no peak was observed for the longitudinal (100, 100) mode.

The strength of relaxation as given in Table 3.4 depends on the mode. The experimental results for various modes studied for BGO and BSO are summarized along with the effective elastic constants in Table 3.5.

This table shows that the low temperature attenuation peak is shown only by those modes whose velocity depends on the s_{44} compliance constant.

TABLE 3.4 Relaxation strength for different modes calculated from experimental results

Crystal	Mode	Velocity 10^5 cm/sec	Frequency MHz	Relaxation Strength, Δ $10^{-3} \pm 2 \times 10^{-4}$
BGO	(100,001)T	1.646	25 45	6.3 5.8
	(110,001)T	1.70	25 35	4.6 4.8
	(111,111)L	3.332	45 90	2.0 2.3
	(100,100)L	3.33		$< 10^{-5}$
BSO	(110,001)T	1.70*	10 15 25	3.8 4.9 4.2

* Hardy (1976).

TABLE 3.5 Effective, elastic and compliance constants for various modes

Crystal	Orientation	Mode	Effective Elastic constant	Effective Compliance constant	Attenuation Peak
BGO	(100)	T	c_{44}	s_{44}^{-1}	Yes
	(100)	L	$\frac{1}{3}(c_{11}+2c_{12}) + \frac{2}{3}(c_{11}-c_{12})$	$\frac{1}{3}(s_{11}+2s_{12})^{-1} + \frac{2}{3}(s_{11}-s_{12})^{-1}$	No
	(110)	T_1	$c_{44} + \frac{e_{14}^2}{\varepsilon_{11}^s}$	s_{44}^{-1}	Yes
	(111)	L	$\frac{1}{3}(c_{11}+2c_{12})+\frac{4}{3}c_{44}+\frac{4}{3}\frac{e_{14}^2}{\varepsilon_{11}^s}$	$\frac{1}{3}(s_{11}+2s_{12})^{-1} + \frac{4}{3}(s_{44})^{-1}$	Yes
BSO	(110)	T	$c_{44} + \frac{e_{14}^2}{\varepsilon_{11}^s}$	s_{44}^{-1}	Yes

Similar results were obtained by Rehwald (1973). From Table 3.5, the velocity for two transverse (100, 001) and (110,001) modes is given by

$$\rho v_s^2 \ (100,\ 001) = c_{44}$$

and

$$\rho v_s^2 \ (110,\ 001) = c_{44} + \frac{e_{14}^2}{\varepsilon_{11}^s}$$

Both modes show similar attenuation peaks, therefore contribution from dielectic loss through piezoelectric coupling must be a small fraction.

If s_{44} is the elastic compliance that undergoes relaxation, then as derived in Section 3.2.1, the attenuation can be written as

$$\alpha_{(100,001)} = \frac{\rho v_s}{2} \ \frac{\omega^2\tau^2}{1+\omega^2\tau^2} \ \delta s_{44}$$

page 92

From Table 3.2, using α_M the peak attenuation, δs_{44} can be calculated for both transverse modes.

Similarly δs_{44} can be calculated for the longitudinal (111, 111) mode using Eq. (3.2.10a). The calculated values for δs_{44} are tabulated below.

Crystal	Mode	Frequency MHz	δs_{44} * 10^{-13} m^2/N
BGO	(100,001)T	25	2.3 $\pm 2 \times 10^{-15}$
		45	2.2
	(110,001)T_2	25	1.6
		35	1.8
	(111,111)L	25	2.
		45	2.0
		90	2.6
BSO	(110,001)T_2	10	1.8
		25	2.1

* Normalized at 50 K

As can be seen from Table 3.5, the transverse (110, 001) and (100, 001) modes have s_{44} as the effective compliance constant, while the longitudinal (111, 111) involves both $(s_{11} + 2s_{12})$ and s_{44}; but the values of δs_{44} for all three modes are the same within an order of magnitude. Further, the longitudinal (100, 100) mode which has $(s_{11} - s_{12})$ and $(s_{11} + 2s_{12})$ as the effective compliances shows no attenuation peak. This confirms that s_{44} is the only compliance that undergoes relaxation.

(b) Defect symmetry .

As shown by Nowick et al, for cubic crystals the compliance $(s_{11} + 2s_{12})$ does not undergo relaxation, therefore only $(s_{11} - s_{12})$ and s_{44} have to be considered. The selection rules given in Table 3.1 show that for a tetragonal defect only $(s_{11} - s_{12})$ relaxes and for a triclinic defect both $(s_{11} - 2_{12})$ and s_{44} relax. But for a trigonal defect only s_{44} relaxes.

Therefore, the defect responsible for the attenuation peaks observed in BGO, BSO must have a trigonal symmetry.

(c) Defect concentration

As derived in Section 3.2.1, when a trigonal defect is the cause of relaxation attenuation, the attenuation can be given by

$$\alpha(\text{nepers/m}) = \frac{2}{9}\rho v_s \frac{C_0 V_0}{kT} |\lambda_1 - \lambda_2|^2 \frac{\omega^2\tau}{1+\omega^2\tau^2}$$

$$= \frac{2}{9} \frac{C_0 v_s M}{kT} |\lambda_1 - \lambda_2|^2 \frac{\omega^2\tau}{1+\omega^2\tau^2} \qquad (3.5.5)$$

Here M is the molecular weight.

Using the experimental values of peak attenuation, the product of defect concentrations C_0 and square of the difference $|\lambda_1 - \lambda_2|$ can be calculated. The values of $C_0 |\lambda_1 - \lambda_2|^2$ for the samples used in this work are given below.

Crystal	Mode	Frequency MHz	$C_0 \lvert\lambda_1 - \lambda_2\rvert^2$ 10^{-7}
BGO	(110,001)T	15	3.8
		25	4.63
		35	5.6
	(100,001)T	25	6.7
		45	6.7
	(111,111)L	45	5.1
		90	6.1
BSO	$(110,001)T_2$	15	7.1
		25	6.4

From this product, $|\lambda_1 - \lambda_2|^2$ can be estimated if the number of defects is known or if $|\lambda_1 - \lambda_2|$ is known from some other measurements then the defect concentration can be calculated.

(d) As seen in Section 3.5.3, the attenuation peaks are simple Debye peaks with a single relaxation time. The plots of τ versus 1/T show that the process is the thermal activation of an atom or defect from one site to another. The values of activation energies given in Table 3.3 suggest that the same relaxation process is responsible for all modes in BGO. But comparing the attenuation curves for BGO and BSO, slight differences are noticed. For BSO, the attenuation peaks were observed at lower temperatures and the activation energy is much smaller (0.028 eV) for BSO than that for BGO (0.04 eV). Since only one atom in 33 has been changed, it suggests the involvement of Ge or Si sites.

The site symmetries of different atoms given in Table 1.4 also shows that the defect must be associated with the oxygen atoms in the GeO_4 or SiO_4 tetrahedron which lie at the cubic 23 sites.

The various possible defects are discussed in Chapter Six.

CHAPTER FOUR

ATTENUATION MEASUREMENTS IN DOPED, ANNEALED BGO AND γ-IRRADIATED BSO

In the first part of this chapter, measurements of attenuation in doped single crystals of BGO are presented and discussed. In the later sections, effects of annealing and γ-irradiation are discussed.

Effects of some dopants on the acoustic and optical properties of BSO have previously been studied by Rehwald (1976) and Hou et al (1973). Recently Obserchmid and Grabmaier have studied the effects of many dopants on the optical absorption in BGO

Since it has been suggested by various workers that there is a correlation between the optical absorption below the band gap and the ultrasonic attenuation peaks, the aim of this work was to try and establish the possible absorption centre by studying the doped BGO crystals in detail.

4.1 Doped BGO samples

The doped BGO samples were kindly provided by Dr Grabmeier and Oberschmid. Due to the small size of crystals available, samples were prepared with only <110> orientation as described in Section 2.4. Measurements were made using the same method as for the undoped samples at a number of frequencies.

Table 4.1 gives the samples studied along with their colours, dopant concentration and other properties measured by Oberschmid (1978). The dopant concentration was found by chemical analysis. As can be seen from the table, the colour of the crystals depends strongly on the dopant, going from nearly transparent when doped with Al, Ga, P+Ga, to dark red-brown when doped with Cr.

TABLE 4.1 Doped BGO samples, dopant concentrations and some effects of dopants

Sample No	Dopant	Dopant* fraction in the crystal per formula unit	Colour	Conductivity
11	Al	0.033	Transparent	P
13	Ga	.003 Ga	"	n
253	Ga + Cr	0.006 Ga .00005 Cr	Pale brown	-
241	Cr	.009 Cr	Dark brown	-
1	Zn	< .009 Zn	Yellow	-
15	Pb	> 0.2 Pb	Pale yellow	-
268	P + Ga	.029 P .004 Ga	"	n

* Chemical analysis

4.2 Ultrasonic attenuation results

4.2.1

(1) BGO + Cr. Measurements were made for the (110,001) transverse mode in a sample of BGO doped with (0.009) Cr Fig. 4.1 shows the attenuation versus temperature for 25, 45 and 90 MHz waves. The attenuation curves show a relaxation behaviour as for the undoped BGO. As given in Table 4.2, the peak positions were within ±2K of the corresponding peak positions for the undoped sample, but the height of the peaks (relative attenuation in dB/cm) was largely increased.

(2) BGO + Zn. Fig. 4.2 presents the results obtained for a crystal of BGO doped with < 0.009 Zn. Only one transverse (110, 001) mode was studied. Identical relaxation peaks were seen, but Zn dopant reduced the peak attenuation to 0.72 of the value for undoped crystals.

4.2.2 Analysis of relaxation peaks

The attenuation peaks observed for Cr and Zn doped samples also show all the features of relaxation peaks. Increasing the frequency shifted peaks to higher

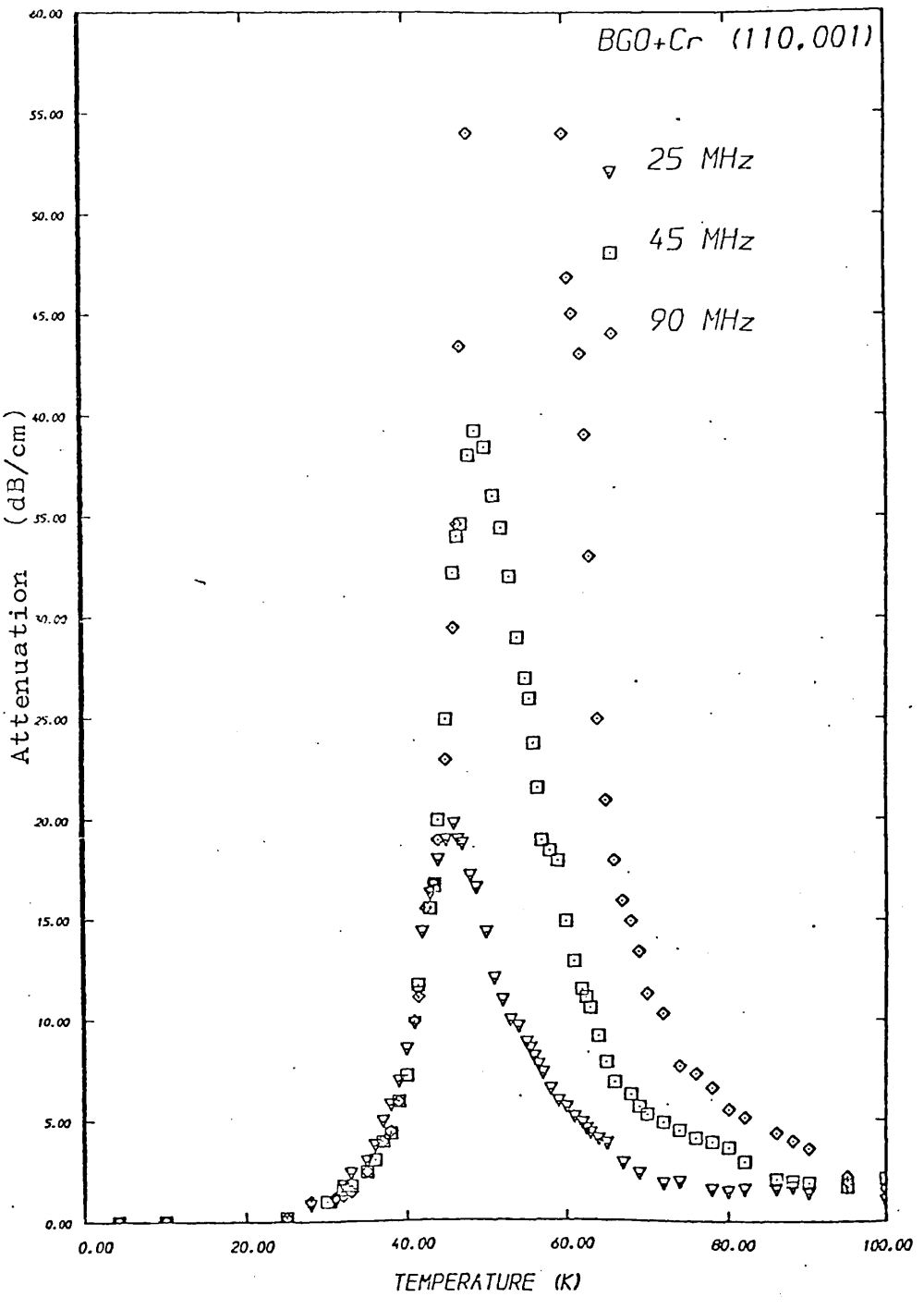

FIG. 4.1 Ultrasonic attenuation for the transverse (110, 001) mode in (BGO + Cr), as a function of temperature and frequency

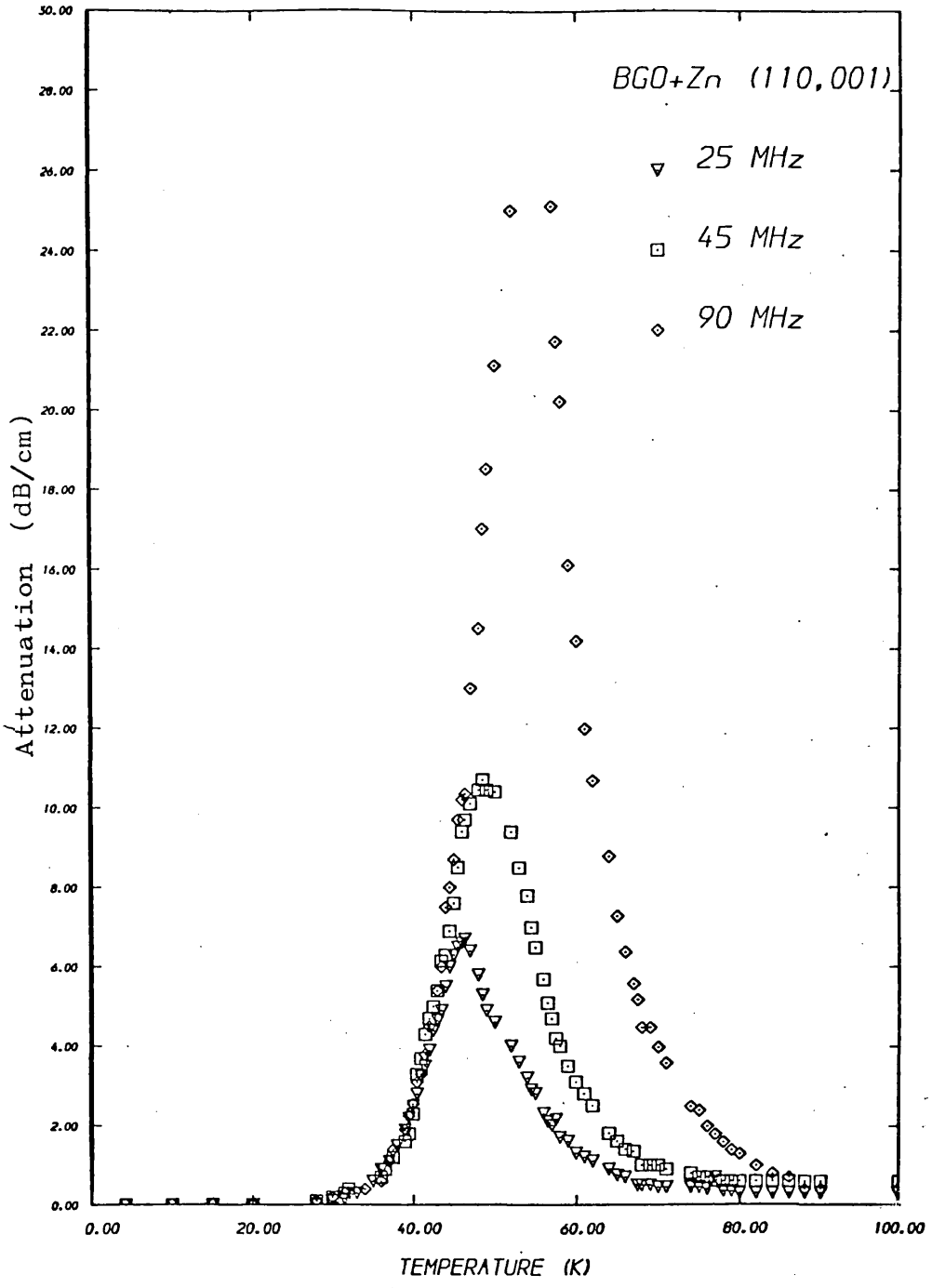

FIG. 4.2 Ultrasonic attenuation versus temperature for the transverse wave (110, 001) in (BGO + Zn) at various frequencies

TABLE 4.2 Peak, attenuation and temperature for doped crystals

Crystal	Dopant	Mode	Freq. MHz	Peak attenuation α_M(dB/cm)	Peak temperature T_M(K)
BGO	-	(110,001)	25	9.3	48.5
	Cr	"	25	19.8	46.0
			45	39.2	48.75
			90	> 60	53.3
	Zn	"	25	6.7	46.35
			45	10.7	48.5
			90	26	54.3
BSO*	-	(111,111)	600	185	-
	Al	"	600	-	-
	Ga	"	600	77	-
	B	"	600	49	-

* Rehwald (1976)

temperatures and the height of peaks increased approximately as ω. These peaks were analysed as explained in Section 3.5.2, using the equation

$$\alpha = \frac{A}{T} \frac{\omega^2 \tau(T)}{1+\omega^2(\tau(T))^2}$$

From the experimental values of peak attenuation, A was calculated and ω and τ were varied to give least squares fitting. The relaxation time was calculated as a function of temperature. Fig. 4.3 and 4.4 give τ versus 1/T from 20 to 80 K. The dashed line on these graphs corresponds to the τ versus 1/T for the undoped sample. This shows that the activation energies of the process involved are the same as for the undoped crystal. The activation energies, attempt frequencies and the corresponding relaxation strengths are given in Table 4.3.

For the Cr doped sample, small deviations were observed at the ends of the peak. The normalized attenuation at two frequencies was plotted as a function of 1/T for this sample as in Fig. 4.5. This also shows that T^{-1}, the shift between the peaks, is constant only from 35 to 60 K. But using equation

$$\Delta(T^{-1}) = (1.144)(2.303/\theta)$$

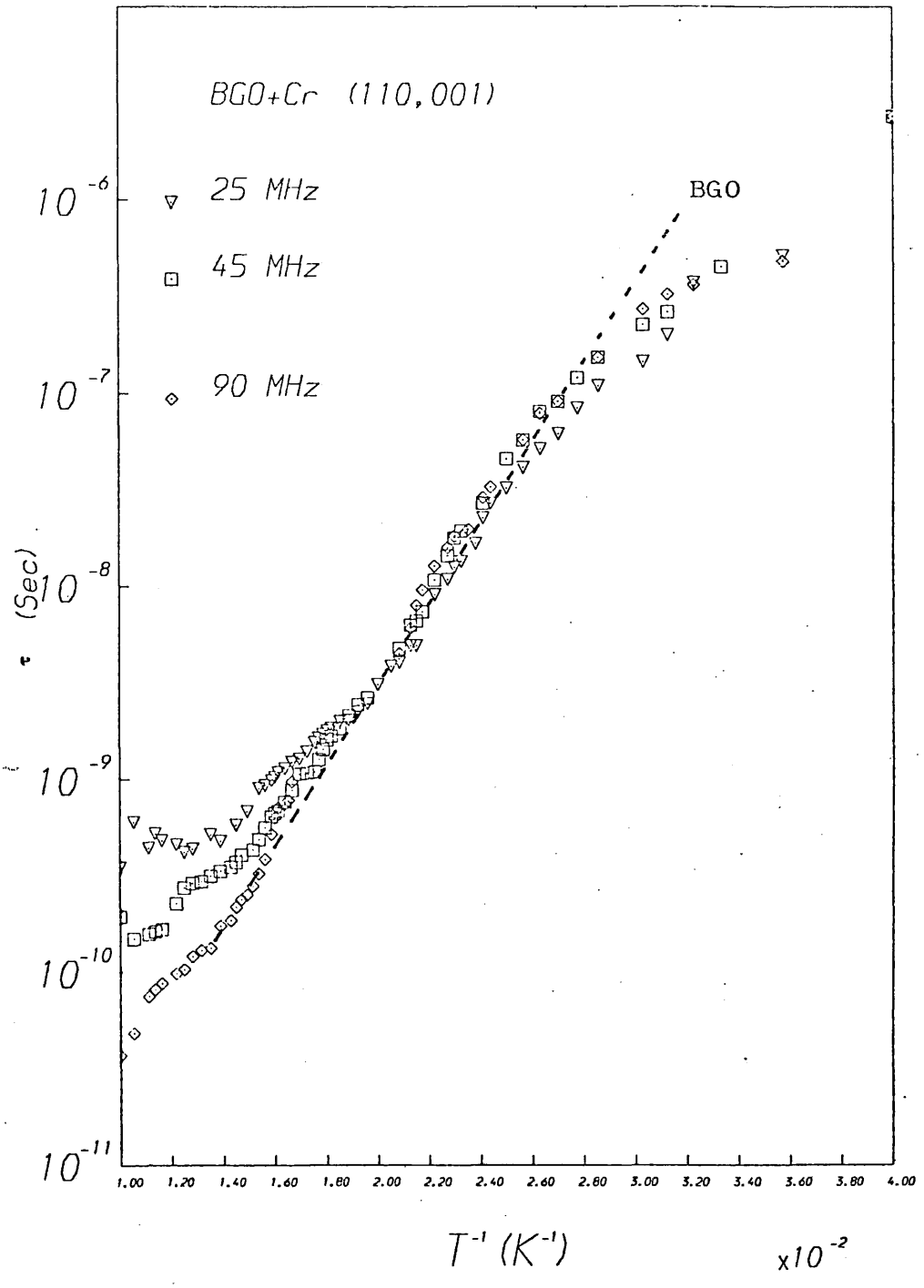

FIG. 4.3 Logarithm of the relaxation time versus reciprocal temperature for a crystal of BGO doped with Cr. The dashed line corresponds to the undoped BGO crystal

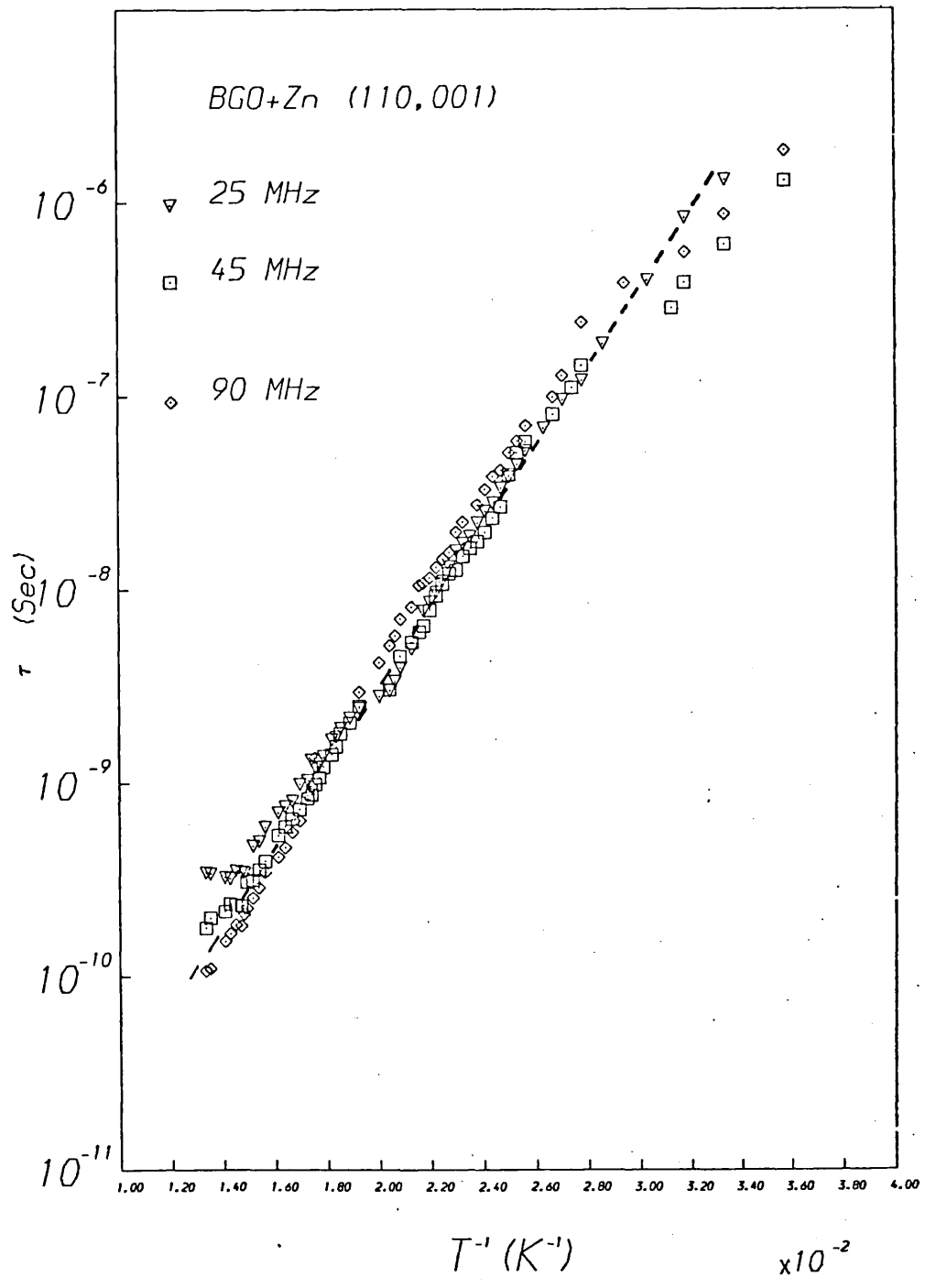

FIG. 4.4 Logarithm of the relaxation time versus reciprocal temperature for a Zn doped crystal of BGO

TABLE 4.3 Activation energies, attempt frequencies, for doped BGO crystals

Crystal	Dopant, Concentration	Frequency MHz	$A = \frac{2\alpha_M T_M}{f}$ dBK/cm MHz	θ K	Q eV	$1/\tau_\infty$ 10^{11}Hz
BGO	0.009 Zn	25	18.8	402±9	.034±.0008	6±1
		45	17.9	411±8	.036±.0007	10±1
		90	22.5	455±7	.039±.0006	24±4
	.009 Cr	45	67.7	380±7	.033±.0006	6±8
		90	64.7	414±10	.036±.0008	6±1

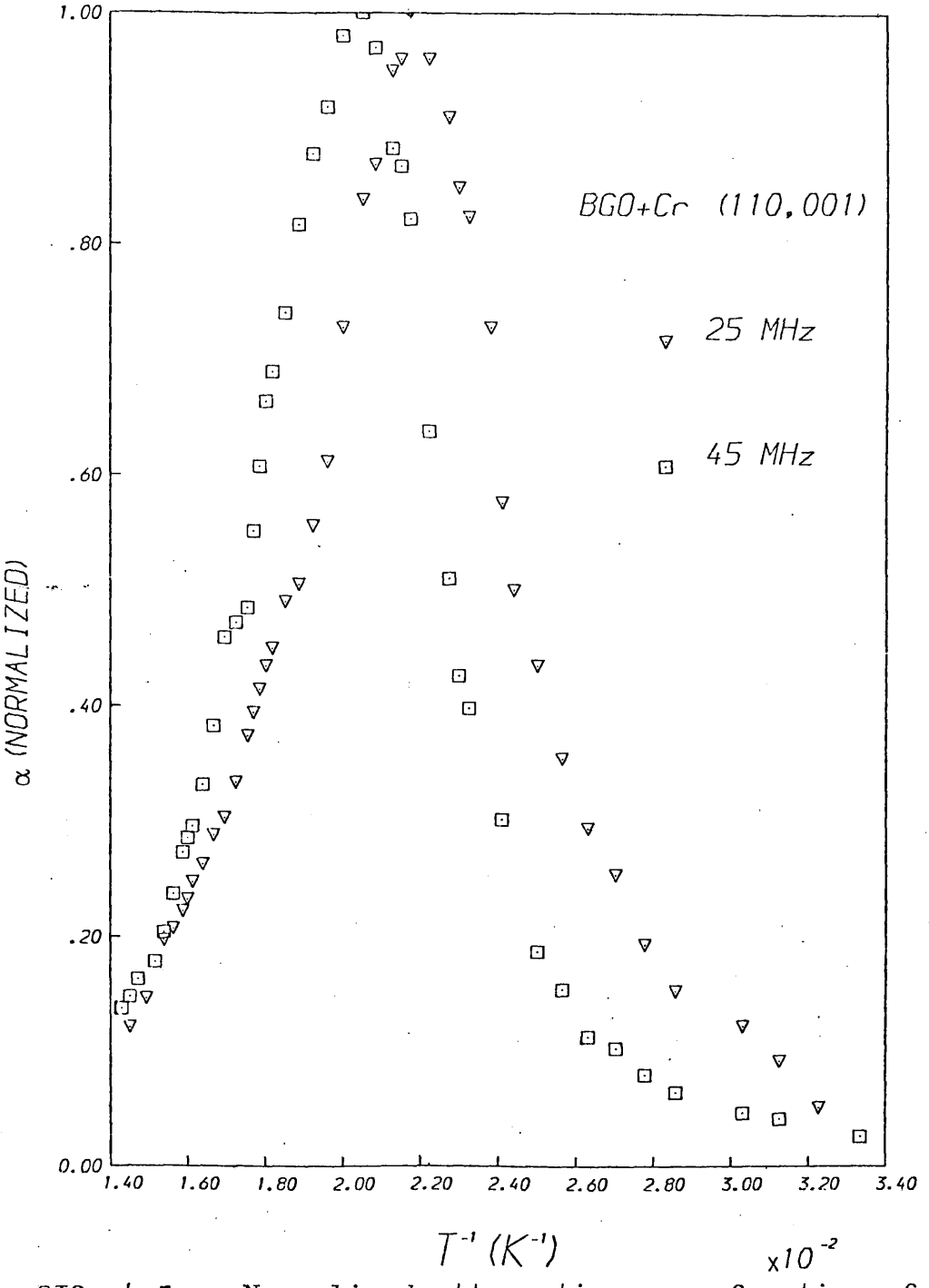

FIG. 4.5 Normalized attenuation as a function of reciprocal temperature for Cr doped BGO sample at two frequencies

the width of peaks at half maximum gives

Crystal	Dopant	Frequency MHz	θ K	Q eV
BGO	Cr	25	455	.039
		45	510	.044

This gives the activation energy to be 0.041 $\pm$ .002 eV.

These results indicate that the same relaxation process is responsible for the attenuation peaks as in undoped crystals, but the strength of relaxation, i.e. the number of defects, has changed.

4.2.3 Results for nearly transparent doped BGO crystals

(1) BGO + Al. A sample of BGO doped with (0.033) Al was transparent unlike the Cr and Zn doped crystals which were dark brown and yellow in colour. Measurements for the transverse T_1 (110, 001) mode at frequencies 15, 30 and 90 MHz are given in Fig. 4.6. This figure shows that the peaks observed for the undoped and Cr, Zn doped BGO crystals are absent. A very small attenuation was observed which increased slowly to ~ 1.5 dB/cm

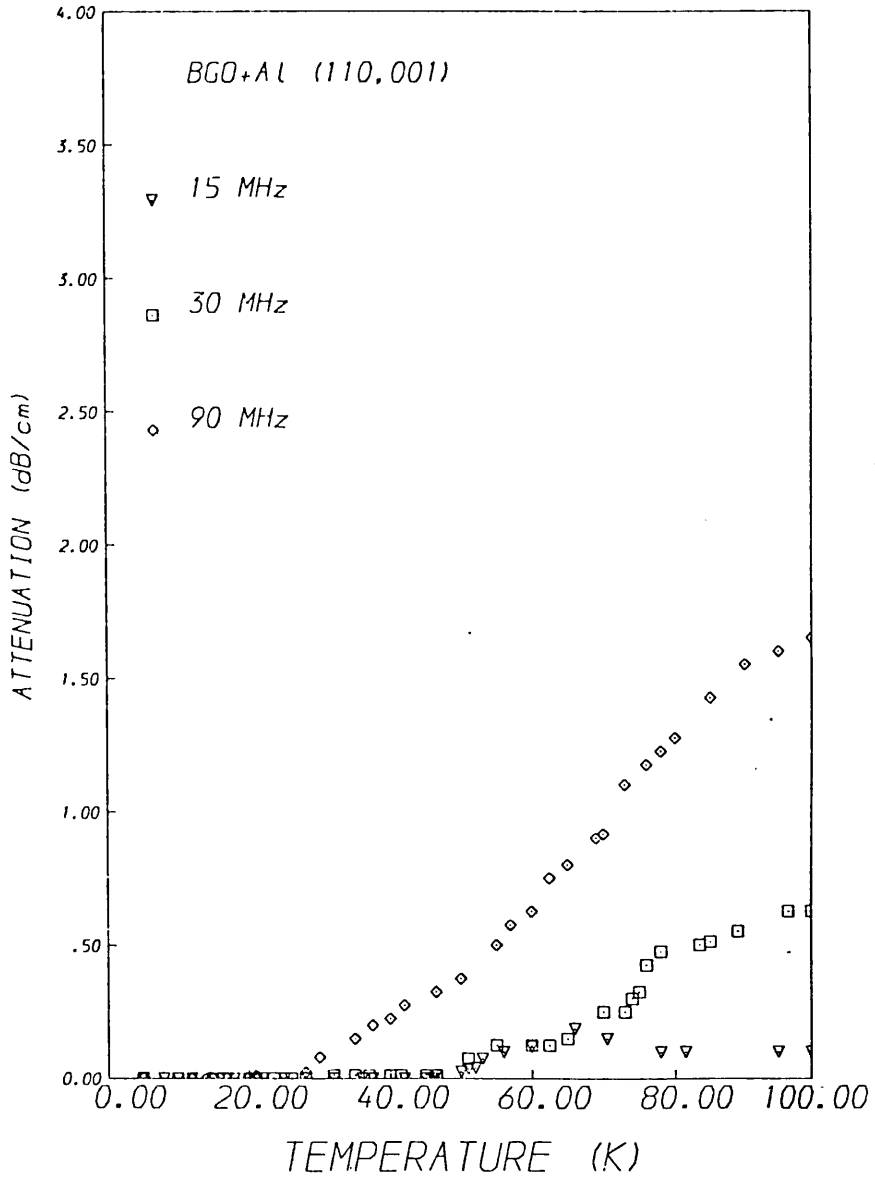

FIG. 4.6 Attenuation as a function of temperature and frequency for the transverse (110,001) mode in (BGO+Al)

at 100 K and then became temperature-independent at ~ 240 K. These measurements complement the work of Rehwald et al (1976) on crystals of the isomorphous material, Bismuth Silicon Oxide, doped with Al (0.008). They also found that Ga (0.002) and B (0.003) reduced the attenuation peaks in BSO. These results are shown in Fig. 4.12.

(2) BGO + Ga. Measurements for a crystal of BGO doped with (0.004) Ga are shown in Fig. 4.7. No peaks were observed even at 190 MHz. Rehwald has reported that (0.002) Ga doping reduced the peak height to approximately 1/3 the value for undoped crystals.

(3) BGO + Pb. Fig. 4.8 shows the results for a (0.5) Pb doped sample. Attenuation increased gradually to about 0.5 dB/cm at 90 MHz.

(4) BGO + P + Ga. This sample doped with (0.029) P, a Group V element, and (0.004) Ga, a Group III element, did not show any peaks. The attenuation versus temperature is shown in Fig. 4.9 for the T (110, 001) mode at 25, 45 and 90 MHz.

(5) BGO + Ga + Cr. Cr concentration in this crystal (5×10^{-5}) is much smaller than in Sample No. (241) No peak was seen at 45, 90 and 190 MHz for the transverse (110, 001) mode as in Fig. 4.10.

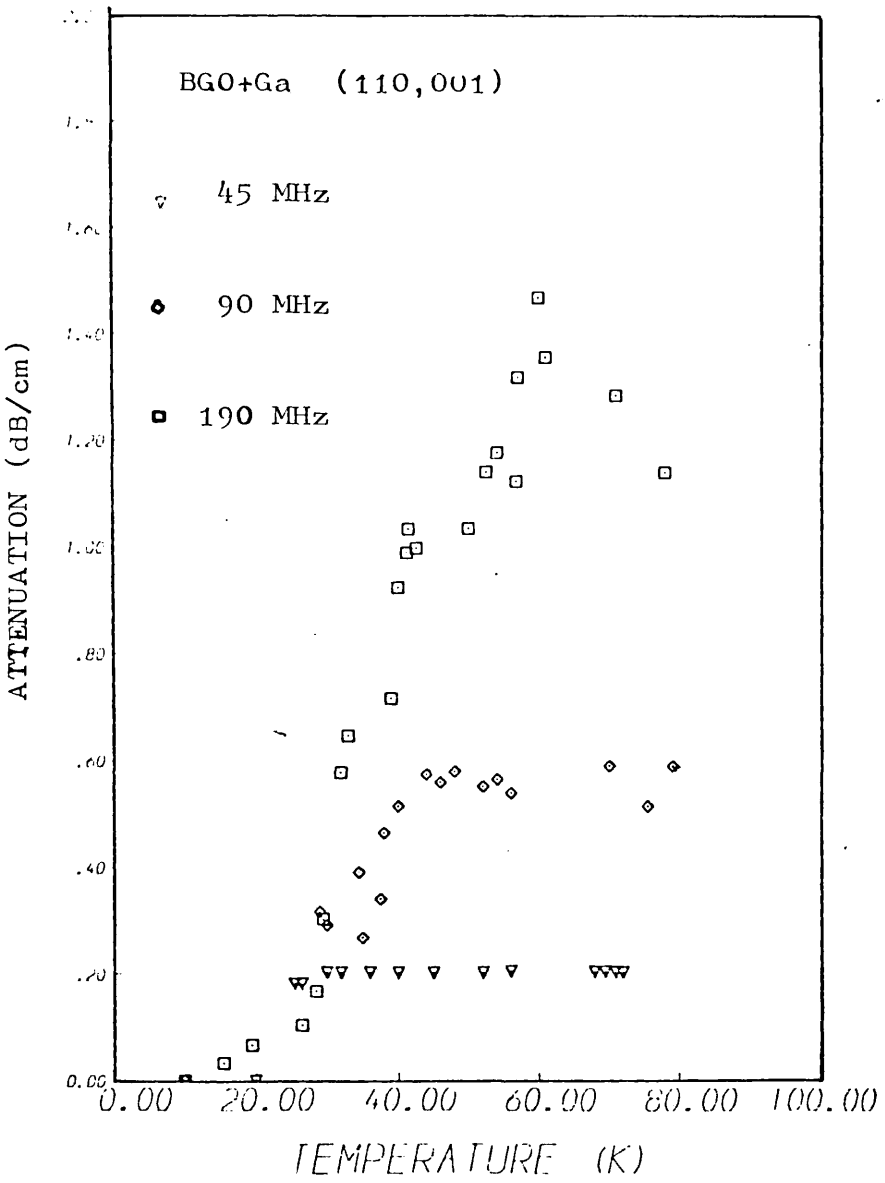

FIG. 4.7 Attenuation as a function of temperature and frequency for the transverse (110,001) mode in (BGO+Ga)

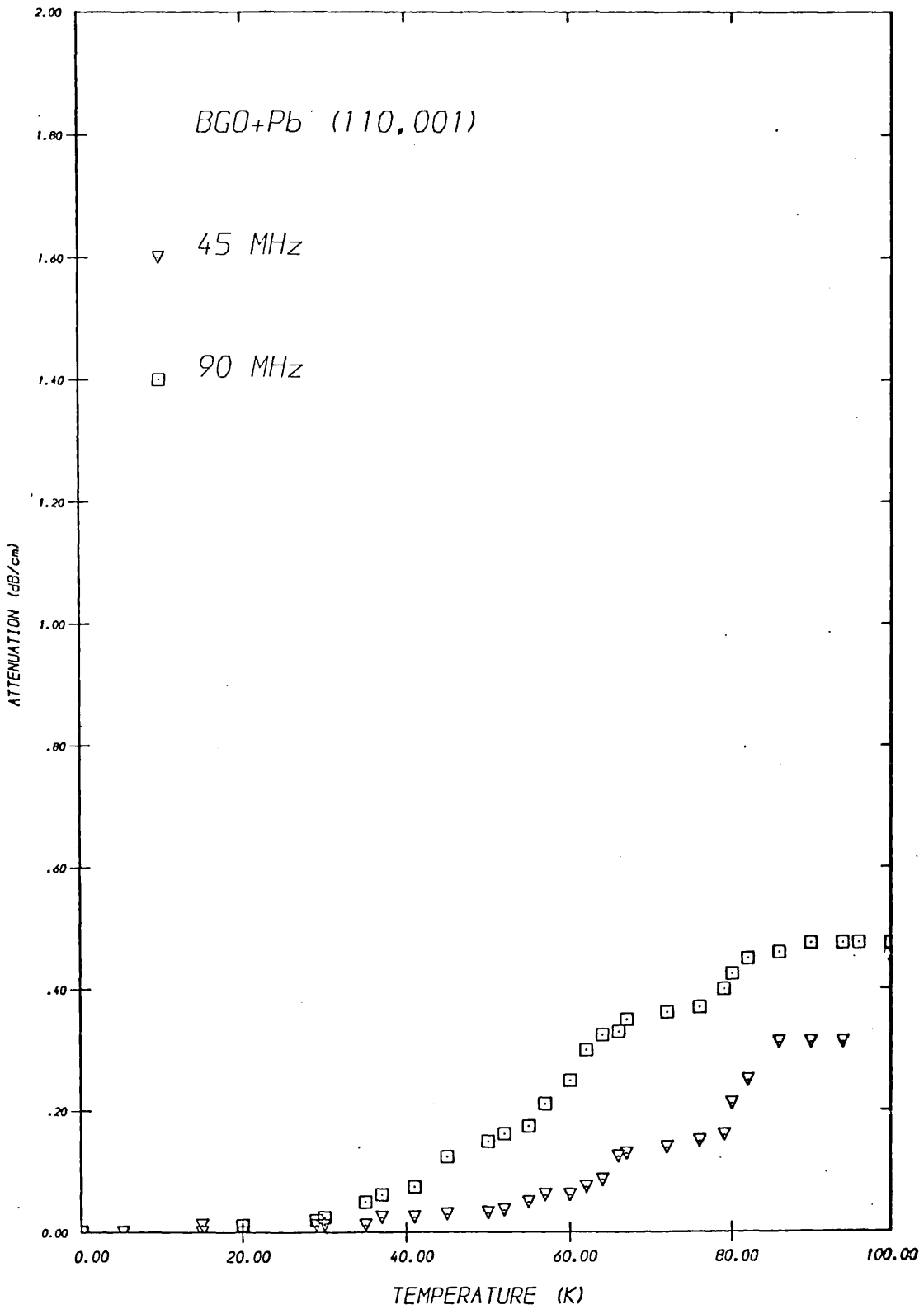

FIG. 4.8 Attenuation for the transverse (110, 001) mode in a crystal of (BGO + Pb) as a function of the temperature and frequency

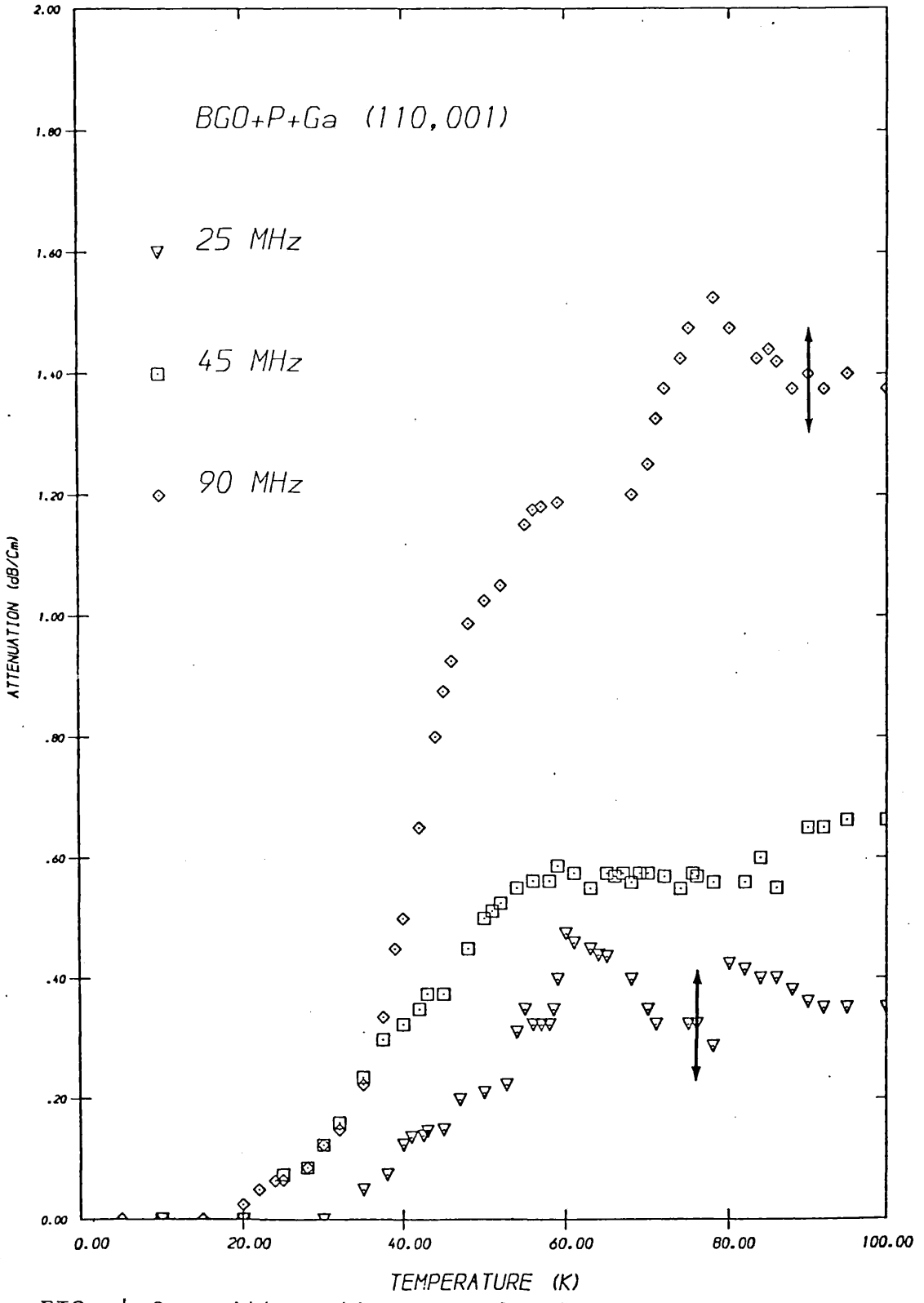

FIG. 4.9 Attenuation as a function of temperature in BGO +(P + Ga) for the transverse wave (110, 001)

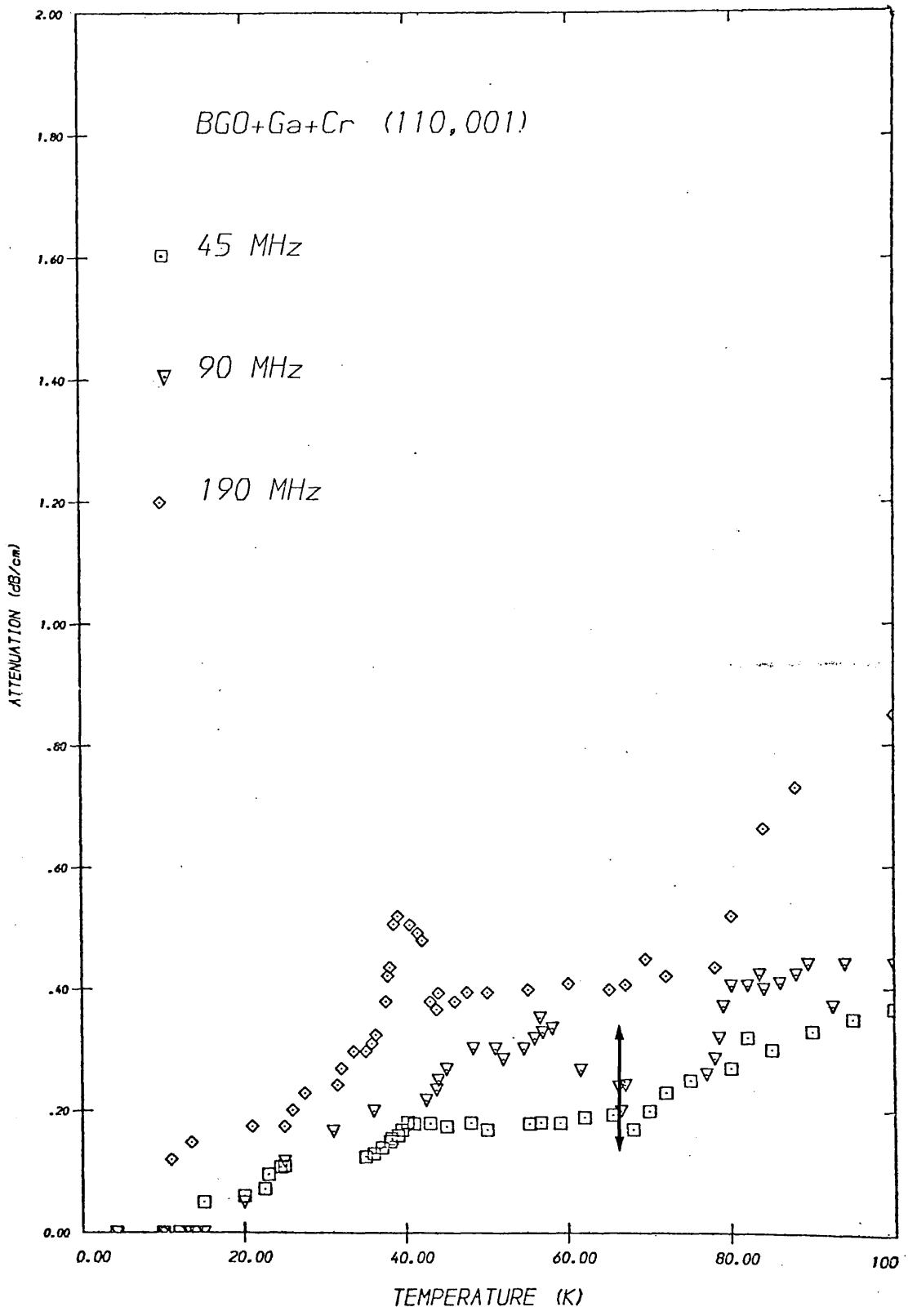

FIG. 4.10 Attenuation in (BGO + Ga + Cr) crystal as a function of temperature and frequency

Fig. 4.11 shows the attenuation for all doped crystals at 90 MHz from 4.2 to 240 K. The attenuation for samples with Al, Pb, Ga, P + Ga and Cr + Ga show the usual phonon-phonon behaviour and is discussed in the next chapter.

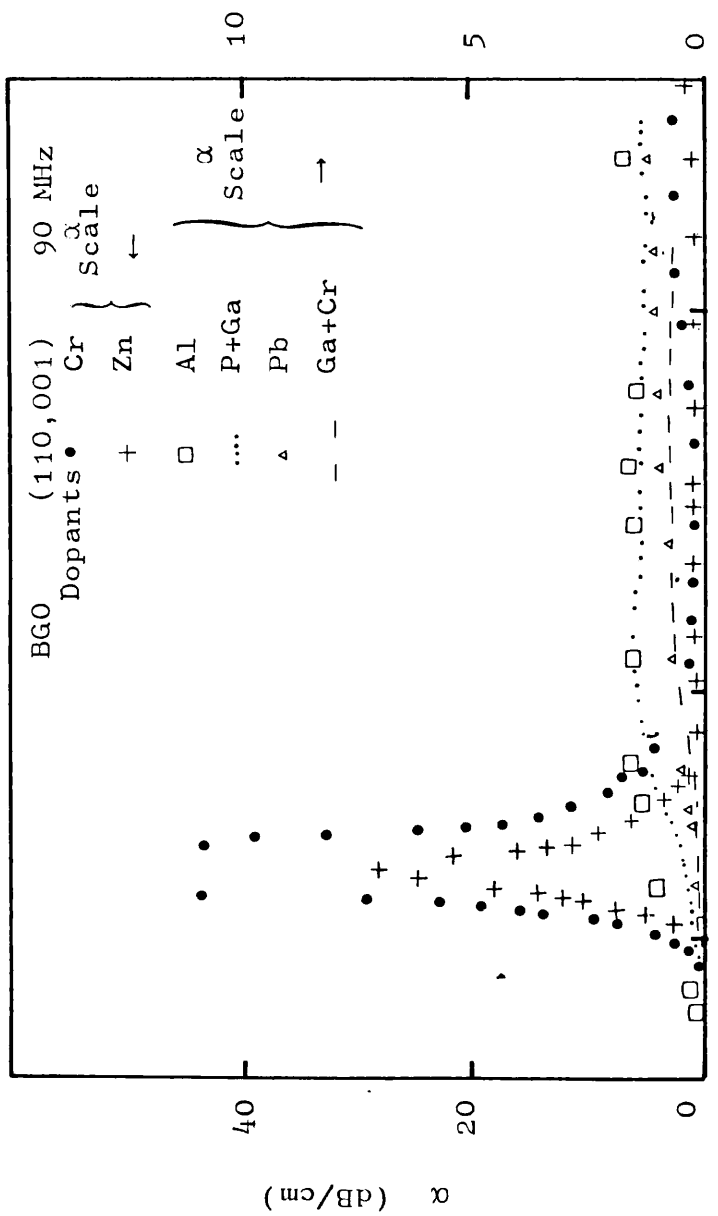

FIG. 4.11 Attenuation as a function of temperature for all doped crystals

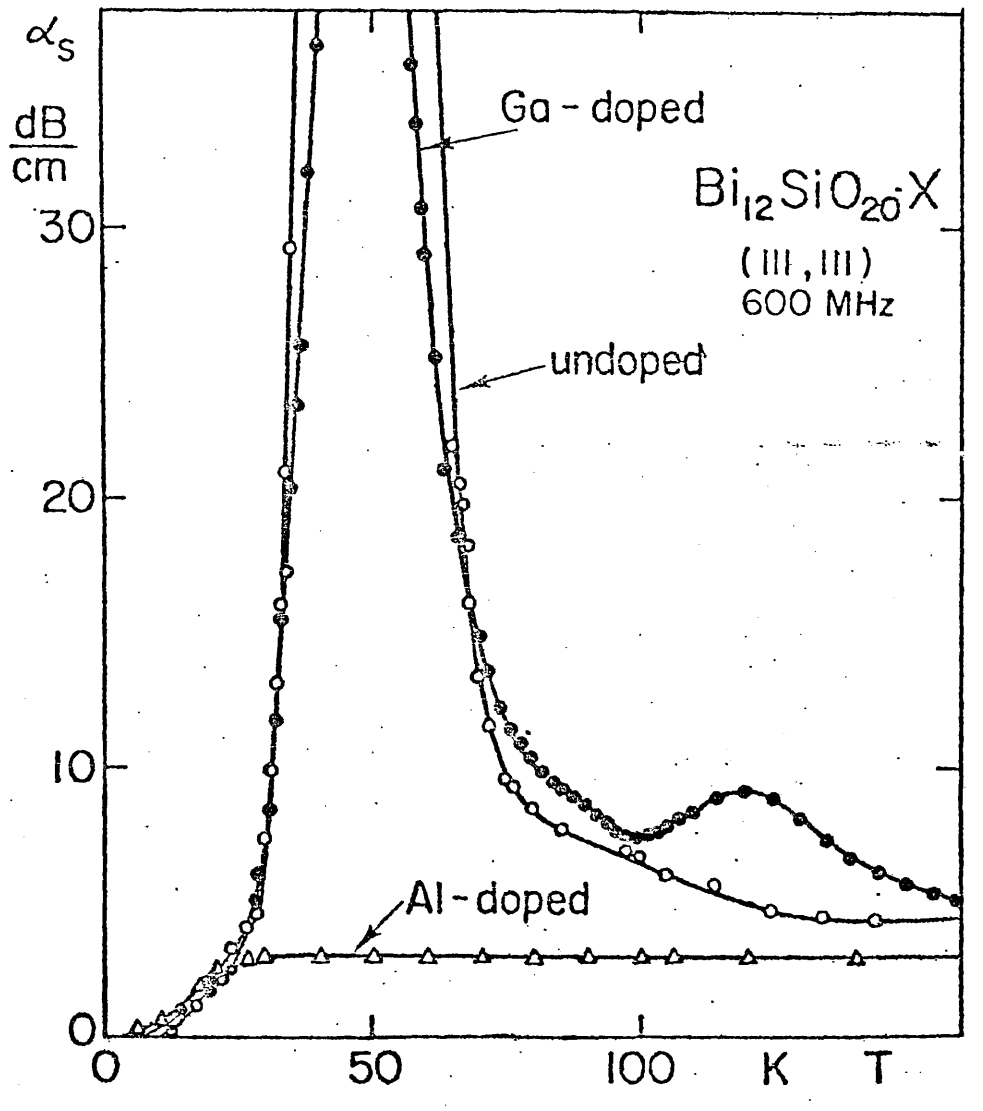

FIG. 4.12 Ultrasonic attenuation of longitudinal waves (111, 111) at 600 MHz, as a function of temperature for undoped, Ga-doped and Al-doped BSO (Rehwald, 1976).

4.3 Correlation with optical absorption

The optical absorption in undoped single crystals of BSO has been studied by Hou, Aldrich and Harvill (1971), Tanguay (1977) and for BGO by Oberschmid (1978). As shown in Fig.1.6 the absorption coefficient shows a broad shoulder between 2.3 and 3.1 eV, and an Urbach-like exponential absorption beyond 3.1 eV. All these results give the room temperature band gap as 3.25 eV. The cause of the broad shoulder is not clear, but Hou et al (1973) explained the additional absorption to be due to a Si vacancy complex situated 2.6 eV below the conduction band when occupied by an electron. The optical absorption spectrum for the doped BGO samples which were used for attenuation measurements in this work have also been studied by Oberschmid and Grabmaier (1978). As can be seen from Fig. 4.13, the absorption depends strongly on the dopant present.

4.3.1 Effect of Cr dopant on optical absorption

As shown in Fig. 4.13, Cr doping, increased the optical absorption to approximately 20 times the absorption in an undoped sample (Oberschmid), throughout the wavelength range from 2.1 eV to beyond 3.25 eV.

Tanguay (1977) has also recorded the transition spectra for the undoped and Cr doped BSO. He noticed a significant increase in the strength of the optical absorption peaks for the Cr doped sample, compared to that for the undoped.

4.3.2 Effect of Zn dopant on optical absorption

Oberschmid (1979) reports that Zn dopant did not change the optical absorption significantly.

4.3.3 Effects of other dopants

Doping BGO with Al, Ga, P, P + Ga have been observed (Oberschmid 1978) to reduce the optical absorption within the band gap, from 2.1 eV to 3.25 eV. This reduces the shoulder observed for the undoped samples. These results complement the previous work of Rehwald (1976) and Hou et al (1973) on doped BSO. They studied the effect of doping BSO with Al^{3+} and Gallium as shown in Fig. 4.14.

4.3.4

The attenuation results for doped BGO crystals given in Section 4.2 show that Cr-doping increases the peak attenuation, Zn reduces it and all others, Al, Ga, P etc. remove the peak. The optical absorption results

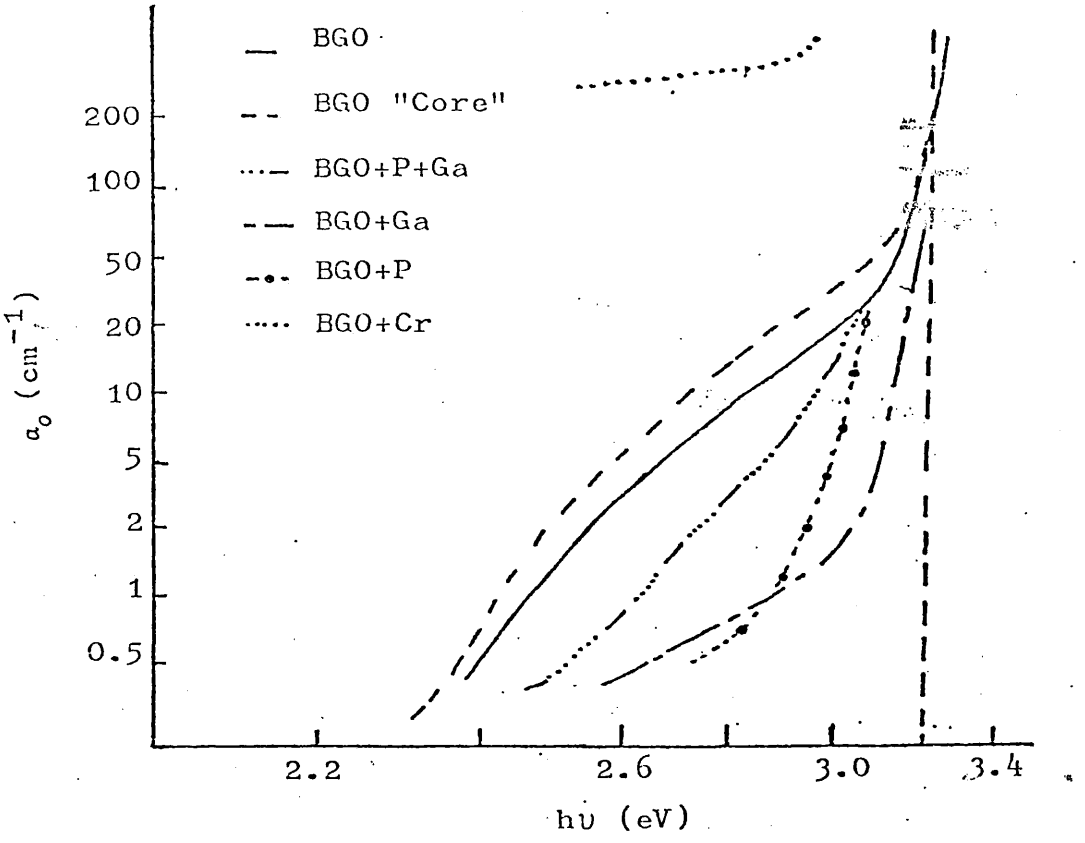

FIG. 4.13 Optical absorption versus photon energy for undoped and doped BGO

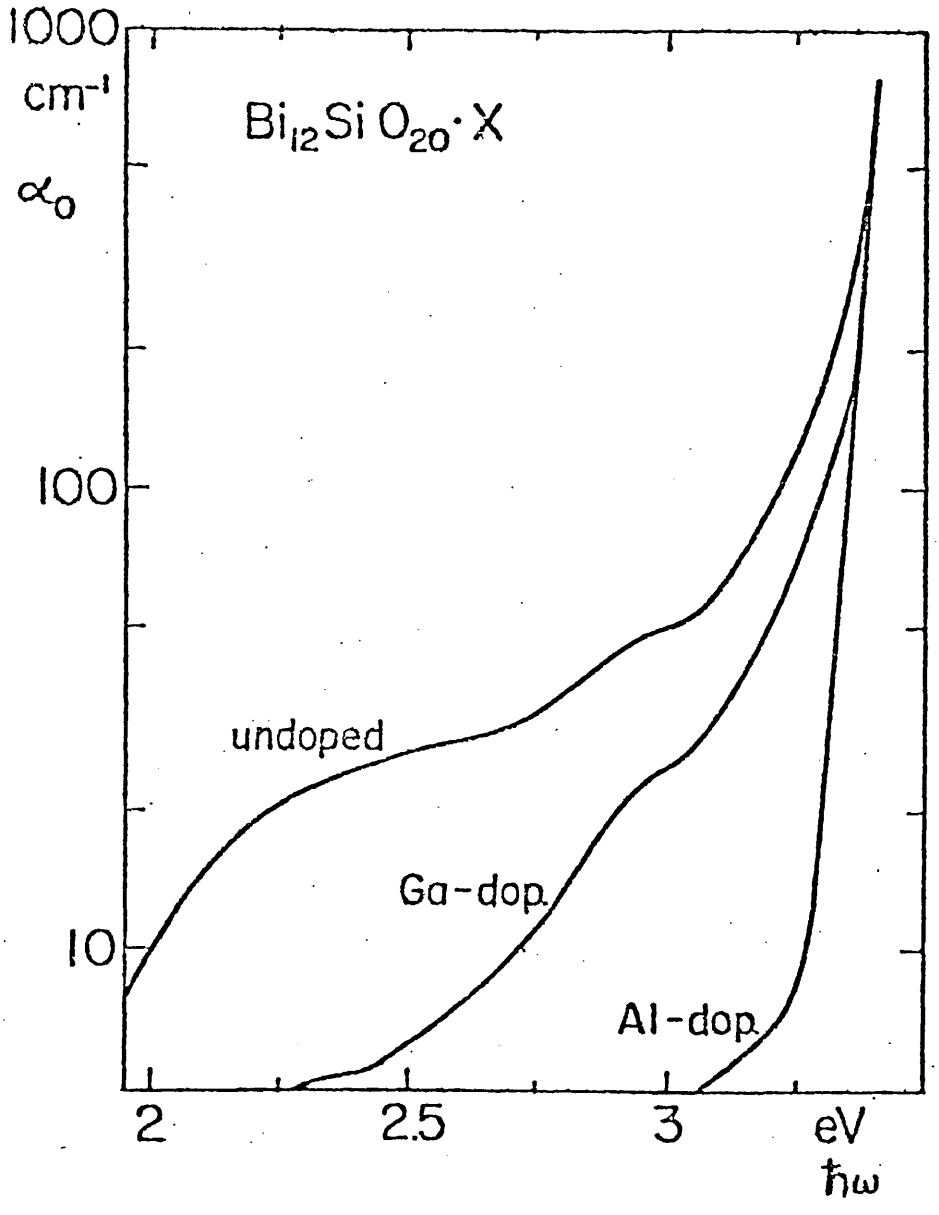

FIG. 4.14 Optical absorption coefficient at liquid nitrogen temperature versus photon energy for undoped, Ga-doped and Al-doped BSO

for all these samples quoted above indicate that dopants have similar effects on the optical absorption and ultrasonic attenuation peaks. Therefore, as previously suggested by other workers, the optical and ultrasonic absorption centres seem to be related. The possible centres responsible for these effects are discussed in the last chapter.

4.4 Effects of annealing and γ-irradiation on point defects in BGO, BSO

Since this material shows interesting optical and photo-conductive properties, Autnov, Arsenyer et al (1976) have carried out a detailed study on point defects in single crystals of BGO. Effects of annealing in reducing or oxidising atmospheres and γ-irradiation, on the optical absorption have been studied. They report that in the absorption spectrum of BGO a weak, wide band, A, is always present in the range of 700 nm and they assign this band to a constant structural defect. By exposing the samples to ultra violet light, two bands, B and C, were observed. To examine the defects produced in reducing the atmosphere, samples were annealed in vacuo and in hydrogen, in the temperature range 400 to 800°C. As shown in Fig. 4.15 (a) and (b), bands A, B, C were intensified and another band, D, was also noted.

An intensive growth of the four bands was also reported by treating BGO samples by gamma irradiation.

Annealing in oxidising atmospheres up to 700°C has been reported to destroy all colour centers produced by vacuum annealing or irradiation.

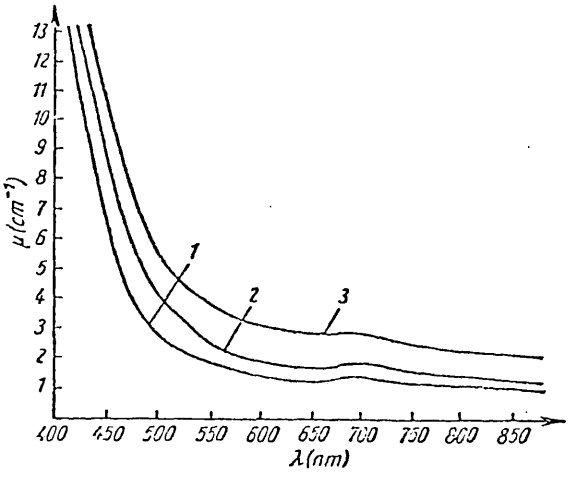

(a) Absorption spectra of crystals $Bi_{12}GeO_{20}$. 1. Initial sample. 2. Irradiation by ultra-violet radiation for 10 hours. 3. Irradiation by gamma-rays, 150 megaroentgens dose

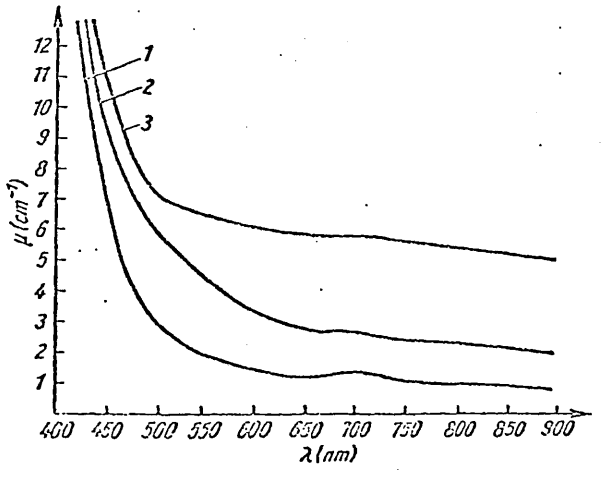

(b) Absorption spectra of crystals $Bi_{12}GeO_{20}$ treated in vacuum for 6 hours at temperatures 600°C(2), 740°C (3). 1. Initial material

FIG. 4.15 Effects of irradiation on optical absorption

Since the ultrasonic attenuation peaks observed in the low temperature region are due to the anelastic relaxation of point defects, attenuation measurements were made on the annealed and irradiated samples to investigate the effects of changing defect concentration on attenuation.

4.5 Experimental results in annealed BGO

4.5.1 Undoped BGO

A crystal of BGO with <111> orientation was used to study the effects of annealing on the attenuation peaks. The crystal was first annealed in vacuo at 450°C for 24 hours, using a resistance-heated (JMC-type T) furnace, modified to give a controlled heating and cooling rate (less than 50°C per hour), as shown in Fig. 4.16.

A slight change in colour (from pale yellow to pale greenish-yellow) was observed but there was no change in the attenuation for the L(111, 111) mode. A vacuum annealed sample was then annealed under similar conditions, in an oxygen atmosphere of 2 p.s.i. Attenuation measurements were repeated again but no change was noticed, as can be seen from the raw data in Fig. 4.17, 4.18 and 4.19.

Autonov et al (1976) from studies of the kinetics of defect formation, reported that up to 500°C the rate of defect formation is not high and increases sharply above 500°C. It may be possible that if we annealed the samples at higher temperatures (> 450°C) we could observe some effect, but because of lack of time further annealing was not carried out.

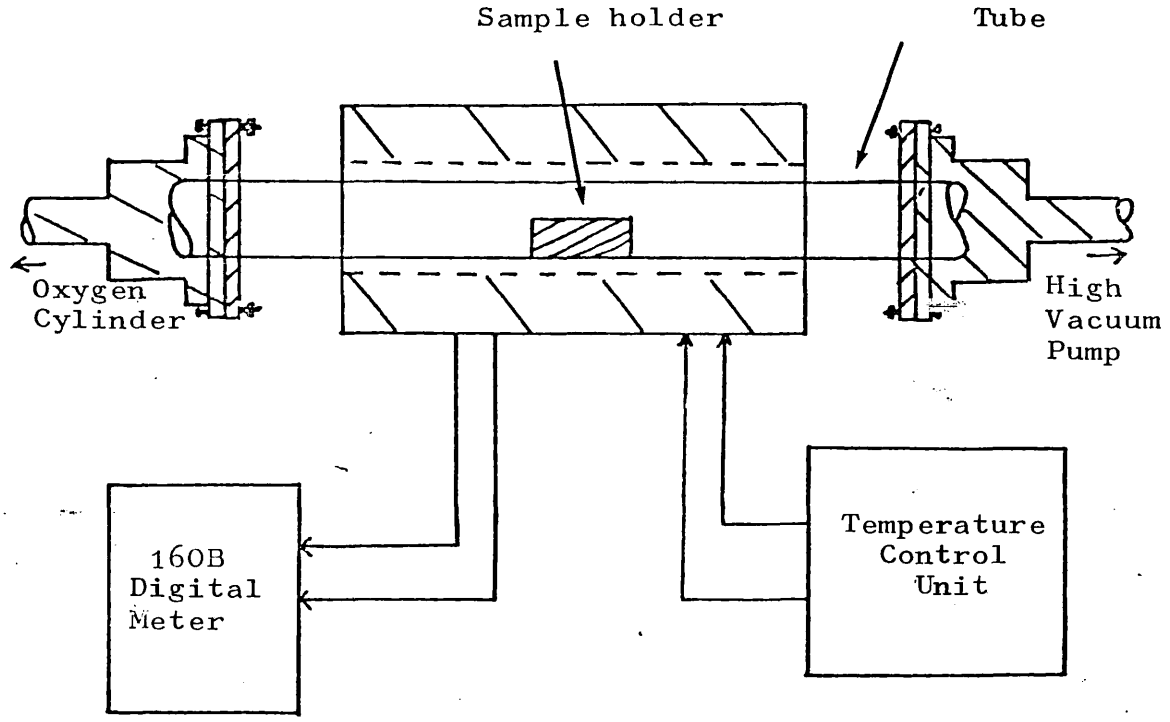

FIG. 4.16 Block diagram of experimental set up used for annealing

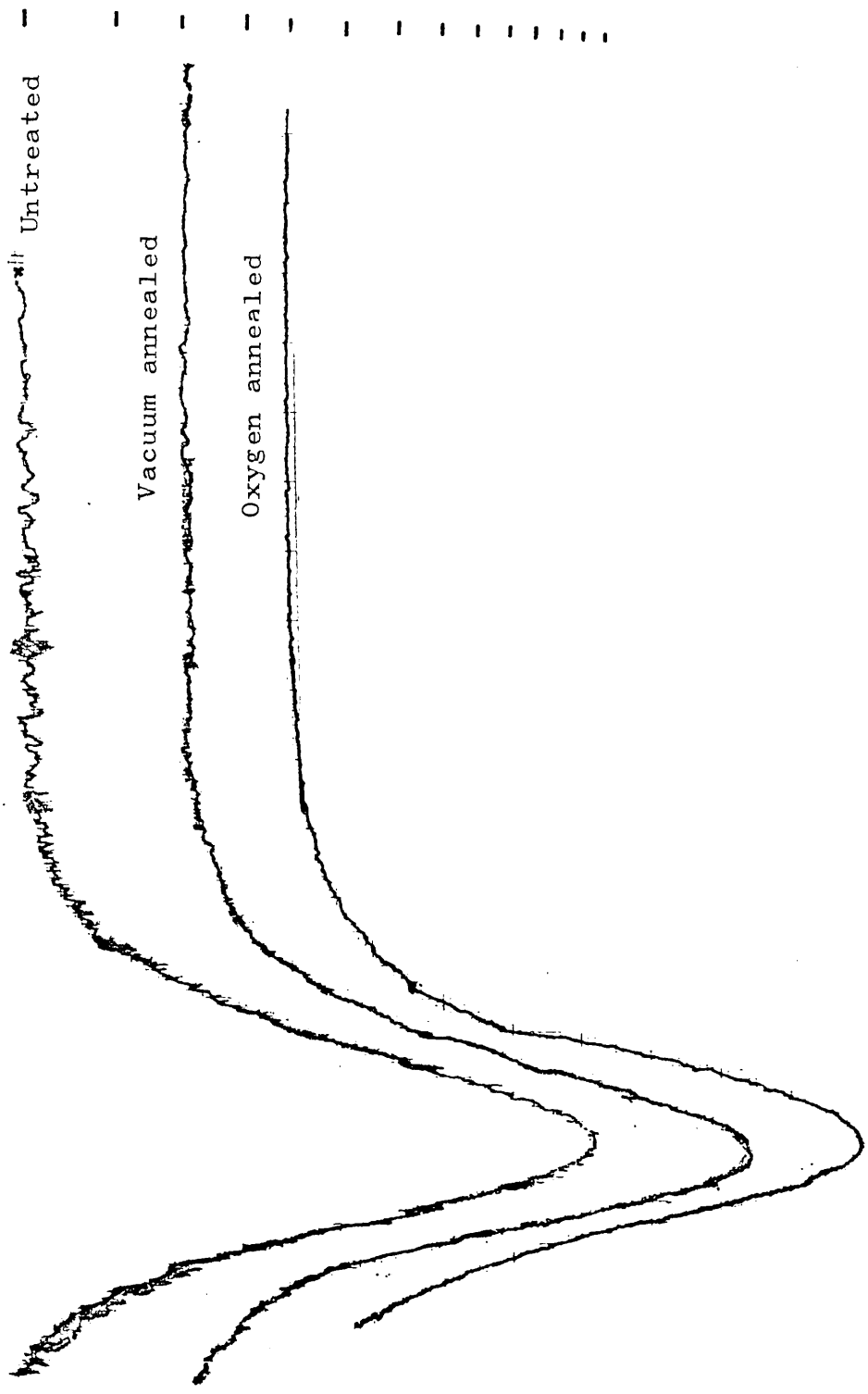

FIG. 4.17, 4.18 , 4.19 Raw data plots for attenuation of L(111,111) mode in untreated and annealed BGO

Tanguay (1977) also studied the effects of annealing on the optical absorption of BSO. He found that the absorption in undoped BSO was unaffected by vacuum or oxygen annealing. This correlates with our results of undoped BGO.

4.5.2 Data for Cr-doped BGO

Wardzynski and Lukasiewicz (1979) have observed that the Mn and Cr doped crystals of BGO changed colour from pale yellow and red to brown and dark red on illumination with visible light, but could be switched back to the original colour by heating the crystals to about 150°C in dark. They have measured the absorption spectrum before and after illumination and also after annealing. The spectrum before illumination and after annealing was found to be the same.

Some attenuation measurements were made on annealed Cr-doped crystals, to see the effect, if any. The sample was annealed in vacuo as previously explained and the attenuation was measured. The peak attenuation was found to be reduced to 0.57 of its original value.

The vacuum annealed sample was then annealed in oxygen atmosphere under similar conditions. Oxygen annealing restored the attenuation to its original value. All three curves are shown in Fig. 4.20. These peaks were

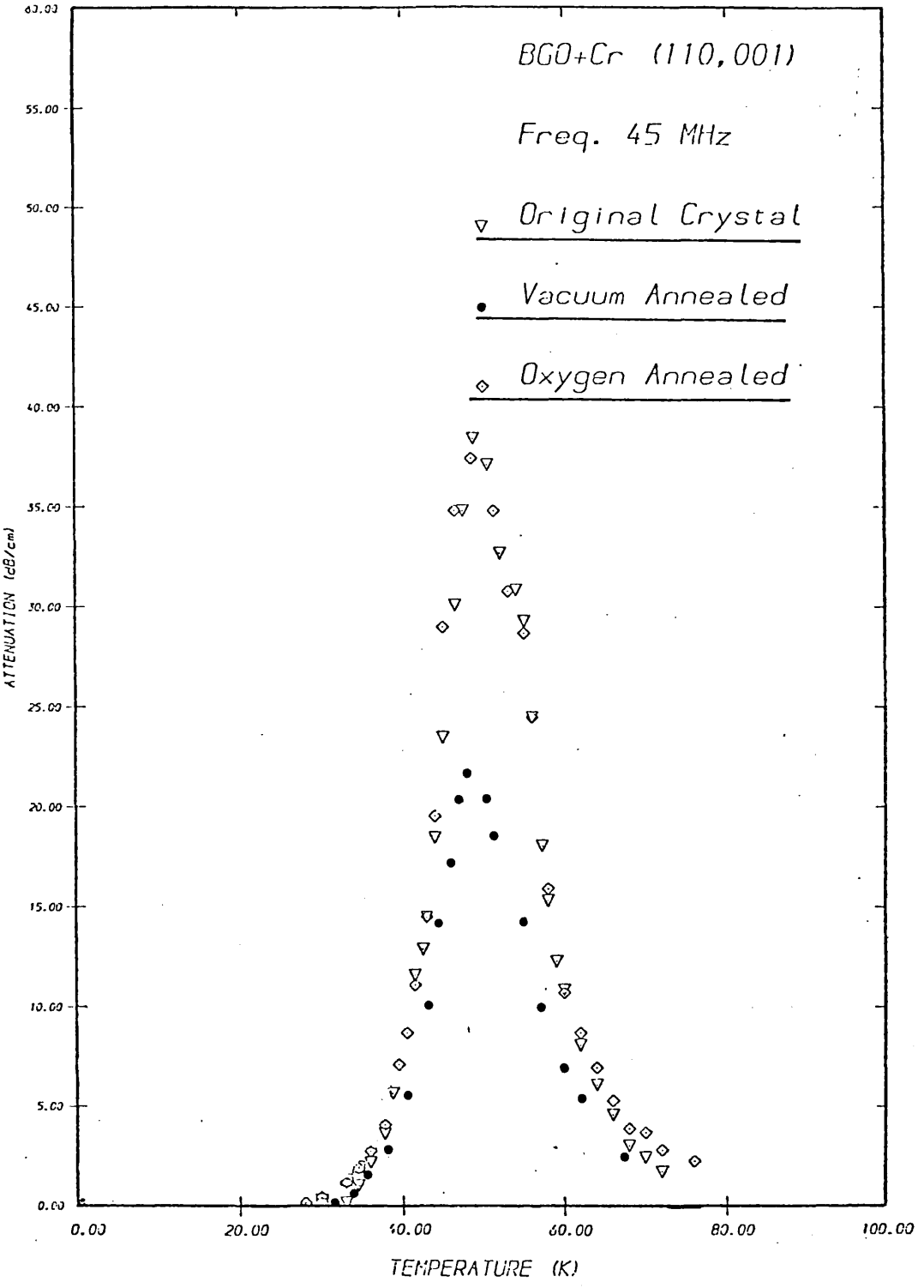

FIG. 4.20 Ultrasonic attenuation for the transverse (110, 001) mode in a Cr-doped crystal (▽) initial sample, (•) vacuum-annealed and (◇) Oxygen-annealed.

analysed as before and Fig. 4.21 shows the relaxation time versus 1/T for the three cases. This indicates that the activation energy of the relaxation process is unchanged, and only the relaxation strength has changed. Therefore, the relaxing defect density seems to be changed by vacuum-annealing.

But, for Cr-doped BSO, Tanguay found strong photochromic behaviour with strong optical absoprtion bands which would be bleached by oxygen annealing, but reappeared after illumination by light pulses.

To explain this behaviour, Wardzynski et al (1979) assumed a light-induced charge transfer process. From EPR measurements they indicate that Cr occupies the Ge or Si sites. Tanguay also considers a charge transfer process to be responsible for this optical absorption behaviour. He assumes that addition of Cr^{3+} on a tetravalent site induces a Bi^{5+} ion to occupy an adjacent Si^{4+} site for charge compensation. A charge transfer mechanism between neighbouring substitutional Cr and Bi ions on tetrahedral sites could produce two metastable states (absorbing and non-absorbing). Our data on Cr-doped BGO suggests that one of these states may be the centre responsible for the ultrasonic attenuation.

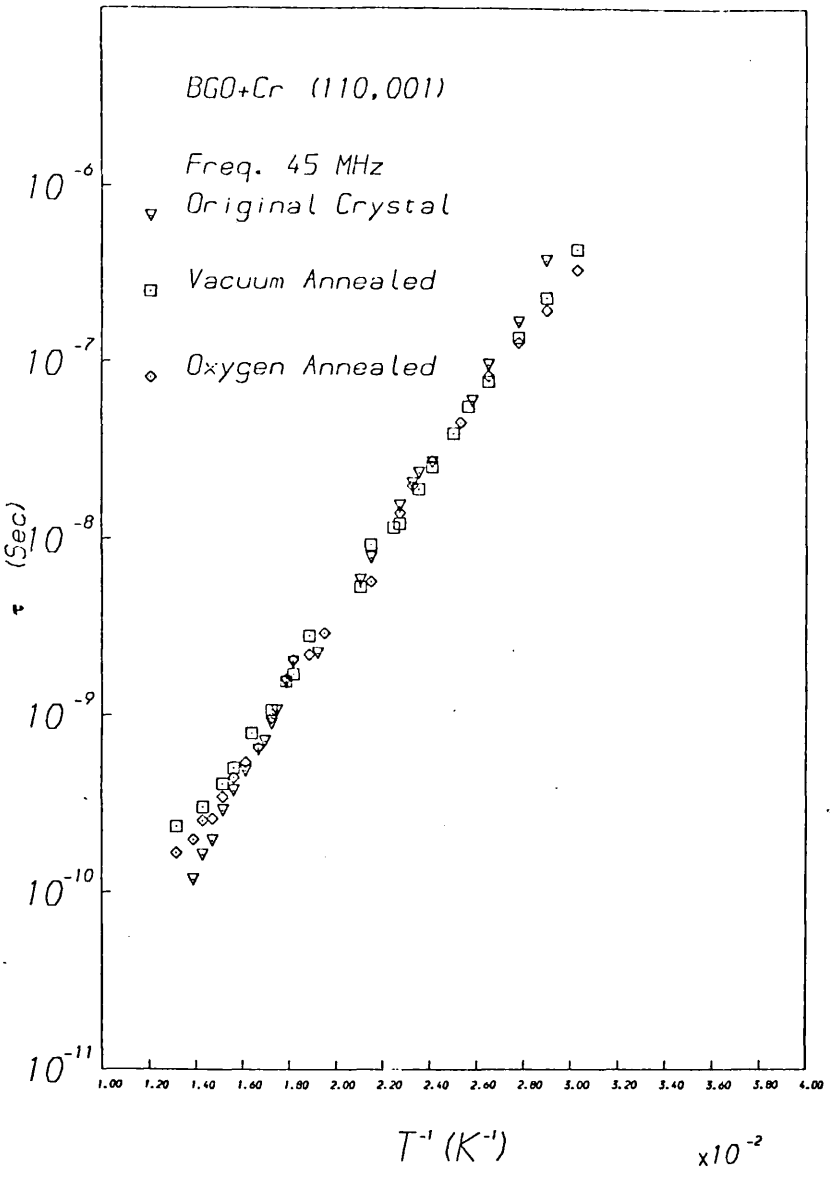

FIG. 4.21 Logarithm of the relaxation time versus reciprocal of temperature for the annealed (BGO+Cr) crystal

4.6 Experimental results in gamma-irradiated BSO

In order to study the effects of defects produced by irradiation on the ultrasonic attenuation, a cylindrical rod of $Bi_{12}SiO_{20}$, with <110> orientation, was used.

Gamma irradiation was carried out using a cobalt-60 source (Imperial College, London) at room temperature. Successive doses of .5, 1, 1.5. 3.0, 6.0 and 12 Mrad were used and the attenuation measurements repeated after each dosage. Fig. 4.22 shows the attenuation measured at 25MHz for the transverse (110, 001) wave as a function of temperature for various doses. Below the peak temperature, i.e. in the region $\omega\tau > 1$, the attenuation was unchanged for irradiation doses from .5 to 12 Mrad. The peak attenuation and the attenuation above the peak temperature was unchanged after a dose, R, of .5 Mrad but decreased by about 20% for R = 1 Mrad. As the dose was further increased, reaching 3 Mrad, the peak attenuation started increasing again. But further increas in dose, i.e. 6 and 12 Mrad, had no appreciable effect. Table 4.4 gives the attenuation as a function of temperature and irradiation. Fig. 4.24 shows the effect of various doses on the peak attenuation and peak temperature.

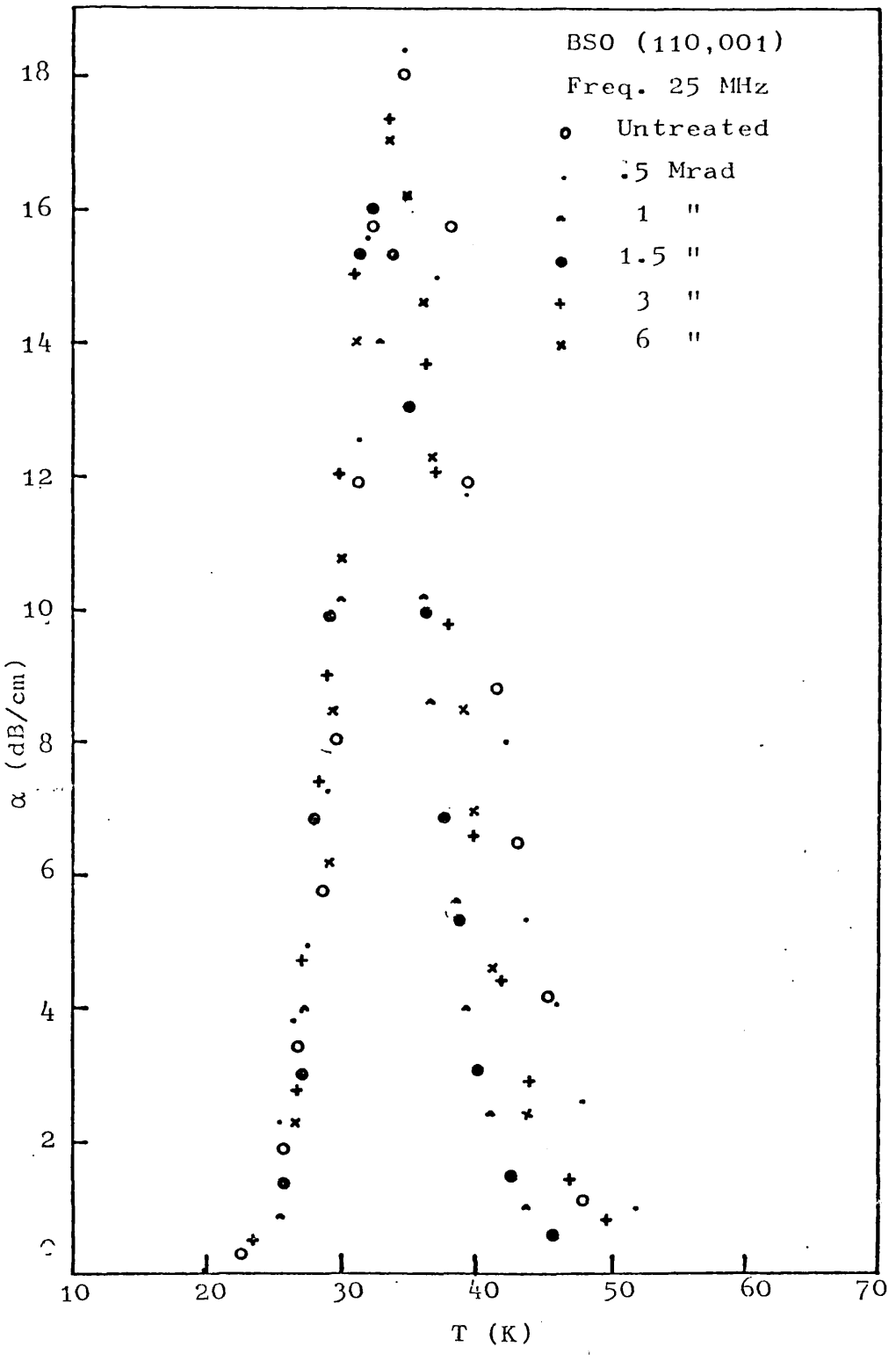

FIG. 4.22 Attenuation for the transverse (110,001) mode in γ-irradiated BSO

TABLE 4.4 Effect of irradiation on attenuation

Dose Mrad	Temperature K	Attenuation (dB cm^{-1})
—	25.	2.0
	34.5	18.
	40.	11.
1.	25.	0.7
	33.	14.1
	40.	3.4
1.5	25.	0.9
	33.	15.
	40	3.6
3.	25	1.2
	33.5	17.3
	40	6.6
6.	25	1.1
	33.5	17.3
	40	7.0

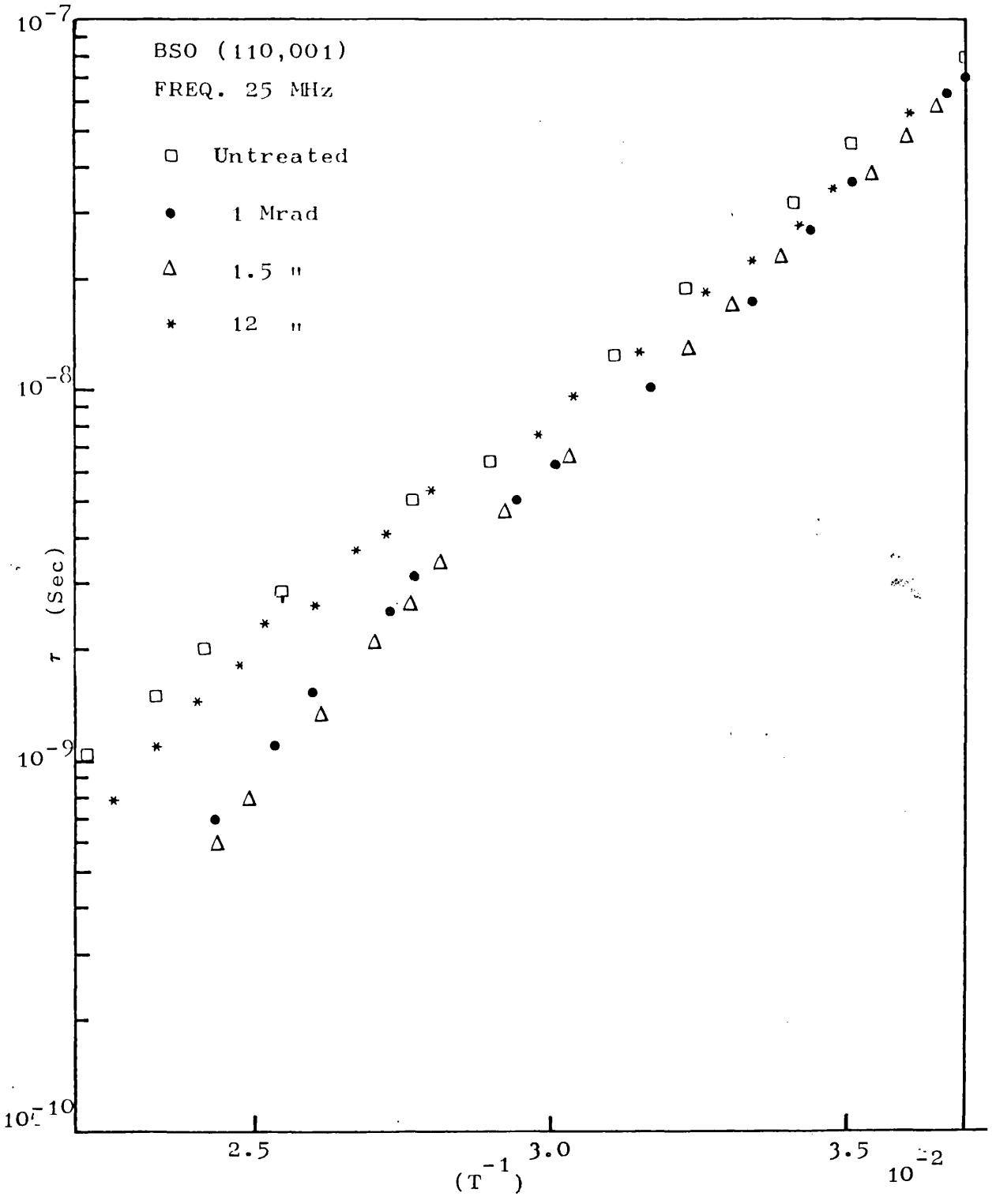

FIG. 4.23 Logrithm of the relaxation time versus reciprocal of temperature for transverse (110,001) mode in γ-irradiated BSO

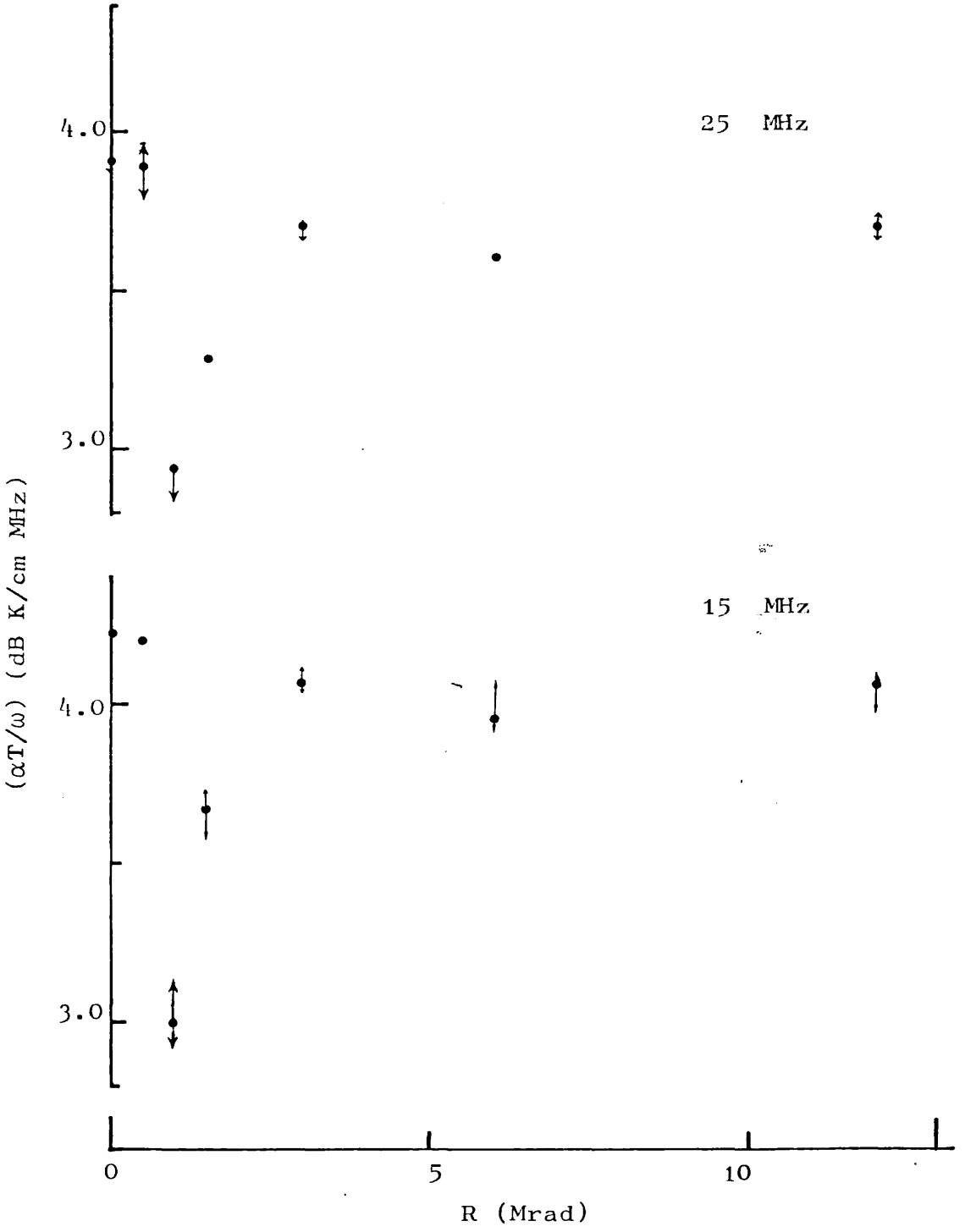

FIG. 4.24 Effect of irradiation on peak attenuation

The attenuation peaks were analysed using the equation

$$\alpha = \frac{A}{kT} \quad \frac{\omega^2 \tau(T)}{1+\omega^2 [\tau(T)]^2}$$

Fig. 4.23 shows the plot of relaxation time τ versus 1/T at 25 MHz for various doses. This plot shows that the activation energy varies from 0.025 eV to 0.031 eV.

γ-rays are likely to produce, displacement of single atoms, or produce colour centres. But no obvious change in colour was noticed.

Since the peak attenuation decreased and increased with increasing doses and also the activation energies changed, nothing very conclusive can be decided.

CHAPTER FIVE

PHONON-PHONON ATTENUATION

The experimental results given in Chapters Three and Four show that the attenuation curves for the undoped and doped BGO crystals can be regarded as consisting of two components, one due to phonon-phonon attenuation and the second due to the relaxation effects. The attenuation due to relaxation effects has been discussed in previous chapters. The first component is present for all the samples and the magnitude of this attenuation would give a correction factor for the attenuation peaks . To calculate this factor, the attenuation curves which did not show any peaks have been used. A brief review of various theories for phonon-phonon interactions is given in the first section.

5.1 Introduction

A given ultrasonic wave interacts with the thermal phonons due to the anharmonic nature of interatomic forces in dielectrics. The thermal phonons also undergo interactions and have a mean free path.

Two regions of temperature are generally considered. In the low temperature region, $T << T_D$, where T_D is the Debye temperature; the ultrasonic wave passing through the crystal has a wavelength, λ, smaller than the mean free path, and is defined by the condition $\omega \tau_{th} > 1$, where ω is the sound frequency, and τ_{th} the thermal phonon relaxation time.

As the temperature is increased, the collision time between thermal phonons decreases and the mean free path becomes smaller than the impressed sound wavelength given by $\omega \tau_{th} < 1$.

In this second region, the sound wave causes a disturbance in the distribution of phonons. The increase in entropy required to restore these phonons to thermal equilibrium leads to an absorption of acoustical energy. Different theories explaining interactions in these two regions are given briefly in the next section.

5.2 Low temperature region $\omega\tau > 1$

In this region, the sound wave is considered to interact with individual phonon modes The mechanisms involved were first discussed by Landau, Rumer, Slominskii (1937). They considered three phonon collisions, in which one thermal phonon collides with an incoming phonon to generate a third phonon.

Since measurements were made only for the transverse mode, (110, 001), the possible interactions only for the transverse ultrasonic waves are discussed.

(1) For an isotropic, non-dispersive medium, the dominant process is generally assumed to be a non-collinear interaction

$$T + L_1 \rightleftarrows L_2 \qquad (5.2.1)$$

known as the Landau-Rumer process.

Here T and L represent transverse and longitudinal modes and subscripts 1 and 2 refer to the thermal phonons involved in the interactions. Notations are as used by Simpson (1974). Landau and Rumer derived

$$\alpha_T = \left(\frac{\pi^3 \hbar F_1^2}{60 \rho^3 \overline{s}^{10}} \right) \omega \left[\frac{kT}{\hbar} \right]^4 \qquad (5.2.2)$$

for shear waves.

$\overline{F}_1$ and $\overline{s}'$ are complicated averages of third order elastic constants and phonon phase velocities. ρ is the density of the material.

(2) Collinear processes. Interactions like

$$T + T_1 \rightleftarrows T_2 \qquad (5.2.3)$$

are also possible but are less dominant.

Dispersion and anisotropy prevent collinear interactions with thermal phonons. Simpson (1974) explains that for transverse acoustic modes propagating along high symmetry directions, pure collinear interactions are forbidden, since the anharmonic coupling between three phonons vanishes. But certain shear modes have been found to have an attenuation dependence of T^n with $n > 4$ (e.g. quartz and Al_2O_3). This higher temperature dependence was explained by Simon (1963) and Maris (1964). They pointed out that the energy time uncertainty principle due to the thermal phonons having finite life times could relax the conservation of energy condition. If τ_{th} is the thermal phonon life time, the energy uncertainty is $\hbar / \tau_{th}$.

$$\therefore \qquad \omega + \omega' = \omega'' + \hbar / \tau_{th}$$

ω, ω' and ω'' are the angular frequencies for the phonons involved. This allows the process (5.2.3) to take place and the attenuation is given by

$$\alpha_T = \alpha_{LR} \text{ (Landau-Rumer)} + \tau \text{ dependent term (smaller than } \alpha_{LR})$$

Simpson has performed detailed calculations for transverse waves propogating along high symmetry directions in a number of cubic crystals. He has taken full account of anisotropy and finite thermal phonon life times to determine when non-energy conserving interactions are of importance. He has shown that in many cases the main contribution to absorption comes from interaction with slow transverse thermal phonons; that are non-energy conserving, and near collinear. In the case of strong anisotropy, interactions are energy conserving interactions. The former processes are shown to give a temperature dependence of T^n where $n > 4$ and a less than linear frequency dependence; and for the latter processes the presence of anisotropy and finite thermal phonon lifetimes have been used to explain experimentaly-observed value of $n < 4$ and a frequency dependence greater than linear.

5.3 High temperature region $\omega\tau < 1$

When $\omega\tau < 1$, direct interaction of sound wave with phonons cannot be followed and is treated macroscopically.

According to Akhieser (1939) the presence of sound wave causes a change in the frequency of the Debye phonons. The thermal phonon frequency for phonons of different polarisation and propagation is changed by different values. The perturbed system comes to equilibrium by collisions among phonons in different modes and the resulting increase in entropy gives rise to the sound absorption.

Akhieser calculated the absorption coefficient to be as

$$\alpha = \beta^2 \left(\frac{3}{C}\right)^2 \frac{KT}{\rho v^5} \omega^2$$

where β - bulk modulus

ρ - density of the material

v - the compressional wave velocity

K - the thermal conductivity

C - the specific heat/cc

At high temperatures, $K \propto \frac{1}{T}$ so α is independent of temperature.

Woodruff and Ehrenreich (1961) obtained similar expression for α. By considering three systems; the driving sound wave, the dissipating system (taken to be the phonon gas occupying the dielectric) and external heat bath, the attenuation of the acoustic wave is then regarded as being due to the transfer of energy from the wave to the phonon gas which in turn transfers an equal amount to the heat bath. They calculated

$$\alpha = c_v T \gamma_{av}^2 \omega^2 \tau_{th} / 3\rho v^3 \qquad (5.2.4)$$

$$K = \frac{1}{3} c_v v^2 \tau$$

then $$\alpha = K T \gamma_{av}^2 \omega^2 / \rho v^5$$

At higher temperatures $K \propto \frac{1}{T}$ so α is independent of temperature.

Bommel and Dransfeld (1965) modified the above expression. They divided all branches of phonons into two groups, one containing branches that suffer a large positive temperature change and the rest belonging to the other group. When a compressional wave propagates through the crystal, a time-dependent temperature difference is produced between the two groups of phonons. Heat exchange between them leads to an increase of entropy and hence absorption of sound. The attenuation coefficient is given by

$$\alpha = \frac{C_v T \gamma_{av}^2}{4\rho v^3} \qquad \frac{\omega^2 \tau}{1+\omega^2 \tau^2}$$

γ_{av} is the average Gruneisen constant. C_v is the specific heat/cc.

Mason and Batemann (1964) have also obtained an expression relating the attenuation to the known third order elastic constant as

$$\alpha = \frac{\Delta C}{2\rho v^3} \left(\frac{\omega^2 \tau}{1+\omega^2 \tau^2} \right)$$

ΔC is the instantaneous increase in the elastic modulus caused by separation of the phonon modes.

5.4 Experimental results

Figure 4.11 shows the results for doped BGO crystals at 90 MHz from 4.2 to 250 K. This figure shows that one component of attenuation due to phonon-phonon attenuation is present for all the samples and its magnitude depends on the dopant present.

The attenuation curves without any relaxation peaks consist of three regions, first the low temperature region from 4.2 to about 30 K in which the attenuation is very small.

In the second region, from 30 K to about 100 K, the attenuation increases with temperature and in the third region above 100 K, the attenuation was again independent of temperature.

Table 5.1 gives the attenuation values at 100 K for various samples and frequencies.

TABLE 5.1 Attenuation as a function of dopant and frequency at 100 K

Crystal	Dopant	Temperature K	Frequency MHz	Attenuation α (dB cm^{-1})
BGO	Cr	100	25	1.0
			45	1.4
			90	1.9
	Zn	100	25	0.4
			45	0.72
	Al	100	30	0.6
			90	0.7
	Pb	100	45	0.3
			90	0.5
	P+ Ga	100	25	0.3
			45	0.6
			90	1.3
	Cr + Ga	100	45	0.3
			90	0.45
			190	0.8

5.4.1 Analysis of experimental results

In the low temperature region, if $\omega\tau_{th}$ is greater than unity, the most probable interaction is the Landau Rumer interaction given by Eq. (5.2.1). From Eq. (5.2.2), the attenuation for transverse waves can be expressed in the form of a power law given by

$$\alpha = A_1 \quad \omega T^n$$

Here A_1 is some constant, T the absolute temperature and n the power index.

A log-log plot of attenuation versus temperature would give the value of n. According to Eq. (5.2.2), the attenuation should show approximately T^4 dependence and should increase linearly with frequency.

But this effect is usually observable only at much higher frequencies and lower temperatures than used in this work.

Figure 5.1 shows the log-log plot of attenuation versus temperature from 30 to 100 K for various doped samples and frequencies. This plot shows that the attenuation depends strongly on the dopant present (dopant concentration also varies from one sample to another). The frequency dependence lies between linear and quadratic. The slope of these graphs gives approximately a $T^{3.5}$

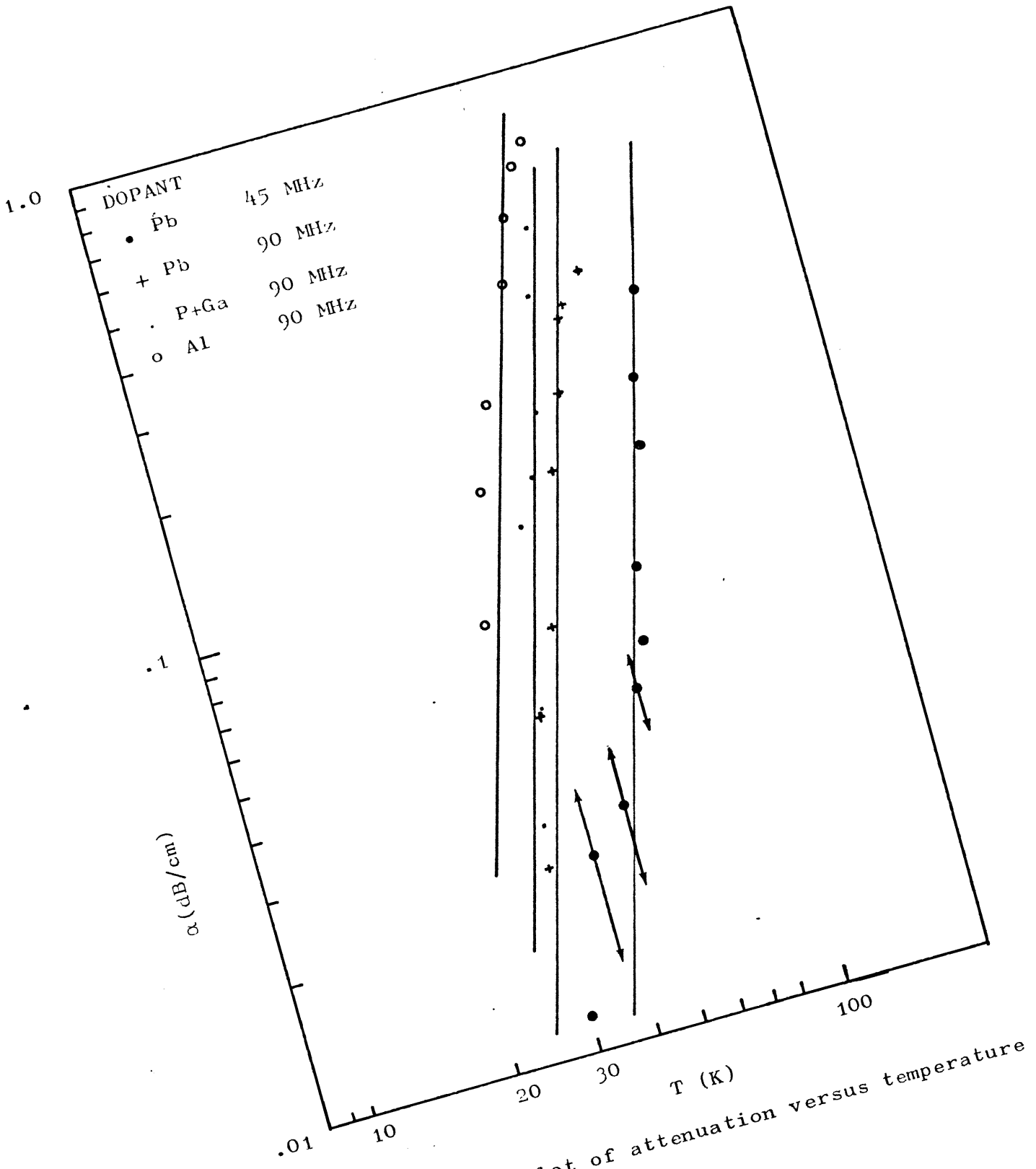

FIG. 5.1 Log-Log plot of attenuation versus temperature

dependence. Since the value of attenuation at Helium temperature is subtracted from the data at all temperatures, the additive temperature independent contributions to the attenuation are eliminated.

According to Silverman (1968), the presence of imperfections in a crystal should reduce the thermal phonon life time τ from its value in a perfect crystal. The reduction in life time affects the ultrasonic attenuation in the low and high temperature regions in opposite ways. At high temperatures, a decrease in life time results in a decrease in attenuation, due to a rapid relaxation towards the equilibrium phonon distribution. At low temperatures, a decrease in life time increases the attenuation by relaxing the energy conservation restriction. He suggests that a cross over point should be observed for pure and impure attenuation curves - about $\omega\tau \simeq 1$. But no such cross over-point was observed in our measurements. This confirms that above 30 K, $\omega\tau_{th} < 1$ for these crystals.

In the region where $\omega\tau_{th} < 1$, the attenuation is given by Eq. (5.3.1), to be

$$\alpha = \frac{K T \gamma_{av}^2 \omega^2}{\rho v^5}$$

i.e., the attenuation should be proportional to ω^2 and the thermal conductivity, K.

If the temperature T is much larger than the Debye temperature of the material, K is usually $\propto 1/T$ and the attenuation becomes independent of temperature. But for BGO the Debye temperature is $\simeq$ 240 K, therefore we have not reached this limit. Since no values for the thermal conductivity are available in this temperature range, therefore no satisfactory explanation can be given for the attenuation observed in these crystals. Further experiments over a wider frequency range and on crystals doped with different concentration may clarify this.

CHAPTER SIX

DISCUSSION AND CONCLUSION

6.1 Introduction

Experiments employed for studying the propagation of ultrasonic waves in BGO-BSO have been described in the previous chapters. Data was obtained for attenuation in undoped, doped, annealed and γ-irradiated crystals. Two transverse and two longitudinal modes were studied for undoped BGO. For all other cases, results were obtained for only transverse $T_1(110,001)$ mode.

As shown in Chapter Three, large attenuation peaks were observed for certain modes in undoped crystals in the temperature range from 30 to 60 K. All these peaks were found to be typical relaxation peaks as discussed in Section 3.5. As seen in Section 3.5, the same relaxation process seems to be responsible for the attenuation peaks observed for different modes. Detailed analysis of the peaks indicates that these attenuation peaks may be due to relaxation of point defects.

Results on doped BGO crystals given in Chapter Four show that dopants have a marked effect on the ultrasonic attenuation.

Vacuum and oxygen annealing had no effect on the ultrasonic attenuation in undoped crystals. But, for Cr-doped crystals vacuum annealing reduced the peak attenuation, while oxygen annealing restored it to its original value. The activation energy of the process was unchanged and only the number of defects changed.

Effects of γ-irradiation on the ultrasonic attenuation were not very conclusive. As described in Chapter Four, an optical absorption shoulder is observed below the band gap for undoped crystals. Hou et al (1972) and Rehwald (1976), after studying the optical absorption and ultrasonic attenuation in Al, Ga-doped BSO crystals, have suggested a correlation between these two effects. Our attenuation measurements on doped BGO crystals given in Fig. 4.11 and the optical absorption measurements made by Oberschmid (1978) given in Fig. 4.13, also suggest a correlation between the attenuation peak and the optical absorption shoulder below the band gap. Therefore it seems probable that the same defect may be responsible for both these effects.

Therefore the problem is to find the possible defects present in the undoped crystals of BGO/BSO and the mechanism by which dopants effect the defects. The properties of BGO and BSO are very similar and any models should relate to both crystals.

The undoped nominally pure crystals of BGO/BSO show the attenuation peaks and are coloured (pale yellow or brown). Since Brice (1977) has reported that BSO crystals typically contain only two to ten ppm of impurities irrespective of the content in the melts; this suggests that the large attenuation peak is an intrinsic property of the material.

In many insulating crystals, relaxation effects have been observed which are attributed to the redistribution of bound electrons among two or more equivalent sites. Such effects are analogous to point defects relaxation, but the activated process is the jump of an electron rather than of an ion. For an electronic relaxation, the change in velocity would be negligible but an appreciable change in

velocity was observed for BSO (Hardy, 1976); for the transverse T_1(110, 001) mode, in the temperature range where the attenuation peak occurs. This suggests a mechanical relaxation rather than an electronic relaxation.

A number of point defects are possible, such as the simple vacancy (v), substitutionals (s), or interstitials (i), or the composite defects such as (i-i) or (s-v) pairs. The concentration of defects can be approximated from various available measurements.

Dopants can change the number of defects in a number of ways.

(a) By changing the number of defects.

(b) If the dopant atom is not isovalent to the atom it replaces, it may change the defects by changing the electron population.

(c) The dopants may enter as interstitials next to the defects and change the symmetry of the defect.

Due to the complex structure of this material, it is difficult to say definitely what sites are occupied by dopants; however various available measurements are used to decide the possible site occupied.

6.2 Experimental Evidence

6.2.1 Ultrasonic measurements

As described in Chapter Three, the temperature and frequency dependence of attenuation lead to the conclusion that the attenuation peaks are due to a relaxation attenuation of the usual form

$$\alpha = \frac{A}{T} \cdot \frac{\omega^2\tau}{1+\omega^2\tau^2} \qquad (6.1)$$

where $\tau = \tau_\infty \exp(Q/kT)$. The peak is a single Debye relaxation with a well-defined activation energy Q and an attempt frequency $1/\tau_\infty$ approximately equal to a lattice phonon frequency. As discussed in Section 3.5, the selection rules for anelastic relaxation show that the peak is due to a relaxation of the elastic constant c_{44} only, which implies that the defect causing the attenuation has trigonal symmetry.

Various parameters extracted from the experimental data are given in Table 6.1.

The values of the product $c_0|\lambda_1 - \lambda_2|^2$ given in the table are for the samples used in this work, but these figures should give an order of magnitude for all nominally pure and stochiometric crystals of BGO/BSO, because of the following reasons:

(i) All measured samples of undoped BGO/BSO (Spencer; 1972, Rehwald, 1975) show similar attenuation peaks.

(ii) Measurements of the acoustic surface wave propagation loss in vacuum on BGO have been made by Slobodnik et al (1972). Temperature dependence measurements show loss peaks in the vicinity of 50-100 K

(iii) All undoped samples have similar colour and show an optical absorption shoulder below the band gap.

6.2.2 Correlation with optical absorption

If the concentration of defects C_0 is known, the absolute value of $|\lambda_1 - \lambda_2|$ can be obtained and this would provide the degree of ellipicity of the distortion. As mentioned in Section 3.2, if the lattice parameter change per unit concentration of defects is known, an additional expression involving the sum $(\lambda_1 + \lambda_2 + \lambda_3)$ can be obtained for calculating $|\lambda_1 - \lambda_2|$ as

$$\frac{1}{C_0} \frac{\Delta a}{a} = \frac{1}{3} (\lambda_1 + \lambda_2 + \lambda_3) \qquad (6.2)$$

where 'a' is the lattice parameter.

Since, as concluded in Chapter Three, the defects responsible for these large attenuation peaks must have trigonal symmetry and for a trigonal defect $\lambda_2 = \lambda_3$, therefore Equation 6.2 becomes

$$\frac{1}{C_0} \frac{\Delta a}{a} = \frac{1}{3} (\lambda_1 + 2\lambda_2) \qquad (6.3)$$

The change in lattice parameter due to defects is calculated from the data for optical absorption in BGO crystals.

As discussed in the first Chapter, facets are formed during the growth of BGO and BSO which are darker yellow in colour and show an increased 'a'. Oberschmid and Grabmeier (1978) have measured a small difference in lattice constant

$$\frac{\Delta a}{a} \simeq (1. \pm 0.3) \times 10^{-4} \qquad \text{for BGO}$$

in the facets (core) region compared with the rest of the crystal. Similar increase in lattice constant

TABLE 6.1 Activation energy, attempt frequency, and the product of $C_0|\lambda_1-\lambda_2|^2$

Crystal	Activation energy eV	Attempt frequency $1/\tau_\infty$ 10^{12}Hz	$C_0\|\lambda_1-\lambda_2\|^2$ 10^{-7}
BGO	0.043± .001	5± 1	4± 1
BSO	0.026± .002	2± .5	6± 1
BGO+Zn	0.036± .002	1± .5	3± 1
BGO+Cr	0.035± .001	.6± .2	4± 1

$$\frac{\Delta a}{a} \quad (0.5 \pm 0.1) \times 10^{-4}$$

in the facets was observed by Brice (1977) for BSO.

Oberschmid and Grabmeier also report that a higher absorption shoulder was observed in the facet material compared with the rest of the corresponding crystal as shown in Fig. 4.13.

If we assume that the increase in the lattice constant, $\frac{\Delta a}{a}$, in the core is entirely due to the absorbing centres, then an increase in the optical absorption by a factor of ~ 0.63 for BGO corresponds to the change

$$\frac{\Delta a}{a} \quad \text{of} \quad (1 \pm 0.3)10^{-4}$$

Therefore we can calculate the appropriate change in the lattice parameter due to all the defects present in the crystal. Using Equation 6.3,

$$(\frac{\Delta a}{a}) = \frac{C_0}{3} (\lambda_1 + 2\lambda_2) \tag{6.4}$$

From the calculated values of $C_0|\lambda_1 - \lambda_2|^2$ and Equation 6.4, λ_1 and λ_2 can be obtained.

6.2.3 λ-tensor

From Equation 3.2.11,

$$(\lambda_1 - \lambda_2) = \pm\sqrt{\frac{B\alpha_M}{C_0}} \tag{6.5}$$

Here B is a constant and α_M the peak attenuation. And from Equation 6.4,

$$\lambda_1 + 2\lambda_2 = \frac{3}{C_0}\left(\frac{\Delta a}{a}\right) \quad . \tag{6.6}$$

So λ_1 and λ_2 can be given by

$$\lambda_1 = \frac{1}{C_0}\left(\frac{\Delta a}{a}\right) \pm \frac{2}{3}\sqrt{\frac{B\alpha_M}{C_0}}$$

and $$\lambda_2 = \frac{1}{C_0}\left(\frac{\Delta a}{a}\right) \mp \frac{1}{3}\sqrt{\frac{B\alpha_M}{C_0}}$$

These equations provide two values of λ_1 and λ_2 depending on whether λ_1 is $\gtrless \lambda_2$.

Using these values, graphs were plotted from λ_1 and λ_2, versus C_0, as shown in Figs. 6.1 and 6.2. These graphs show that the difference $(\lambda_1 - \lambda_2)$ is appreciable for C_0 from (0.005) to (0.05) and then decreases rapidly.

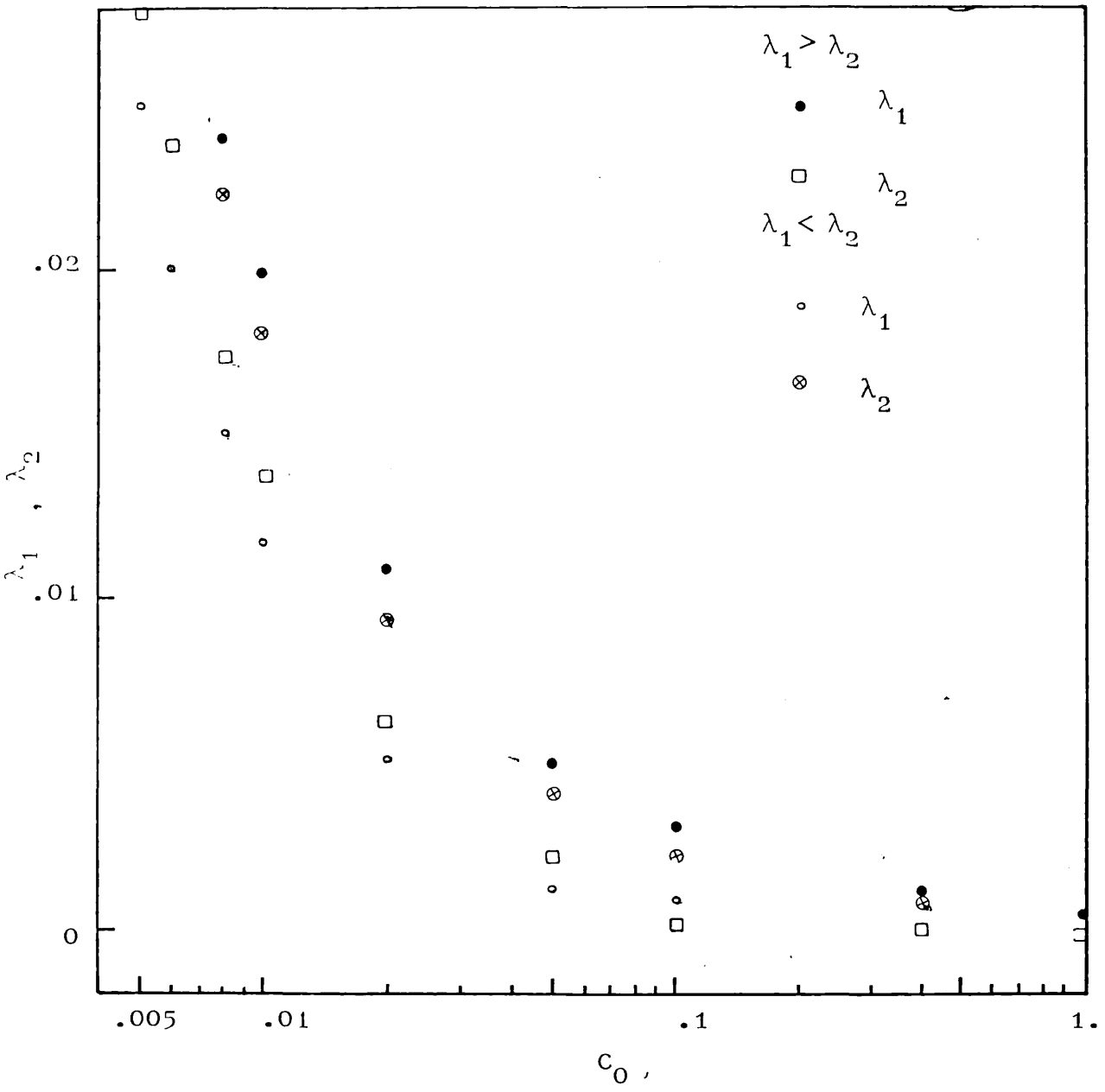

FIG. 6.1 Plot of defect concentration versus λ for BGO

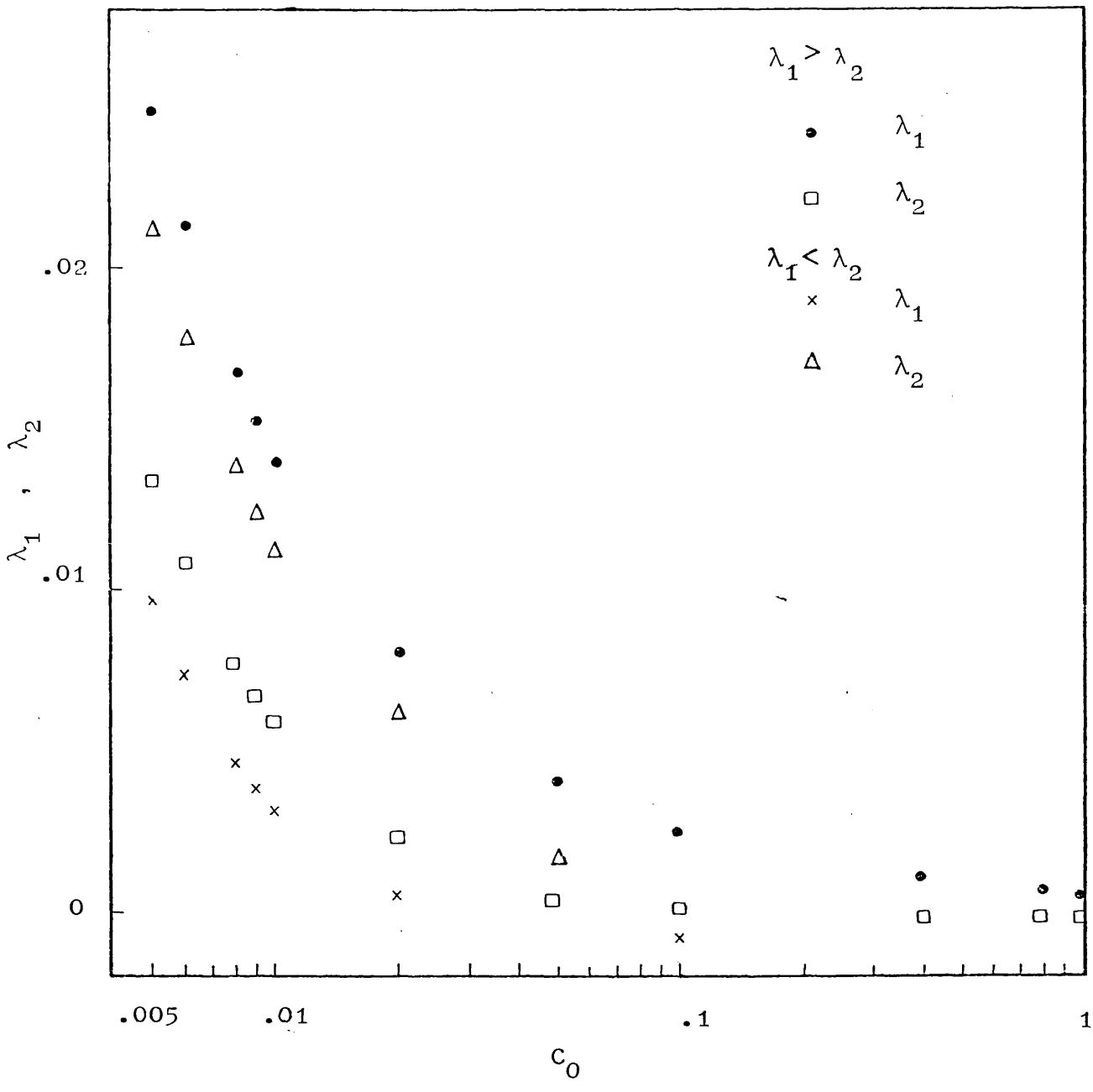

FIG. 6.2 Plot of defect concentration versus λ for BSO

6.2.4 Range of λ

As described in Section 1.2, Craig et al (1975) have shown that the body centered cubic structure with formula $Bi_{12}MO_{20}$ can accommodate a variety of different M atoms. If the lattice constants for these crystals are plotted versus the ionic radii given in Table 1.1, it can be seen from Graph 6.3 that the lattice constant increases linearly with the ionic radius.

A comparison with close-packing shown by the dotted line suggests a relatively loose structure.

Crystals of BMO with M being a Bi atom, have been prepared but are found to be unstable at room temperature. To obtain an order of magnitude of λ tensor for a Bi substitution on Ge sites, let us assume that all Ge atoms in BGO are replaced by Bi atoms. From Equation 3.12 for a substitutional atom, the increase in the lattice constant $\frac{\Delta a}{a}$ is

$$\frac{\Delta a}{a} = \frac{1}{3}(3\lambda_1 = 3\lambda_2 = 3\lambda_3)$$

From the graph in Fig. 6.3, we can calculate approximate value for λ_1. This gives

$\lambda \approx 0.01$ **For Bi substitution on Ge sites.**
$\lambda \approx -0.004$ **For Si on Ge sites.**
$\lambda \approx 0.004$ **For Ge on Si sites.**

and for vacancies on Ge or Si sites, λ would be (~ -0.004).

Various figures have been given by different workers for the number of defects in BGO/BSO.

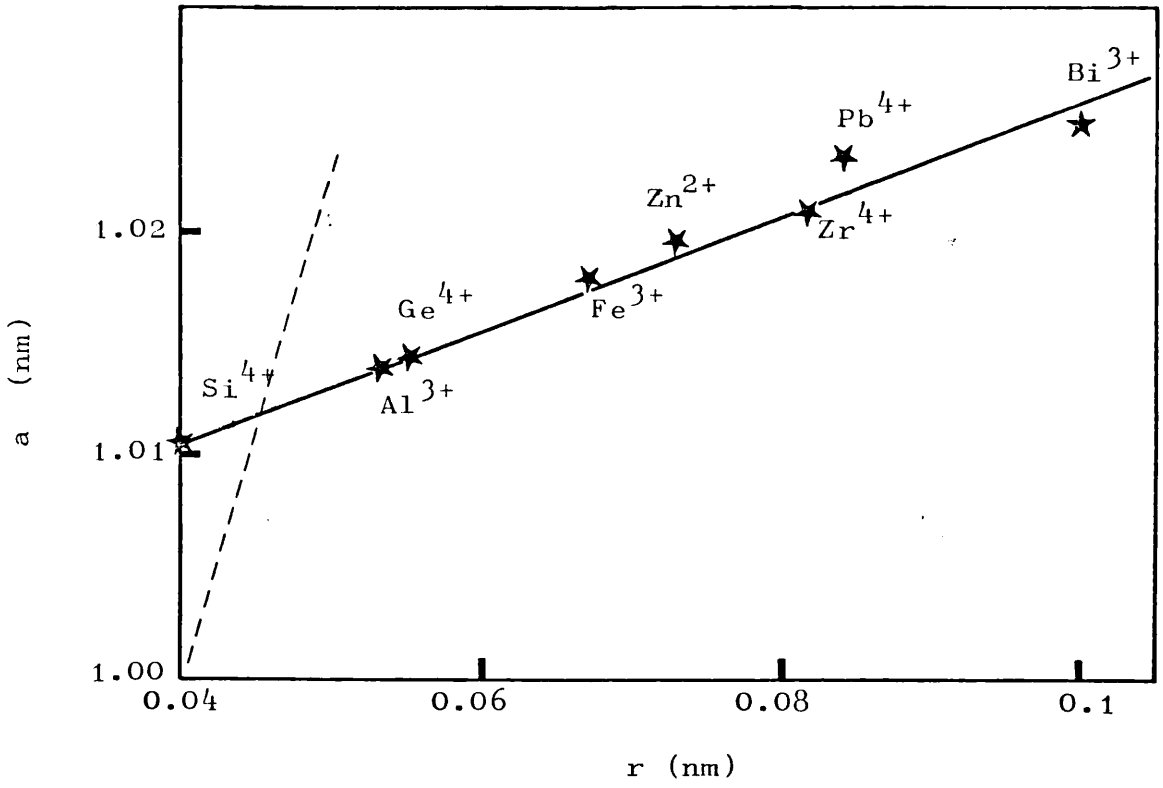

FIG. 6.3 Lattice constant versus ionic radius

(i) Brice (1977) has shown that these crystals typically contain impurities up to about 10 ppm (i.e. 1×10^{-5}). If these impurities are the cause of attenuation peaks and the optical absorption, λ would have to be enormously large.

(ii) Abraham et al (1967) have shown by X-ray analysis that Si or Ge vacancies of the order of (0.13) can be present in these crystals. But for vacancies λ would have (-ve) value.

(iii) Oberschmid (1979) has mentioned that Bi substituting for Ge or Si is always less than (0.035).

(iv) Tanguay (1976) also reports that the number of defects is less than (0.01).

(v) As seen in Chapter Four, a sample of BGO doped with Ga (0.004) showed no attenuation peak and the optical absorption shoulder within the band gap was also removed. If this dopant concentration corresponds to the number of defects present in the undoped crystal, this would give C_0 to be $\tilde{\sim}$ (0.004).

Rehwald (1976) also found that doping with Ga (0.002) reduced the attenuation peak to about (1/3) of its undoped value. Therefore it indicates that the defect concentration should be (> 0.002).

Therefore, considering the defect concentration of the order of

$$C_o \sim 0.005$$

λ would be positive and have reasonable values of the order of

$$\lambda \sim (+ 0.01 \text{ to } 0.02).$$

This value corresponds to the λ value calculated for a substitution on Ge or Si sites. But this conclusion depends on defect being the only cause of expansions on facets.

The activation energies obtained from our results are given in Table 6.1. Rehwald (1975) obtained values for activation energies for BGO and BSO to be 0.045 and 0.033, which agree with values obtained in this work. Spencer (1972) obtained a much lower value of 0.005 eV.

6.3 Other available measurements

To help identify the defect, various available measurements for BGO, BSO are considered.

(a) From ESR measurements in BSO Tanguay (1976) concluded that the number of unpaired spins is less than 5 ppm in undoped pair BSO (i.e., with absorbing centres). This indicates that the number of unpaired electrons is very small in these crystals.

(b) As described in the first Chapter, the dark conductivity is p-type in these crystals, but photoconductivity measurements show that the electrons dominate the photocurrent in undoped crystals.

(c) Abraham et al (1967, 1979) has reported from the X-ray diffraction studies on BGO and BSO that the occupancy factor of the Ge sites is 0.87 ± .02 and 0.87 ± 0.08 for Si.

But, Brice, Hill (1974) and Wilkes (1978) in reports on the growth of BSO crystals show that the Bismuth to Silicon ratio in the crystal varies from 11.77 : 1 to 12.05 : 1, as the ratio in the melt is varied from 10 : 1 to 15 : 1, as shown in Table 6.2 and Graph given in Fig. 6.4.

(d) Rehwald (1975) also reports that the dielectric loss measurements show no temperature dependence. Therefore there is no electric dipole associated with the elastic dipole.

Taking all these measurements into account, the possible defect centres are discussed below.

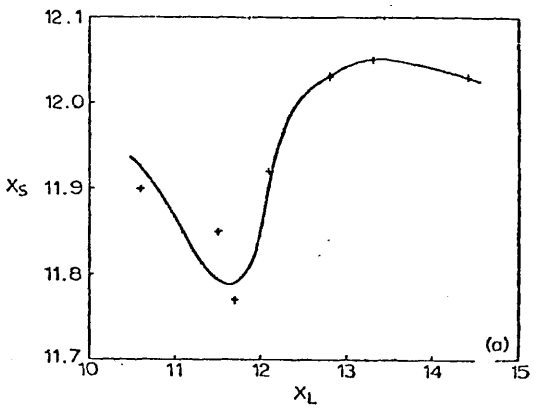

FIG. 6.4 Relation of bismuth content in the melt and the crystal (Brice, 1974)

TABLE 6.2 Lattice constant for crystals grown from different melt compositions (Brice, 1974)

Compositions		Lattice constant
Melt (x_L)	Crystal (x_S)	$(a_0 - 10.1000) \times 10^4$
10.6	11.90 ± 0.07	33 ± 3*
11.5	11.85 ± 0.03	30 ± 3
11.7	11.77 ± 0.03	30 ± 1
12.1	11.92 ± 0.04	31 ± 2
12.8	12.03 ± 0.06	32 ± 4
13.3	12.05 ± 0.10	33 ± 4
14.4	12.03 ± 0.03	32 ± 1

*The lattice constant for crystal grown from melt x_L = 10.6 is 10.1033 ± 0.0003 Å.

6.4 Possible defect centre

As discussed before the defects responsible for the ultrasonic attenuation peaks and optical absorption shoulder is an intrinsic defect. This defect must have trigonal symmetry. If the defect is trigonal, it must lie on <111> axis through the Si site as shown in Fig. 6.5. The site symmetries of various atoms discussed in Section 1.2 suggest that the defects must be associated with GeO_4 or SiO_4 tetrahedra. The various possibilities are:

6.4.1 Ge or Si vacancy (v)

A simple Ge or Si vacancy cannot give rise to anelasticity since its site symmetry is cubic 23 and $\lambda_1 = \lambda_2 = \lambda_3$. However, as assumed by Scholtz and Seegar (1963) for vacancies in germanium, if the bonds which are broken to form a vacancy are reformed between pairs of atoms nearest neighbours to the vacancy, the defect formed may have lower than cubic symmetry and give rise to relaxation. This is really a manifestation of Jahn Teller effect (Watkins, 1972).

6.4.2 Oxygen-vacancy

An oxygen vacancy on O(3) or O(2) site forming the tetrahedron would have the trigonal symmetry. The oxygen will have four different sites on the tetrahedron surrounding the silicon or germanium site.

6.4.3 Divacancy (v-v)

In stochiometric compounds, it is possible to have an equal number of vacancies on the cation and anion lattices for charge neutrality. Therefore if there are Ge or Si vacancies there may be oxygen vacancies associated with these and form divacancies as $[GeO]^{--}$ or $[SiO]^{--}$.

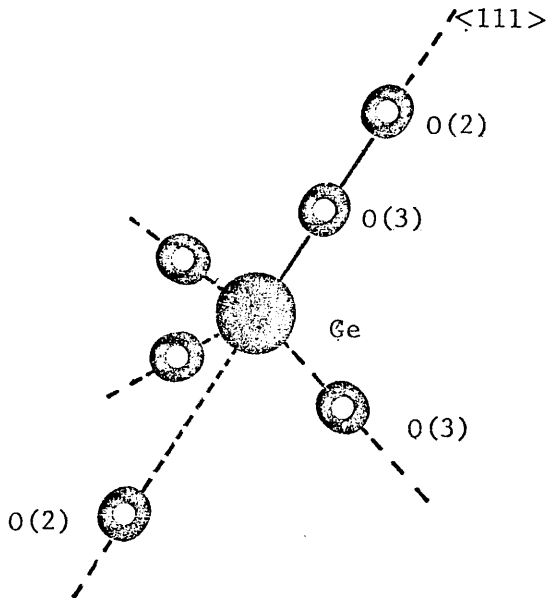

FIG. 6.5 Diagram of a trigonal defect

6.4.4 Vacancy substitutional pair (v-s)

If certain ions of a lower valence substitute for Ge or Si, the presence of a vacancy on an oxygen site is required for charge neutrality. Due to strong coulomb attraction, it can be expected that the substituted ion and vacancy are located on adjacent sites. Thus the vacancy can be on one of the four tetrahedron sites and the defect so formed is trigonal.

6.4.5 Substitutional-interstitial pair (s-i)

In certain insulators and semiconductors, defects consisting of an interstitial atom bound to a substitutional impurity have been observed. Therefore a defect consisting of an atom on Ge or Si site associated with an interstitial oxygen may form the required defect.

Some of these defects have been considered by other workers. From Abraham's X-ray data, Hou et al (1972) assume that Ge or Si vacancies of the order of $10^{19}/cm^3$ can exist in BGO, BSO and for charge neutrality oxygen vacancies are needed. Therefore a Ge, Si and oxygen divacancy complex is regarded as the possible absorption centre. They have explained the optical absorption shoulder by electronic transitions from this Ge, Si vacancy complex level.

Rehwald has assumed that if this level is degenerate and splits under the external strain, it can cause the ultrasonic attenuation observed.

Hou et al (1972) and Rehwald (1976) have expressed the opinion that various dopants shift the Fermi level thereby effecting the optical and ultrasonic attenuation. Al doping is assumed to occupy Si sites and lower the Fermi level by creating acceptor levels. If has been

indicated that addition of P brings the Fermi level back to the original position and restores the absorption shoulder. But there are a few inconsistencies. Firstly, as mentioned before, Brice (1974) reports that when crystals are grown from a stochiometric melt (i.e. 6 Bi_2O_3 : 1 GeO_2), the Bi : Si ratio in the crystal is always less than 12 : 1. This indicates a Bi deficiency in the crystal.

A second puzzling feature is the fact that a (P + Ga)-doped BGO sample used in this work did not show any attenuation peak. This crystal was nearly transparent and Oberschmid (1977) found these samples to be n-type. But the optical absorption within the band gap was reduced compared to that for the undoped crystals as in Fig. 4.13. This is contrary to what should have been expected, according to the explanation given by Hqu et al (1972).

A second type of centre (s-v) pair is suggested by Oberschmid et al (1979). They assume a Bi atom on Ge/Si site, because of the large lattice constant observed in the facets, and a hole on the surrounding oxygen tetrahedra sites associated with the $Bi^{3+}_{Ge,Si}$ centre.

They explain the dopant bleaching of the BGO, BSO crystals by the following mechanism:

(a) Deep acceptor levels of $Al_{Ge,Si}$ or $Ga_{Ge,Si}$ site may reduce the absorption centre like

$$Bi^{3+}_{Ge,Si} + h \rightarrow (Bi^{4+}_{Ge,Si}) + h + e$$

(b) Electrons from donor levels of P_{Ge} or P_{Bi} site may compensate the hole of the absorption centre like

$$Bi^{3+}_{Ge,Si} + h + e \rightarrow Bi^{3+}_{Ge,Si}$$

These effects are assumed to shift the optical transition energy levels and cause the absorption shoulder to vanish.

This defect would have the right symmetry and would give a (+ve) λ value. But, some workers argue that Bi^{3+} ion being too large and asymmetric cannot occupy a position with site symmetries 23. Levin and Roth (1964) have commented that metastable bcc phases are formed if oxides involving large ions such as Cd^{2+}, Ce^{4+} are added to Bi_2O_3. Presumably these structures involve the large cations occupying the tetrahedral sites thereby causing distortions. Therefore it seems less likely that Bi^{3+} is substituting for Ge/Si.

Craig and Stephenson (1975) have studied the structure of two compounds $Bi_{25}FeO_{40}$ and $Bi_{38}ZnO_{60}$ involving Bi_2O_3. These crystals are also body-centred cubic. They found that for both these crystals the electron concentration on the tetrahedral sites was much higher than it should be if these sites were fully occupied by Zn in the case of $Bi_{38}ZnO_{60}$ and Fe in the case of $Bi_{25}FeO_{40}$. They have explained this higher electron population by assuming that there must be some Bismuth substitution on the tetrahedral sites. They have assumed that $\gamma - Bi_2O_3$ structure contains some Bi^{5+} ions in addition to Bi^{3+}, and these smaller Bi^{5+} ions can occupy the tetrahedral sites.

Brice et al (1977) have also assumed the presence of some Bi^{5+} in $\gamma - Bi_2O_3$ in order to explain the larger lattice constant observed in the facets.

Therefore if Bi^{5+} ions can be present in γ- Bi_2O_3, these ions may occupy some of Ge/Si sites in BGO/BSO crystals. The substitution of Bi^{5+} on Ge/Si sites would give a (+) λ value and the increased lattice constant observed in the facets. If the pentavalent Bi^{5+} ion replaces Si^{4+} or Ge^{4+} ions in the crystal, the mode of charge compensation is the introduction of extra (O^{--}) ions.

The relaxation of (O^{--}) ions can therefore possibly give rise to the effects observed in these crystals. The addition of Al, Ga, may reduce the content of Bi^{5+} ions present in BGO/BSO, thus removing the attenuation peaks and the optical absorption shoulder below the band gap.

Wardzynskii et al (1979) have mentioned (ESR measurements) that Cr added as a dopant to BGO occupies tetrahedral sites. The presence of a Cr^{3+} on a tetrahedral site would cause a Bi^{5+} ion to occupy the neighbouring tetrahedral site for charge neutrality, thus increasing the Bi^{5+} content. This would explain the larger ultrasonic attenuation and optical absorption shoulder observed in Cr-doped BGO cyrstals. Due to the complex structure of these crystals, it is difficult to say exactly what is causing the effects observed in this material, but the presence of Bi^{5+} ions may be the possible cause.

It was assumed in section 6.2.2 that the larger optical absorption and a larger lattice constant in facets is due to the increased number of defects, and would give a corresponding increase in attenuation peaks; therefore it would be required to do some measurements on attenuation in the facet regions, to confirm this assumption.

It would also be intersting to make some attenuation measurements in crystals of $Bi_{25}FeO_{40}$ and $Bi_{38}ZnO_{60}$, in which the presence of Bi^{5+} ions has been indicated by Craig and Stephonson(1975).

6.5 Conclusion

The aim of this work was to try and establish the possible cause of large attenuation peaks observed at low temperatures in single crystals of BGO and BSO. Measurements of the attenuation in undoped BGO crystals, for different modes have shown that these peaks are single Debye peaks, probably due to the relaxation of point defects. Measurements suggest that the defects must have a trigonal symmetry.

Measurements made on doped BGO crystals have shown that the attenuation in these crystals depends strongly on the dopant present. A correlation has been observed between the attenuation peak and the optical absorption shoulder below the band gap, confirming the suggestion that the same defect centre is responsible for both these effects. It was hoped that this work would provide enough information to decide the possible defect centre, but due to the complicated structure of the material and certain inconsistencies with various experiments it is not possible to positively identify the defects at this time, although various suggestions are made. Further experiments in these and related materials would be required to solve this problem.

REFERENCES

Abraham SC, Jamieson PB and Bernstein JL 1967
J. Chem. Phys. 47, 4034.

Abraham SC, Bernstein JL and Svensson C 1979
J. Chem. Phys. 71, 788.

Akhieser A 1939 J. Phys. (U.S.S.R.) 1, 277.

Albova MS, Andreev AA
1977 Sov. Tech. Phys. Lett. 3(6), 219.

Aldrich RE, Hou SL, Harvill ML 1971
J. Appl. Phys. 42, 493.

Autonov VA, Arsenyev PA et al 1976
Kristall und Technik (Germany) 10, k59.

Ballman AA 1967 Journal of Crystal Growth 1,

Bernstein JL 1967 Journal of Crystal Growth 1, 45.

Berry BS, Nowick AS 1966 Physical Acoustics IIIA, 1.

Bommel H, Dransfeld K 1960 Phys. Rev. 117, 1245.

Brice JC 1977 Journal of Crystal Growth 42, 427.

Brice JC 1977 Report on Progress in Physics 40, 575.

Brice JC, Hight MJ, Hill OF, Whiffins PAC 1977
Philips Technical Review 37, 250.

Butcher KJ 1978 Ph.D. Thesis, University of London.

Clegg JB, Millet EJ 1974 Philips Tech Rev. 34, 344.

Clement JR, Quinnell EH 1952 Rev. Sci. Instru. 23, 213.

Craig DC, Stephenson NC 1975
J. of Solid State Chemistry 15, 1.

Cryotech Lake Shore Cryotronics, Sandrock RD, Eden.
N.Y.14057.

Dobbs ER, Hughes E. Lawson NS, Lea MJ, Meredith DJ
and Timms WE 1973 J. Phys. E. 6, 309.

Douglas GG, Zitter RN 1968 J. Appl. Phys. 39, 2133.

Feigelson 1976 Tanguay's Thesis.

Feinlab I, Oliver DS 1972 Apl. Opt. 11, 2752

Fynn GW, Powell WJA 1979 The Cutting and Polishing
of Electro-optic Materials (Adam, Hilger Ltd).

Grambaier 1978 Private Communication.

Gurtler 1903 Z. Anorg. Allgen. Chem. 37, 222.

Gyorgy EM, Krause JT, Lecraw RC, Merritt FR, Sturge MD
1967 Phys. Rev. 155, 218.

Hardy K 1976 M.Sc. Project Report, University of London.

Hill OF, Brice JC 1974 J. of Materials Science 9, 2652.

Hou SL, Oliver DS 1972 Appl. Phys. Letters 18, 325.

Hou SL, Lauer RB, Aldrich RE 1973 J. Appl. Phys. 44, 2652.

Huignard JP, Micheron F 1976 Appl. Phys. Letters 29, 591.

Keyes R 1967 Solid State Series 20, 37.

King PJ, Monk DJ, Oates SG 1978 J. Phys. C. 11, 1067.

Kraut EA, Tittmann BR, Graham LJ and Lim TC 1970 Appl. Phys. Lett. 17, 271.

Kröner 1958 Kontinumstheorie der Versetzungen und Eigenspannungen Springer Berlin

Landau LD, Rumer G 1937 Phys. Z. Sowjun 11, 18.

Lange J 1973 J. Phys. Rev. B8, 5999.

Lawless WN 1971 Rev. Sci. Instrum. 32, 9.

Lea MJ, Butcher KJ, Dobbs ER 1978 Proceedings of The Institute of Acoustics.

Maris HJ 1964 Phil. Mag. 9, 901.

Mason WP and Batemann 1966 J. Acoust. Soc. America 40, 1343.

Nowick AS 1967 Advan. Phys. 16, 1.

Nowick AS 1970 J. Phys. Chem. Solids 31, 1819.

Nowick AS, Berry BS 1961 IBM J. Res. Dev. 5, 297.

Nowick AS, Berry BS 1972 Anelastic Relaxation in Crystalline Solids (Academic Press).

Nowick AS, Heller WR 1963 Advan. Phys. 13, 251.

Nowick AS, Heller WR 1956 Advan. Phys. 14, 101.

Nye JF 1957 Physical Properties of Crystals (Oxford Press).

Oberschmid R 1978 German Physical Society Meeting, Freudenstadt.

Onoe M, Warner AW and Ballman AA 1967 IEEE Transactions on Sonics and Ultrasonics SU-14, 165.

Orbach R 1967 Proc. Roy. Soc. A261, 458.

Peletier M, Micheron F 1977 J. Appl. Phys. 48, 3683.

Pirc B, Zeks B and Gosar P 1966 J. Phys. Chem. Solids 27, 1219.

Rehwald W 1973 J. Appl. Phys. 44, 3017.

Rehwald W, Frick K. Lang GK, Meier E 1976 J. Appl. Phys. 47 1292.

Scott P and Jeffries C 1962 Phys. Rev. 127, 32.

Schumb W and Rittner EJ 1943 Amer. Chem. Soc. 65, 1055.

Sillen LG 1937 Arkiv. Kem. Mineral. Geol. 12A, 1.

Sillen LG and Aurvillius B 1945 Nature 155, 305.

Silverman BD 1968 Prog. Theor. Phys. 39, 245.

Simons S 1963 Proc. Phys. Soc. 82, 401.

Simpson IC 1975 J. Phys. C. 8, 399.

Slobodnik AJ and Sethares JC 1971 Physical Sciences Research Papers, No. 467.

Spranskaya and Arshakuni AA 1964 Zh. Neorg. Khim. 226.

Spencer EG, Lenzo PV and Ballman AA 1966 Appl. Phys. Lett. 9, 290.

Scholz A, Seegar A 1963 Phys. Status Solidi (Germany)

Sussmann J 1964 Phys. Condensed Matter 2, 146.

Sussmann J 1967 J. Phys. Chem. Solids 28, 1643.

Tanguay A 1977 Ph.D. Thesis Yale University.

Tanguay A 1977 J. of Crystal Growth 42, 431.

Truell R, Chick BB and Anderson G 1960 The J. of the Acoustical Society of America 32, 186.

Truell R, Elbaum C and Chick BB 1969 Ultrasonic Methods in Solid State Physics (Academic Press).

Van Vleck J 1967 J. Phys. Rev. 57, 426.

Watkins GD 1972 Radiation damage and defects in Semicoductors Conf. Series 16, 228.

Wardzynskii W, Lukasiewicz T et al 1979 Optics Communication 30, 203.

Woodruff TO, Ehrenreich H 1961 Phys. Rev. 123, 1553.

Wilkes J 1978 Private Communication.

Zelenka J 1978 Czech. J. Phys. B28, 165.

Zener C 1948 Elasticity and Aneleasticity in Metals (University of Chicago Press).

Zener C 1950 Acta Crystallogr. 3, 346.

APPENDIX 1

```
      PROGRAM RELAX(INPUT,OUTPUT,TAPE2=OUTPUT)
      DIMENSION ATTEN(200,7),ANORM(200,7),TEMP(200),FREQ(7),A(7),
     1TP(7),DATA(200,8),CODE(8),XBAR(8),STD(8),SKEW(8),CURT(8),
     2R(8,8),N(8,8),C(8,8),B(8,8),S(8,8),THETA(7),ATTFR(7)
C*****READ NO OF DATA POINTS AND NO OF DATA SETS
      READ 100,NO,M
  100 FORMAT(2I10)
      M1=M-1
      CALL FIT(ATTEN,ANORM,TEMP,FREQ,A,TP,DATA,CODE,XBAR,STD,SKEW,CURT,
     1R,N,C,B,S,NO,M,M1,THETA,ATTFR)
      STOP
      END

      SUBROUTINE FIT(ATTEN,ANORM,TEMP,FREQ,A,TP,DATA,CODE,XBAR,STD,
     1SKEW,CURT,R,N,C,B,S,NO,M,M1,THETA,ATTFR)
      DIMENSION ATTEN(NO,M1),ANORM(NO,M1),TEMP(NO),FREQ(M1),
     1A(M1),TP(M1),DATA(NO,M),CODE(M),XBAR(M),STD(M),SKEW(M),CURT(M),
     2R(M,M),N(M,M),C(M,M),B(M,M),S(M,M),THETA(M1),ATTFR(M1)
C*****READ THE NEXT THREE CARDS WHICH GIVE THE FREQUENCIES USED,
C*****APPROX A VALUES AND PEAK TEMPERATURES
      READ 101,(FREQ(I),I=1,M-1)
      READ 101,(A(I),I=1,M-1)
      READ 101,(TP(I),I=1,M-1)
  101 FORMAT(8F10.4)
C*****READTHE NO DATA SETS OF ATTEN(DB/CM) AND TEMPERATURE
      DO 1 I=1,NO
      READ 101,(ATTEN(I,J),J=1,M-1),TEMP(I)
      DATA(I,M)=1./TEMP(I)
    1 CONTINUE
      PI=3.14159265
      DO 11 I=1,M
      CODE(I)=-100.
   11 CONTINUE
C*****NORMALISE THE DATA TO (ATTEN * T **2/F * A)
      DO 19 J=1,M-1
      CALL NORM(ATTEN,ANORM,TEMP,FREQ,A,DATA,TP,NO,M,M1,J)
   19 CONTINUE
C*****DO A REGRESSION ANALYSIS ON THE M DATA SETS
      CALL MISR(NO,M,DATA,CODE,XBAR,STD,SKEW,CURT,R,N,C,B,S,IER)
      IX=1
      GO TO 21
   20 CONTINUE
      IX=2
C*****VARY A TO GIVE THE MINIMUM STANDARD DEVIATION
      DO 13 J=1,M-1
      NA=-1
      IY=0
      X=1.
   16 CONTINUE
      CALL NORM(ATTEN,ANORM,TEMP,FREQ,A,DATA,TP,NO,M,M1,J)
      CALL MISR(NO,M,DATA,CODE,XBAR,STD,SKEW,CURT,R,N,C,B,S,IER)
      SIG1=S(M,J)
      IY=IY+1
   17 A(J)=A(J)*(1.+(X*(10.**NA)))
      CALL NORM(ATTEN,ANORM,TEMP,FREQ,A,DATA,TP,NO,M,M1,J)
      CALL MISR(NO,M,DATA,CODE,XBAR,STD,SKEW,CURT,R,N,C,B,S,IER)
      SIG2=S(M,J)
      IF(SIG2.GE.SIG1) GO TO 15
      SIG1=SIG2
      GO TO 17
   15 IF(IY.GT.1) NA=NA-1
      X=-X
      IF(NA.EQ.-5) GO TO 13
      GO TO 16
   13 CONTINUE
   21 CONTINUE
```

```
C*****CALCULATE RESULTS
      DO 17 I=1,M1
      THETA(I)=B(M,I)
      TP(I)=1./C(I,M)
      ATTFR(I)=2.*PI*FREQ(I)*1.E6*EXP(-C(M,I))
   17 CONTINUE
C*****PRINT DATA
      DO 8 J=1,M1
      WRITE(2,102)FREQ(J)
  102 FORMAT(/,13H FREQUENCY = ,F10.4,3HMHZ)
      IF(IX.EQ.1) GO TO 22
      WRITE(2,108)A(J)
  108 FORMAT(/,16H BEST A VALUE = ,F10.5,13H  DB K/CM MHZ)
      GO TO 23
   22 WRITE(2,113)A(J)
  113 FORMAT(/,19H INITIAL A VALUE = ,F10.5,13H  DB K/CM MHZ)
   23 CONTINUE
      WRITE(2,109)TP(J)
  109 FORMAT(/,20H PEAK TEMPERATURE = ,F10.4,1HK)
      Z=(A(J)*FREQ(J))/(TP(J)*2.)
      WRITE(2,110)Z
  110 FORMAT(/,23H PEAK ATTENUATION = ,F10.4,5HDB/CM)
      WRITE(2,111)THETA(J),S(M,J)
  111 FORMAT(/,21H ACTIVATION ENERGY = ,E10.3,9H  +/- ,E10.3,4H  K)
      ERR=(EXP(ALOG(ATTFR(J))+(S(M,J)/TP(J)))-EXP(ALOG(ATTFR(J))-(S(M,J)
     1/TP(J))))/2.
      WRITE(2,112)ATTFR(J),ERR
  112 FORMAT(/,21H ATTEMPT FREQUENCY = ,E10.4,9H  +/- ,E10.4,4H  HZ)
      WRITE(2,114)
  114 FORMAT(//,5X,1HT,8X,3H1/T,5X,5HATTEN,5X,6HATTEN*,6X,2HNT,//)
      DO 6 I=1,NO
      XA=EXP(DATA(I,J))
      WRITE(2,103)TEMP(I),DATA(I,M),ATTEN(I,J),ANORM(I,J),XA
  103 FORMAT(5F10.5)
    8 CONTINUE
      IF(IX.EQ.1) GO TO 24
C*****PRINT REGRESSION MATRICES
      WRITE(2,104)
  104 FORMAT(/,16H GRADIENT MATRIX)
      DO 7 I=1,M
      WRITE(2,105)(B(I,J),J=1,M)
    7 CONTINUE
  105 FORMAT(8G11.4)
      WRITE(2,106)
  106 FORMAT(/,17H INTERCEPT MATRIX)
      DO 9 I=1,M
      WRITE(2,105)(C(I,J),J=1,M)
    9 CONTINUE
      WRITE(2,107)
  107 FORMAT(/,20H STANDARD DEVIATIONS)
      DO 10 I=1,M
      WRITE(2,105)(S(I,J),J=1,M)
   10 CONTINUE
      RETURN
      END
```

```
      SUBROUTINE NORM(ATTEN,ANORM,TEMP,FREQ,A,DATA,TP,NO,M,M1,J)
      DIMENSION ATTEN(NO,M1),ANORM(NO,M1),TEMP(NO),FREQ(M1),
     1A(M1),TP(M1),DATA(NO,M)
      DO 2 I=1,NO
      ANORM(I,J)=(2.*ATTEN(I,J)*TEMP(I))/(FREQ(J)*A(J))
    2 CONTINUE
C*****TRANSFORM TO LN(XT) AND 1/T AND FILL DATA ARRAY
      DO 5 I=1,NO
      IF(ANORM(I,J).GT.1.E-6)GO TO 12
      DATA(I,J)=-100.
      GO TO 4
   12 CONTINUE
      IF(ANORM(I,J).LE.1.0)GO TO 6
      DATA(I,J)=0.0
      GO TO 4
    6 IF(TEMP(I).GE.TP(J)) GO TO 3
      DATA(I,J)=ALOG((1./ANORM(I,J))+SQRT((1./(ANORM(I,J)**2))-1.))
      GO TO 4
    3 DATA(I,J)=ALOG((1./ANORM(I,J))-SQRT((1./(ANORM(I,J)**2))-1.))
    4 CONTINUE
    5 CONTINUE
      RETURN
      END
```

APPENDIX 2
Proceedings of The Institute of Acoustics

Ultrasonic Attenuation in Doped Bismuth Germanium Oxide

P.K. Sandhu and M.J. Lea

Department of Physics, Bedford College, University of London

We have measured the ultrasonic attenuation in single crystals of bismuth germanium oxide, Bi_{12} Ge O_{20} (BGO) at frequencies ($\omega/2\pi$) from 10 to 190 MHz at temperatures (T) from 4.2 to 260K. We have studied both undoped crystals and crystals doped with Aℓ, Ga, Pb, Zn, Cr, P + Ga and Cr + Ga. The doped crystals were very kindly provided by Frau Dr. Grabmeier and R. Oberschmid of Siemens, München.

BGO is one of a group of isomorphous crystals whose formula is approximately Bi_{12} MO_{20} where M represents a metal (usually, but not necessarily, quadrivalent). These are cubic crystals, space group I23, and have interesting piezoelectric, photoconductive and optical properties which have found applications in surface acoustic wave and electro-optic devices.

Some of our measurements in undoped BGO are shown in Figures 1 and 2 and confirm previous results by Rehwald and his co-workers[1,2]. The most striking feature is a very strong attenuation peak at low temperatures only for those modes which involve the elastic constant C_{44} such as the transverse modes, T(100,001) and T_1(110,001) but not for the longitudinal mode L(100,100). This attenuation peak is typical of an anelastic relaxation due to point defects[3] with the attenuation (α) given by

$$\alpha = \frac{A}{T} \frac{\omega^2\tau}{(1 + \omega^2\tau^2)} \qquad (1)$$

where A is a constant proportional to the defect concentration and the relaxation strength. τ is a relaxation time which is well described by the Arrhenius relation

$$\tau(T) = \tau_\infty \exp(\theta/T) \qquad (2)$$

where $k_B\theta$ is an activation energy and the attempt frequency, $1/\tau_\infty$, is of the order of that for a lattice optical phonon. Our data has been fitted to equation (1), as shown in Figure 2, for the T_1(100,001) mode, to obtain values of A, θ and $1/\tau_\infty$.

The magnitude of this attenuation peak in BGO is strongly affected by the presence of dopants, as shown in Figure 3. Doping with the Group II element Zn (dopant fraction per formula unit $\leq$0.009[4] reduced the peak to 0.77 of its undoped value while doping with Aℓ(0.033), Ga (0.004) and Pb (~0.5) removed the attenuation peak completely. However, doping with Cr (0.009) increased the attenuation by a factor of 2.3. The crystals with two dopants, Ga (0.006) + Cr (5×10^{-5}), P (0.029) + Ga (0.004), also showed no large attenuation peak although some very small relaxation peaks may be discernible in the data. These measurements complement the work by Rehwald et al[2] on crystals of the isomorphous crystal, bismuth silicon oxide (BSO), doped with Group III elements. They found that Ga (0.002) and B (0.003) reduced the corresponding peak in BSO while Aℓ (0.008) removed it completely.

We have also investigated the effects of annealing on the ultrasonic attenuation by measuring the low temperature relaxation peak before and after

annealing at 425°C either in a vacuum or in a pure O_2 atmosphere. For an undoped crystal no change in the attenuation peak was found. However, for the Cr doped sample the attenuation was reduced by vacuum annealing to 0.57 of its original value and was restored by oxygen annealing as shown in Figure 4.

There seems to be a strong correlation between the ultrasonic attenuation, α, and the optical absorption, σ, in these crystals. BGO is an insulator with a direct band gap of 3.25 eV but the undoped crystals are a pale yellow colour and have considerable optical absorption in the visible region below the band edge. This absorption is not present [4] in those doped crystals which show no ultrasonic attenuation peak and these crystals are nearly transparent. Similar results in BSO were found by Rehwald et al [2]. Hence it seems probable that the same defect centre may be responsible for both the optical absorption and the ultrasonic attenuation in these crystals. Tanguay [5] found that the optical absorption in undoped BSO was unaffected by vacuum or O_2 annealing and, by inference, this correlates with our results on the annealing of undoped BGO crystals. However, for Cr doped BSO Tanguay found strong photochromic behaviour with very strong optical absorption bands which could be bleached by oxygen annealing and restored by vacuum annealing. This is exactly the opposite to the behaviour of the ultrasonic attenuation in our Cr doped BGO crystal (which is almost black).

The defects responsible for these effects are not yet known. If we assume a point defect is responsible for the ultrasonic attenuation then we can obtain its symmetry from selection rules [3]. Since the relaxation affects C_{44} but not $(C_{11}-C_{12})$ then the defect must have trigonal symmetry. It must therefore be associated with the oxygen atoms in the GeO_4 tetrahedra which lie at the cubic (23) sites in the crystal. Several possible defects have been suggested for the optical absorption, a recent proposal [4] being a Bi^{3+} ion on a Ge site with a hole on one of the surrounding O^{2-} sites. Such a defect would have the correct symmetry to produce the ultrasonic attenuation observed. Several mechanisms for the dopant-bleaching of the optical and ultrasonic absorptions can be envisaged but more work is needed to elucidate the exact mechanism.

For the photochromic effects Tanguay [5] has suggested that a charge transfer mechanism between neighbouring substitutional Cr and Bi ions on tetrahedral sites could produce two metastable states (absorbing and non-absorbing). Our data on Cr doped BGO suggests that one of these states may be the centre responsible for the ultrasonic attenuation.

We would like to thank Frau Dr. Grabmeier and R. Oberschmid for supplying the doped crystals and for details of their extensive electrical and optical measurements on these crystals. We are grateful for the assistance of S. Sen, A.K. Betts and other members of the Physics Department.

References

1. Rehwald, W., J.Appl.Phys. 44, 3017 (1973)
2. Rehwald, W., Frick, K., Lang, G.K. and Meier, E., J.Appl.Phys. 47 1292 (1976)
3. Nowick, A.S. and Berry, B.S., 'Anelastic relaxation in crystalline solids', AP (1972).
4. Oberschmid, R. and Grabmeier, B.C., private communication and German Physical Society, Freudenstadt, 1978.
5. Tanguay, A., Ph.D. thesis, Yale University (1977).

Proceedings of The Institute of Acoustics

Ultrasonic Attenuation in Doped Bismuth Germanium Oxide

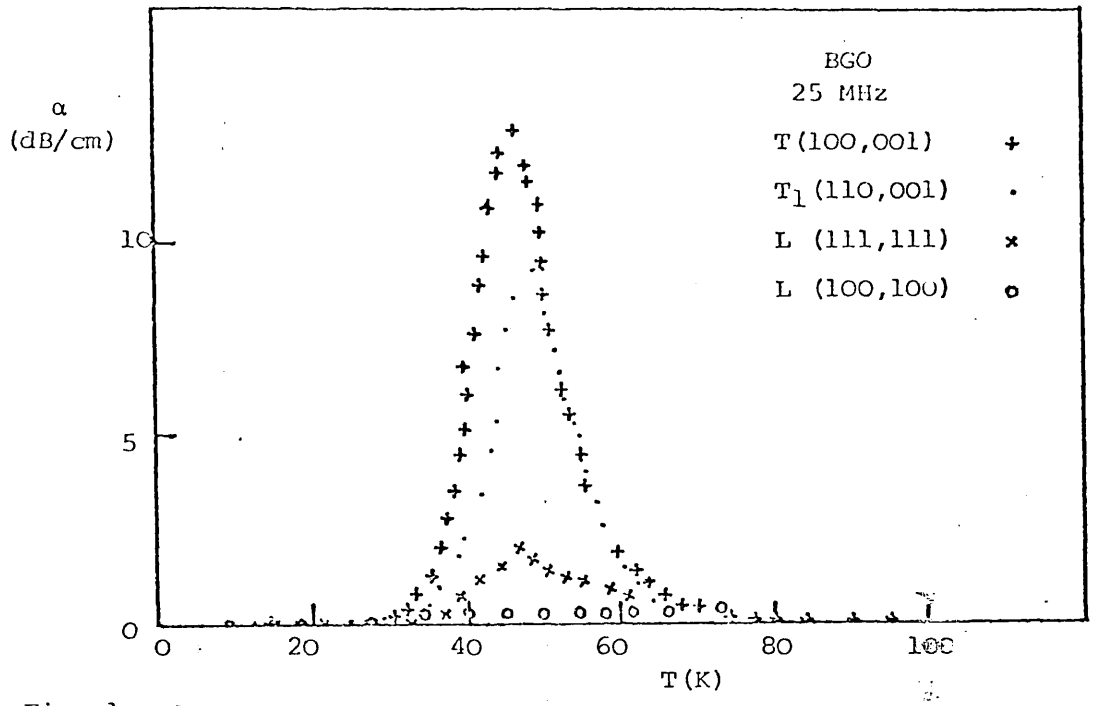

Fig. 1 Ultrasonic attenuation in undoped BGO for several acoustic modes

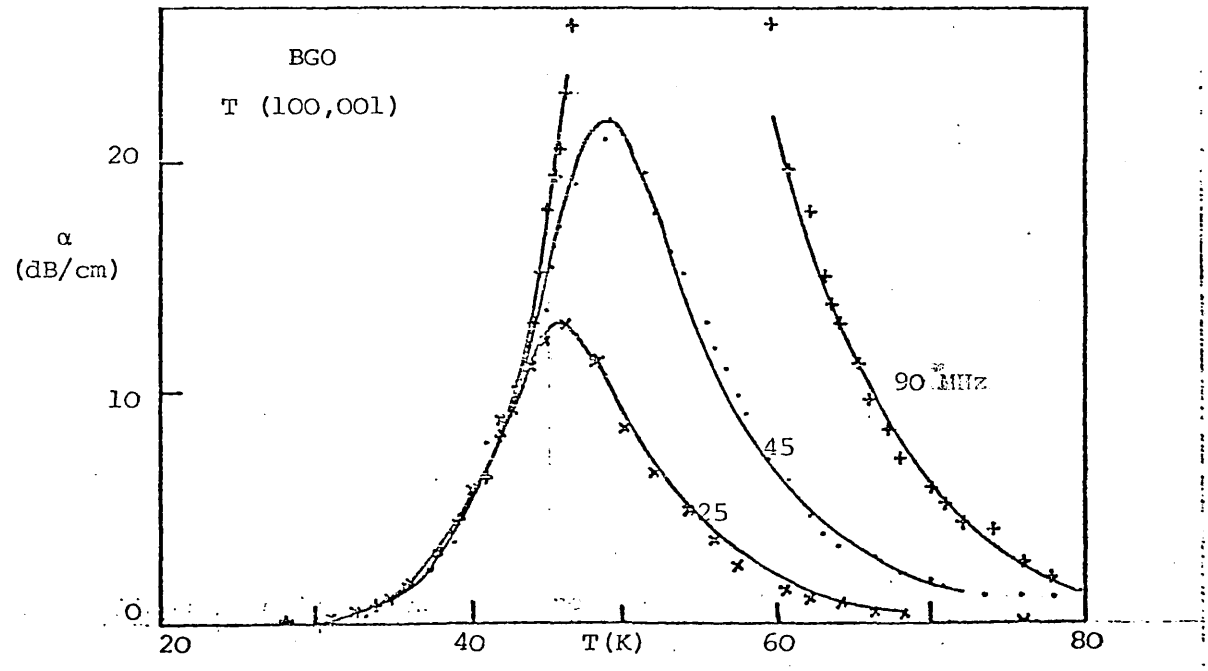

Fig.2 Attenuation of T (100,001) mode in undoped BGO fitted to eq. (1) with A = 34.8 dBK/cm MHz, θ = 460K, $1/\tau_\infty = 4.6 \times 10^{12}$ Hz

Proceedings of The Institute of Acoustics

Ultrasonic Attenuation in Doped Bismuth Germanium Oxide

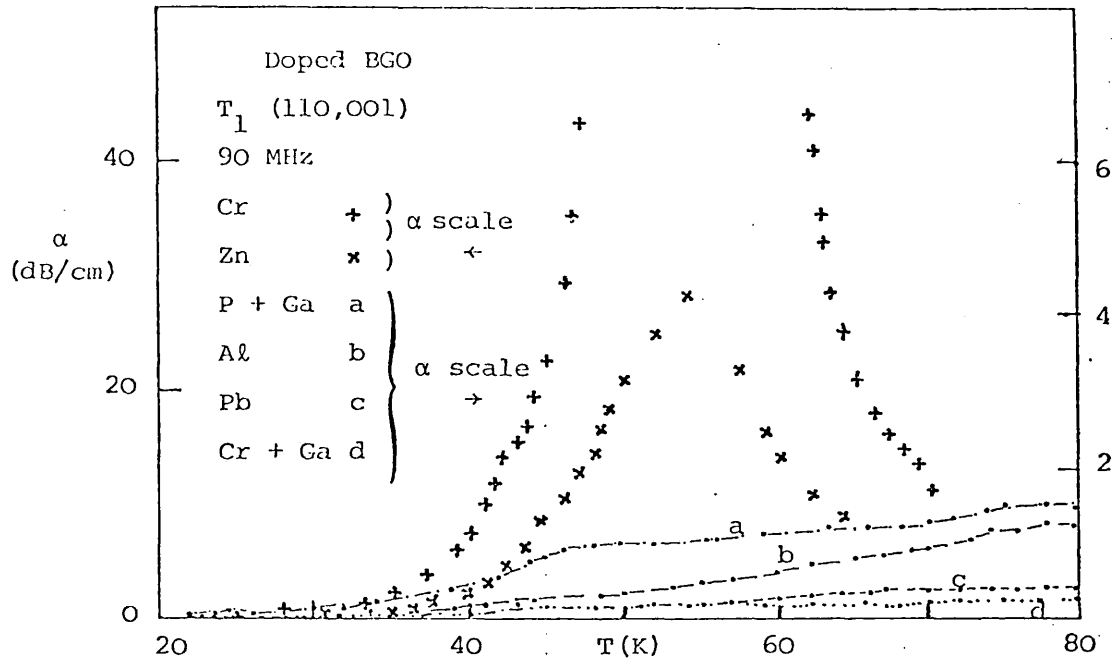

Fig. 3 Attenuation of T_1 (110,001) mode in doped BGO

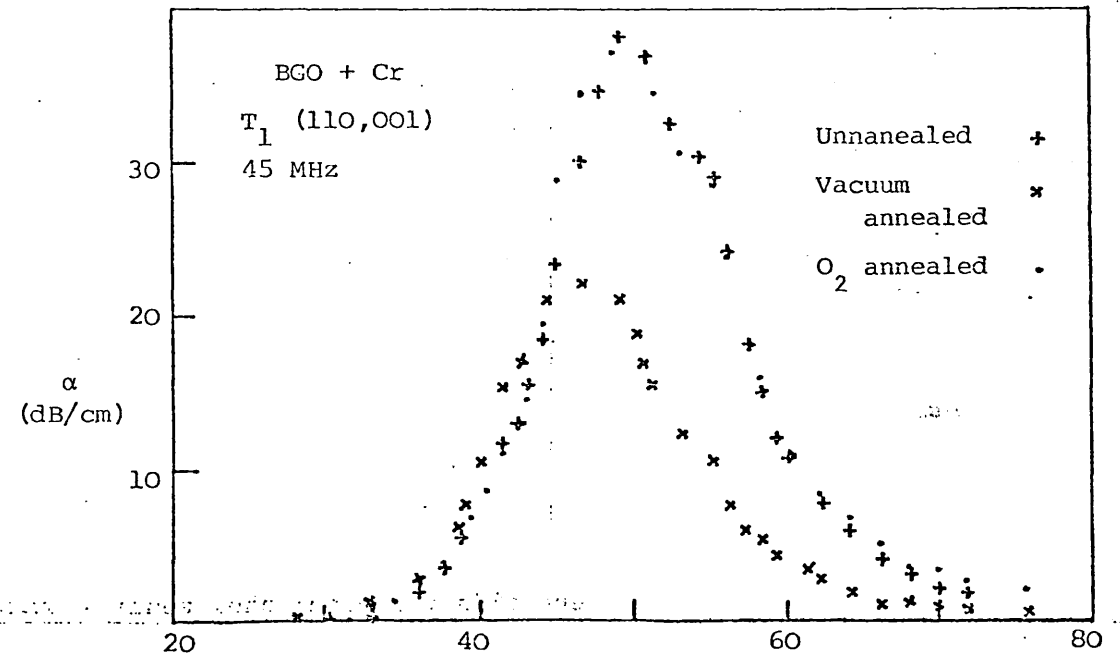

Fig. 4 Attenuation of T_1 (110,001) mode in Cr coped BGO, after annealing in vacuum and in oxygen